This electronic thesis or dissertation has been downloaded from Explore Bristol Research, http://research-information.bristol.ac.uk

Author:
Torre, Cyril C

Title:
Microscopy with Quantum States of Light

General rights
Access to the thesis is subject to the Creative Commons Attribution - NonCommercial-No Derivatives 4.0 International Public License. A copy of this may be found at https://creativecommons.org/licenses/by-nc-nd/4.0/legalcode This license sets out your rights and the restrictions that apply to your access to the thesis so it is important you read this before proceeding.

Take down policy
Some pages of this thesis may have been removed for copyright restrictions prior to having it been deposited in Explore Bristol Research. However, if you have discovered material within the thesis that you consider to be unlawful e.g. breaches of copyright (either yours or that of a third party) or any other law, including but not limited to those relating to patent, trademark, confidentiality, data protection, obscenity, defamation, libel, then please contact collections-metadata@bristol.ac.uk and include the following information in your message:

•Your contact details
•Bibliographic details for the item, including a URL
•An outline nature of the complaint

Your claim will be investigated and, where appropriate, the item in question will be removed from public view as soon as possible.

Microscopy with Quantum States of Light

By

Cyril Torre

Department of Physics
University of Bristol

A dissertation submitted to the University of Bristol in accordance with the requirements of the degree of Doctor of Philosophy in the Faculty of Science.

June 2023

Word count: ~ 36000

ABSTRACT

Microscopy is a technique to image samples, such as biological cells that cannot be seen unaided by the eye. Signal-to-noise ratio (SNR) and precision are important aspects for such imaging technique. The current methods for microscopy imaging rely on high intensity light that may degrade irreversibly the sample through photo-damage and photo-bleaching. In addition, the laws of quantum mechanics limit the performances of these imaging techniques due to the inherent noise of the electromagnetic field in the quadrature space.

In this thesis, I introduce two novel imaging techniques with quantum states of light acting as probes. First, I report the implementation of super-resolution microscopy with a two-photon interference: the Hong-Ou-Mandel effect. By measuring the time delay between a reference photon and a probe photon transmitting through the sample, the variation in thickness of a semi-transparent sample is evaluated in combination with two-dimensional raster scanning. The wavelength separation between the signal and the idler of a two-colour entangled state controls the sensitivity of the microscope where sub-μm axial precision is reported using up to 12.3 nm of detuning and $\sim 10^4$ detected photons pairs. Within the loss of the experimental setup, this corresponds to a sample illumination of fW level, corresponding from 8 to 12 order of magnitude below classical microscopes achieving similar performances. Consequently, the HOM microscope, reach higher Fisher information per photon, which can be an important consideration for photo-sensitive samples and can otherwise be a limiting factor for measurement precision.

In the second part, noise reduction within a coherent state due to Kerr squeezing with a photonic crystal fibre is used to enhance the precision for absorption microscopy. The classical noise is reduced by taking fast measurements and modulating the probe in time to be in a shot-noise limited bandwidth of the detector and the laser. Then, with the noise reduction of the amplitude squeezed light and despite the inherent noise of the laser, I report shot-noise precision on single-pixel measurements with squeezing of $\Phi_{log} = -0.88\ dB$ for $\sim 200\ \mu W$ of light detected. Furthermore, a quantum advantage of 1.13 ± 0.1 with $\Phi_{log} = -0.62\ dB$ is demonstrated for confocal microscopy imaging, where I show that sub-shot noise precision can be possible with a higher squeezing value above $\Phi_{log} \leq -1.6\ dB$.

Applications for bio-imaging can be found for these two microscopes, where high sensitivity or enhancement in the precision can be done without photo-damaging or photo-bleaching the sample either by having a probe at the photon level or by taking fast measurements and limiting the sample illumination.

ACKNOWLEDGEMENTS

First, I would like to thanks the Engineering and Physical Sciences Research Council (EPSRC) and the Centre for doctoral training in quantum engineering (QE-CDT) of the University of Bristol to help me financially to conduct my PhD projects. I want to thanks the imaging hub QUANTIC for helping me to reach out scientists across the UK working in my field of research.

On a second hand, I would like to thanks my supervisors, Jonathan Matthews and Alex McMillan. I got the support I needed to go through my experiments/projects, either in the good time and in the bad time, and I appreciated it a lot. Experimental work is never working as it should, but in a peculiar way, we managed to conduct the experiments and made them work. This success is not solely attributable to my efforts but also to the support you both provided. Alex, I apologise for any headaches my (fantastic?) English may have caused you. Thanks to John Rarity for the scientific discussions! I would like to thanks my mentor Javier who was a river to me. Thanks to Jason, for the good advises in the lab, mon ami (et mon khoya). Thanks to Sabine who advised me to apply to the CDT, I think I would have not applied for a PhD in Bristol without her support. Thanks to gymbro Andriy, Ben, Dave the petit pois and Elliot for supporting me within the cohort 5, you might hate (or love?) french people now, and I am glad that it is because of me. Some of you have already submitted, some of you are already doctor and hopefully everybody else will follow. Good luck to Alex Q., Cécile and Reece too! It was a lot of fun to do a PhD in the same time, kinda motivated me to see that a PhD can be depressing, but you are not alone. Thanks the people who gave a bit of their time to correct my English such as Alex B., Oli and Beth. Thanks again to Alex B. for the gym session, the scientific-chess-food discussions, and also to made me discover The Keg steakhouse! Thanks to George for your own time that you gave me to help me on my last project. Thanks to the metrology crew such as Giacomo, Giulia R., Frazer, Joel and David who spent some of his PhD time to do a voltage amplifier that I never used (sorry). Thanks to Dan, Molly and Ed for the conversations over lunchtime. You can always trust someone who value their own lunch! Thanks to the admin team, Emma, Sorrel, Lin, Holly, Belinda and Sam. Thanks to the QETLabs people who had to listen to me (I think) while I was complaining about UK, I did enjoy a lot. A wise man once told me "You never finish a thesis, you abandon it". He's right! Thanks Jorge B. for these wise words!

Merci aux potos français de Bristol: Chris, Elodie, James, Louise (même si te souviendras pas de moi), Lise, Ninon (same than Louise hein), Charles, Elliot, Elvine: beaucoup de raclettes, beaucoup de fromages, et du bon vins (merci mon dieu). Merci aux potos de la fac, Paul aka Vlospa, Pavel (bientôt la fin aussi). Merci à la famille, au fréro Cédric, qui fait beaucoup trop de vélo. Merci à sa compagne Julie aussi! Merci à maman et papa à qui j'ai parfois oublié les anniv' et les appels du weekend, j'avais une excuse maintenant va falloir faire attention. Pareil pour pépé et mémé, oui la bouffe en angleterre est pas ouf, mais en vrai ça va et je ne dépéris pas.

Finally, I would like to thanks amore mio, recently PhD in marine biology: Giulia (my Giulia). Auguri, e sono molto contento per te. Sono impaziente di vivere la mia vità con te. Molto di formaggi, pasta, pizze et tutti quanti. Grazie a la tua famiglia, MR Titi, MME Titi, Marcantoine il principe di Poggio Mirteto e grigettinno. Ti amo fino al $GN - z11$ e ritorno.

Je pourrai écrire beaucoup plus pour ces remerciements, mais même si je suis le premier auteur de cette thèse, cela ne veut pas dire que j'étais seul, et bien au contraire, c'est grâce aux supports et à plein de gens (stp papa pas de blague là dessus) que j'ai pu finalement finir cette thèse, du coup: MERCI!

AUTHOR'S DECLARATION

I declare that the work in this dissertation was carried out in accordance with the requirements of the University's Regulations and Code of Practice for Research Degree Programmes and that it has not been submitted for any other academic award. Except where indicated by specific reference in the text, the work is the candidate's own work. Work done in collaboration with, or with the assistance of, others, is indicated as such. Any views expressed in the dissertation are those of the author.

SIGNED: CYRIL CHRISTOPHE TORRE DATE: 30/06/2023

ROI ARTHUR : Bon ok, on va demander un interprète..

ROI BURGONDE : Aaaahhhh, Arthooouuurrr !!! Arthooouuurrr !!!

ROI ARTHUR : Et ben quoi ?

ROI BURGONDE : Cuillèèère !

ROI ARTHUR : Interprète !

ROI BURGONDE : Interprète !

ROI ARTHUR : Interprète !

ROI BURGONDE : Interprète ! Cuillèèère !

Saison 2, Episode 3, Kaamelott

MANUSCRIPTS AND PRESENTATIONS

The two-colour Hong-Ou-Mandel microscope, **Cyril Torre**, Alex McMillan & Jonathan C.F. Matthews.
Poster: BQIT, Bristol, UK, 26/04/2021.

Single-pixel imaging with heralded single photons, Steven Johnson, Alex McMillan, **Cyril Torre**, Stefan Frick, John Rarity & Miles Padgett
Doi: 10.1364/OPTCON.458248 (2022).

High resolution Hong-Ou-Mandel microscope for depth imaging, **Cyril Torre**, Alex McMillan & Jonathan C.F. Matthews.
Talk: Imaging and Applied Optics Congress 2022 (3D, AOA, COSI, ISA, pcAOP), Vancouver, Canada, 11/07/2022.
Doi: 10.1364/OPTCON.458248

Precision enhancement in microscopy imaging using a bright Kerr-squeezed state, **Cyril Torre**, George S. Atkinson, John Rarity, Jonathan C.F. Matthews & Alex McMillan.
Poster: BQIT, Bristol, UK, 24/04/2023.

Sub-μm axial precision depth imaging with entangled two-colour Hong-Ou-Mandel microscopy, **Cyril Torre**, Alex McMillan, Jorge Monroy-Ruz & Jonathan C.F. Matthews.
Doi: 10.1103/PhysRevA.108.023726 (2023).

Sub-μm axial precision depth imaging with entangled two-colour Hong-Ou-Mandel microscopy, **Cyril Torre**, Alex McMillan, Jorge Monroy-Ruz & Jonathan C.F. Matthews.
Talk: CLEO Europe, Munich, Germany, 26/06/2023.

TABLE OF CONTENTS

LIST OF TABLES

TABLE **Page**

LIST OF FIGURES

FIGURE **Page**

CHAPTER 1

INTRODUCTION

Metrology is the study of measurements. The term derives from ancient Greek "metron" and "logos" which can be literally understood as "study of measurements". In optics, light is used to probe a sample to get information on a desired parameter such as absorption. Then, through measurements, desired parameters are estimated with a certain degree of accuracy and precision. Imperfections of the detectors or the source of the probe light and environmental fluctuations leading to background noise can degrade the performance of measurements. The noise can be decreased by approaching the shot-noise limit (SNL), also known as the quantum noise limit (QNL), which corresponds to the minimum of uncertainty achievable by a classical state and which derives from the laws of quantum mechanics [95].

To approach the QNL with a classical state, scientists have developed several techniques, such as heterodyne detection by comparing a local oscillator to a sample beam allowing removing of excess noise within measurement [3, 69], stabilisation of the laser source [90, 171], quantum technologies like single-photon detectors in a quasi-photon number resolving scheme (used in chapter 3 to resolve the number of photons) [60] or even machine learning to remove the noise through algorithms [88, 166]. Despite all these efforts, measurements using classical resources are limited by the QNL which defines a fundamental bound. The QNL scales as the inverse of $\sqrt{N}$, where N is the number of photons of the probe. The cause is the inherent noise within the probe beam following $\sqrt{N}$ for an average of N photons detected. It is driven by the generation of the light following a Poisson distribution and for which the standard deviation is $\sqrt{N}$ [147]. Subsequently, quantum metrology investigates the performance of measurements achievable from quantum probe state of light [63]. Quantum mechanics allow measurements with performance beyond the QNL, where the correlation within photons of a same quantum state can achieve precision or sensitivity that a classical state cannot physically achieve [15]. The precision of a measurement can be described as the standard deviation for N repeated measurements, whilst the sensitivity can be seen as the smallest signal that an apparatus can distinguish amongst the noise, corresponding to the signal-to-noise ratio (SNR) [83, 146].

Quantum metrology represents a promising tool where quantum states of light used as probes have shown quantum enhancement [41, 44, 103, 113]. As this thesis focuses on quantum probe states of light for microscopy imaging, only the progress of quantum imaging will be discussed. For instance, the $NOON$ state corresponds to the generation of an entangled state of a superposition of N photons between two different modes [75, 140]. This state can be known as the "all and nothing" state where it can be described by a superposition of N photons in one mode and nothing in the second mode [5]. For such a quantum state, a sensitivity factor scaling with N have been demonstrated for phase measurements. This quantum state has been used for demonstrating an improvement of 1.35 in the SNR for measurements with $N = 2$. This imaging technique has been used for microscopy depth imaging in the nanometre range with $\sim 10^3$ photons pairs detected [108]. Additionally, $NOON$ states have been used for polarisation microscopy showing phase super sensitivity with $N = 2$ and $N = 3$ for ~ 50 photons detected per measurements (corresponding to 25 pairs for $N = 2$ and 17 triplets for $N = 3$) [77]. However even if the scalability is promising, the generation of a $NOON$ state with a high number of photons remains difficult and experimentally challenging. Higher number of $NOON$ state have been achieved but not applied to imaging. The cause is mainly the low efficiency detection of $NOON$ state and the generation becomes harder when $N > 2$, where the rate of a coincidence detection events for $N = 5$ have been reported to $10^{-2}\ Hz$ [5]. The low detection rate will make the imaging slower and experimentally challenging to perform.

Another approach is to use the correlation from the photons of a same pairs (also known as twin beams or biphoton state) [26, 81]. This state can be generated from spontaneous down conversion (SPDC), a non linear process where one pump photon generates two correlated photons from a same pair. Because the two photons of the same pair are correlated in time, this has been used to improve the SNR in the presence of noise for spectroscopy [81], and later on the time correlation of such a quantum state has been employed for single-pixel measurements imaging [79]. My contribution to this work was the implementation of the photon pair source for single-pixel imaging. The source was generating through SPDC a broad spectrum of correlated photon pairs from 700 to 950 nm. The imaging was done through a technique known as single-pixel imaging. One photon of the pair was sent toward a digital micro-mirror device (DMD) to generate a spatial pattern of the light. A DMD is a device constituted of micro-mirrors where each of the mirrors can be individually controlled, either in the mode "on" to reflect the light, or in the mode "off" to do not reflect the light. Afterwards this photon was sent to illuminate the sample. The detection was done with single photon detectors and a time-tagging electronic device to monitor coincidence events between the photon transmitting through the sample and the other photon of the same pair send to another detector. Generating different patterns with the DMD corresponds to projecting the sample onto an imaging basis, called Hadamard basis [62].

Measurements were made for both positive and negative patterns, where the difference within the signal for both patterns were reconstituting the image. The quantum advantage of such an imaging technique was by demonstrating a robustness to background noise compared to a classical probe light. For each of the probe beams, either classical or quantum, background noise with a LED was added to the measurements. After processing each of the images, the room mean squared error (RMSE) was calculated. Because the two photons from a same pair are correlated in time and the background noise corresponds to adding uncorrelated photons to the signal, the quantum probe states of light have demonstrated a robustness to the noise compared to classical probes [79]. Furthermore, the correlation of such a quantum state has previously been used to demonstrate sub-shot noise microscopy for single-mode raster-scan imaging [124] and multi-mode wide field imaging [126]. One photon of the pair was used as a probe transmitting through the sample whilst the second photon of the same pair was sent toward another detector and used as a reference photon to monitor simultaneously the fluctuation in intensity. Because the intensity fluctuation between the two beams is correlated, one could subtract the noise monitored on the reference beam to the probe beam and achieve sub-shot noise microscopy imaging [124, 126]. However, this scheme suffers from loss and it requires high transmission and detection and so far has been demonstrated only for a probe beam with a brightness up to $\sim pW$ level.

Generation of photon pairs can be used to produce squeezed states of light. When the generation of photon pairs is co-linear and the signal and idler are not distinguishable, one can generate a squeezed state of light exhibiting photon number reduction in a single mode [97]. To enhance the brightness of such a quantum state, two techniques have shown their effectiveness. The generation of squeezed states is done through optical parametric oscillator (OPO) or optical parametric amplifier (OPA). Both techniques are similar but the OPA needs to be triggered by implementing a coherent seed to the scheme, whereas the OPO only require squeezed vacuum and usually exploit cavities [101]. Due to the high brightness of the probe beam, one can use it for Raman spectroscopy where the noise floor is lowered due to the noise reduction granted by the squeezed state, showing a quantum enhancement in the SNR [29]. Squeezed states from OPA have demonstrated precision and SNR enhancements above the QNL for biological application such as particle tracking [147]. Bright squeezed states can also be generated with Kerr squeezing, showing quantum enhancement in the precision [13].

Non linear interferometry has been used in quantum imaging and have been demonstrated other promising effects through non-linear interferences between the signal and the idler. For this imaging technique, the measurements are done on the photon that does not interact with the sample, whilst the other photon of the same pair interacts with the sample [93, 94]. The performance of such a technique has been investigated and sub-diffraction resolution could be possible [61, 127, 153]. This scheme is promising for gas sensing where the detection in the near infrared region is challenging for single photon detectors, or could be use for bio-imaging, for instance using terahertz wavelength to perform in-vivo imaging [165].

In this thesis, quantum probes states of light are investigated for strategies of measurements involving discrete and continuous variables for confocal microscopy. Chapter 2 constitutes the background chapter of the thesis. A brief description of discrete and continuous variables frameworks for quantum metrology is given. Then parameter estimation problem is described and the Fisher information $\mathscr{F}(t)$ is defined as a tool to characterise the performance of the imaging techniques. In particular, the standard deviation of the measurement achieved by an optimal estimator is theoretically given by the Cramér-Rao bound, corresponding to $1/\sqrt{N\mathscr{F}(t)}$ where N corresponds to the number of photons. For the discrete and continuous variables states used in this chapter, the generation and the detection of such quantum states is described. Furthermore, the Hong-Ou-Mandel interference experimentally demonstrated in the chapter 3, is described in a quantum formalism.

In chapter 3, Hong-Ou-Mandel interferometry is implemented with confocal microscopy to evaluate the variation in thickness on a semi-transparent sample. It had been originally proposed to measure subpicosecond time delay measurements between two photons of the same pair [72]. Here, the precision of the time delay measurement is enhanced with a wavelength-entangled photon pair source. The source is used to control the axial sensitivity where sub-μm axial precision is reported with 10^4 photon pairs detected and a wavelength separation of 12.3 nm between the signal and the idler. The wavelength-entangled photon pair source is a single nonlinear crystal where the photon pairs are generated through spontaneous parametric down conversion [40]. A dual Sagnac interferometer arrangement allows for the generation of the wavelength-entangled state which is actively phase-stable with a PID controller feedback loop. Then, a Fisher information analysis is used to characterise the performances of the microscope where sub-fs precision is reported and constitutes to an improvement of 3 orders of magnitude to the original HOM effect [72].

In chapter 4, I report the use of of bright amplitude squeezed light through the Kerr effect to enhance the precision of confocal microscopy for static loss measurements. The state is generated with a photonic crystal fibre (PCF) where a non-linear effect of the third order induces self-phase modulation on a coherent state and displaces it to generate a bright squeezed state in amplitude with an average power of $\sim 200\ \mu W$. The strategy of measurement relies on decreasing the classical noise by taking a measurement in a shot-noise limited bandwidth of the laser and detector by modulating the light in time [13]. An electro-optic modulator modulates the phase of the probe between horizontal and vertical polarisation mode. Afterwards, the probe beam is transmitted through a polarising beamsplitter (PBS), where the probe beam is now path-modulated. Due to the PBS, a π-shift occurs between the horizontal and vertical components. One of the polarisation modes interacts with the sample before being recombined with another PBS with the second optical mode. The π-shift from the PBS induces a total cancellation of the time-modulation from the probe beam in the absence of the sample. However, in the presence of the sample the amplitude of one of the modes decreases from absorption of the sample. Thus, the output signal exhibits a time-modulation where its amplitude is proportional to the loss induced by the sample. This strategy of measurement corresponds to encode static loss in a higher shot-noise limited frequency bandwidth, where only the amplitude at the sideband frequency is monitored. Then, due to the noise reduction granted by the squeezed state, an enhancement in the precision of the measurements is experimentally demonstrated where shot-noise limited measurements are reported on a single-pixel measurement despite the inherent noise within the laser probe. Then, absorption microscopy is performed with the squeezed source to enhance the precision in the imaging, showing a quantum advantage of 1.14 ± 0.1 between the unsqueezed and amplitude squeezed state.

These two probes for quantum microscopy exemplify the interest and potential around exploiting quantum effects for imaging. In the first case performance of super-resolution microscope is approached with a sample illumination 8 to 12 order of magnitude below microscopes using classical light as a probe [114, 128]. For the Kerr-squeezing microscope, the results show enhancement with bright squeezed light and I evidence the capacity for, and pathway to, yet further improvements in the experiment. We show such improvements could lead to absolute enhancement precision in estimation static loss absorption beyond the QNL, with bright optical probes.

Chapter 2

Background

This chapter reviews the concepts useful to understand the thesis. A brief overview of discrete and continuous variables and their uses in quantum optics is described in the section 2.2. Then, section 2.3 reviews the concept of measurements for metrology, how a parameter is estimated and how an estimator can be optimised and quantified. Due to the probabilistic nature of the measurements, two points of view are presented, the Bayesian and frequentist point of view. Section 2.4 reviews the generation and the detection of photons pair from chapter 3. The two-photon interference used to achieve sub-μm axial precision for depth microscopy is explained with a single-mode and multi-mode interpretation. Finally, section 2.5 describes the generation and the detection of bright Kerr-squeezed light, corresponding to the probe state used in chapter 4 to achieve enhancement precision for absorption microscopy.

2.1 Statement of the work

This chapter is a background chapter. There is no novel work presented in this chapter.

2.2 Discrete & continuous variables

In statistics, a variable can be either discrete (DV) or continuous (CV). DV can only be labelled by a list of integers, where $n_{DV} \in \mathbb{N}$, while CV can take the value of any real numbers $n_{CV} \in \mathbb{R}$. For instance, the number of inhabitants in Bristol is a DV, whilst the area of the city is a CV. In quantum optic experiments, when measurements are done on the single-photon level, we consider the variable to be discrete as the number of photons can be counted for example with avalanche photodiode detectors (APD). When the probe beam reaches higher level of brightness, the detection technique of photon counting experiment cannot be used and we consider the probe of light to be a CV that we can monitor with p-i-n (PIN) detectors. PIN detectors are less sensitive than APDs, but can perform measurements for brighter sources and with a faster output rate [84].

In quantum metrology, DV allows great performance for a low level of brightness (typically around pW). The shot-noise limit corresponds to the best performance on a measurement that a classical state can achieve and is typically given by $\sim \sqrt{N}$ when N corresponds to the number of photons [168]. DV in quantum metrology has demonstrated sub-shot noise performance [26, 80, 124, 125, 145]. The limitation of the scalability in the brightness of photon counting experiment is due to the technique of detection, often relying on coincidences counting. In the coincidence measurement, the correlation between two photons of a same pair can be used to achieve sub-shot noise measurements [80, 124, 140]. A coincidence event corresponds to monitoring the arrival time of $N \geq 2$ photons within the same coincidence window. Enhancement in the brightness of the probe beam will increase the rate of detected photons and will require: 1) single photon detectors with a higher level of saturation and 2) higher resolution for time tagging operation. The limitation in the brightness of the probe beam for photon counting experiment is typically $\sim 400\ MHz$ for single photon detectors [52] and time-tagging electronics [11], limiting photon counting experiments to $10^2\ pW$.

For the reasons listed above, CV are used in quantum metrology to achieve higher level of brightness with the detection in the continuous regime with PIN detectors [25]. Because the probe beam is brighter, the detector can work at room temperature where the dark current (or dark counts) corresponding to fake event due to the thermal vibration within the detector does not need to be reduced by cooling down the temperature of the detector [25]. CV can be used in measurements in regimes that photon counting experiments could not achieve due to the requirement on the brightness of the probe beam, such as Raman spectroscopy. In fact, bright squeezed-light has demonstrated quantum enhancement in the signal-to-noise ratio for Raman spectroscopy in the CV regime [29]. Furthermore, other quantum precision enhancement schemes has been demonstrated with such quantum states [13, 147]. These higher level of brightness can achieve better precision than photon counting experiment due to the higher number of photon detected, with noise reduction from the squeezed state demonstrating precision enhancement within the measurements compared to a classical state. However, as discussed previously the QNL scale with $\sqrt{N}$ while the number of photon within the signal scale with N when the power increases. It means that to maintain sub-QNL performance, only a smaller amount of noise can be tolerated from the apparatus, and more difficult it becomes to achieve sub-QNL measurements for quantum imaging.

Finally, it is important to say that quantum metrology can benefit from photon counting experiment such as the ones using NOON state and Hong-Ou-Mandel interferometry, corresponding to quantum effect occurring at the photon level [108, 140]. Such input states who requires single photons detectors and/or coincidence counting measurement scheme can lead to quantum enhancement or high resolution measurement with few thousand of photons [72, 99, 106, 120].

From the previous discussions, CV and DV propose different strategies of measurements where one can achieve high precision with few thousand of photons by the first whilst the second one can deal with higher level of brightness of the probe beam and where a quantum advantage has been demonstrated. This thesis proposes two strategies of measurements, where in chapter 3 a photon counting experiment based on a Hong-Ou-Mandel interferometry can achieve sub-μm axial precision for depth imaging with $\sim 10^4$ photon pairs detected per measurement whilst chapter 4 demonstrates precision enhancement for absorption imaging with a probe beam of $\sim 200\ \mu W$.

2.3 Theory of measurement

To gain access to knowledge about a parameter φ in physics, a state ρ interacts with the sample where the parameter is encoded. Then, $\hat{\rho}(\varphi)$ is measured and φ can be calculated from an estimator (Fig. 2.1). The measurements used to estimate the parameter are imperfect (noise, device precision, etc) and lead to a set of data $\mathbf{x} = \{x_1, x_2, ..., x_n\}$ following a probability distribution [17]. Therefore, we call $\widehat{\varphi}$ the estimation of the true value φ over a data set $\mathbf{x}$.

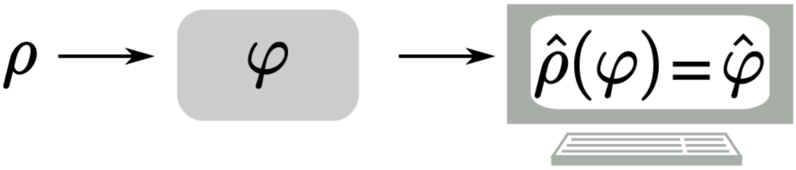

FIGURE 2.1. **Measurement scheme in metrology.** To extract the value of a parameter φ from a sample, a source ρ is used to interact with the sample. Then, the measurement is performed on the state $\hat{\rho}(\varphi)$. Finally, an estimation $\hat{\varphi}$ can be inferred from it.

In quantum optics, the probe can be discrete such as correlated photon pairs [124, 149], continuous such as squeezed state of light for gravitational wave detection [2, 31, 148] or even both [10]. A strategy of measurements is defined as having access to φ with the best accuracy and precision achievable (Fig. 2.2). In a mathematical formalism, the likelihood function $f(x|\varphi)$ defines the probability of observing the outcome x given the parameter φ. The bias can be calculated which computes the deviation between the estimated value $\widehat{\varphi}$ and the true value φ, where:

$$bias(\widehat{\varphi},\varphi) = \mathbb{E}(\widehat{\varphi}) - \varphi. \tag{2.1}$$

$\mathbb{E}(\widehat{\varphi})$ is the expected value of $\widehat{\varphi}$ given by:

$$\mathbb{E}(\widehat{\varphi}) = \sum \widehat{\varphi}(x) f(x|\varphi) \tag{2.2}$$

$$\mathbb{E}(\widehat{\varphi}) = \int \widehat{\varphi}(x) f(x|\varphi) dx, \tag{2.3}$$

respectively, for discrete and continuous variables. Then we can characterise the performance of a measurement from the standard deviation σ which can be calculated as:

$$\sigma(\widehat{\varphi}) = \sqrt{\mathbb{E}\left[\widehat{\varphi}^2\right] - \mathbb{E}\left[\widehat{\varphi}\right]^2}. \tag{2.4}$$

Eq. (2.1) quantifies the error between the true value and the estimated value and is known as the accuracy whilst Eq. (2.4) quantifies how the estimator deviates from the expected value, defining the precision. The diagram from Fig. 2.2 shows two data sets of measurements for which in (a) the measurements are accurate and (b) not accurate but more precise than (a). In metrology, the goal is to decrease the bias, ideally to 0 and to have the highest precision (*i.e.* the smallest variance) bounded by the laws of physics and statistics (Heisenberg uncertainty and Cramér-Rao bound [42, 116, 133] defined in section 2.3.2).

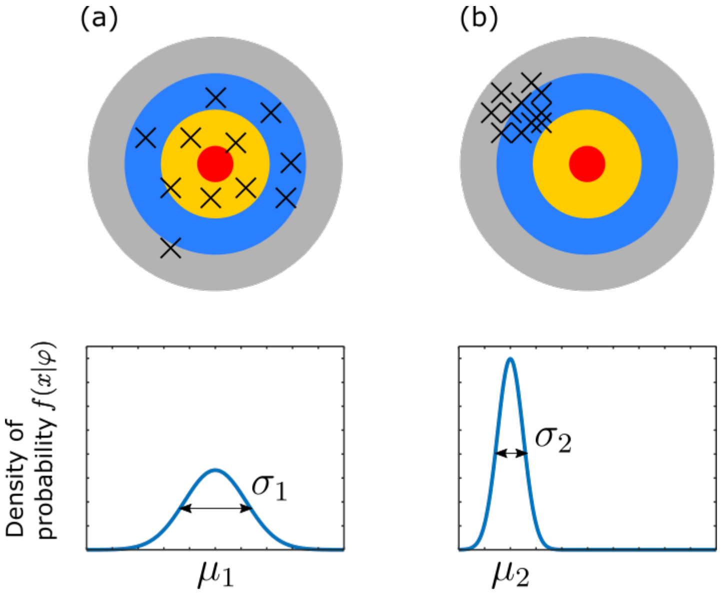

FIGURE 2.2. **Accuracy and precision.** Schematic of (a) accuracy and (b) precision. Two sets of measurements, in (a) accurate but not precise and in (b) not accurate but more precise than (a).

In practice, the central limit theorem is an important resource in statistics and especially for measurements. For a large data set $\mathbf{x}$ following a random distribution, the sampling distribution of the mean will always be normally distributed [27]. In this thesis the number of photons per measurements are from thousands up to a billion of photons and satisfy the condition of large data set. Hence, the density of probability $f(x|\varphi)$ follows the behaviour of a normal distribution with its mean $\mu_{\widehat{\varphi}}$ and standard deviation $\sigma_{\widehat{\varphi}}$. It makes the calculation of the precision quite easy, as the confidence level defines the probability to estimate $\widehat{\varphi}$ within an interval. For a normal distribution, the confidence level of 68% is defined by the interval $[\mu_{\widehat{\varphi}} - \sigma_{\widehat{\varphi}}; \mu_{\widehat{\varphi}} + \sigma_{\widehat{\varphi}}]$. Thus, in this thesis the precision is given by the standard deviation of the estimates.

Finally, to optimise the estimates $\widehat{\varphi}$, the mean squared error (MSE) defines the error due to the accuracy and precision and can be expressed as [156]:

$$MSE(\widehat{\varphi}) = (\sigma_{\widehat{\varphi}})^2 + bias(\widehat{\varphi}, \varphi)^2. \tag{2.5}$$

However because the true value of a parameter φ is unknown and is experimentally impossible to know, the bias cannot be calculated experimentally. Usually the bias is set to 0 and an estimator is found to minimise the standard deviation.

2.3.1 Bayesian & frequentist statistics

To estimate a parameter φ, two approaches in statistics are used, the Bayesian and frequentist point of view. Both of these techniques use the likelihood estimator. The likelihood estimator allows to estimate the parameter φ dependant of random observables x_i.

To estimate a parameter φ, two primary approaches in statistics are employed: the Bayesian and frequentist perspectives. Both methodologies utilise the likelihood estimator, a tool facilitating parameter estimation based on random observables x_i. Consider a set of random observables denoted as $\mathbf{x} = \{x_1, x_2, \ldots, x_n\}$, dependant on the parameter φ. The probability of observing the values x_i given the parameter φ is represented as $f(x|\varphi)$. For example, in chapter 3, the Hong-Ou-Mandel (HOM) interference is conceptualised as the probability $P_{11}(N_{11}|t)$, where P_{11} is the probability density of observing N_{11} anti-bunching events, contingent upon the time delay t between interfering photons. While the probability distribution $f(x|\varphi)$ is usually known and derived from the theory of the physical phenomenon (in chapter 3, denoted as P_{11} and given by Eq. (3.15)), the goal is to estimate the parameter φ based on measurements x_i. Similar to chapter 3, where anti-bunching events are measured to estimate the time delay t, we employ a likelihood estimator as a function to estimate φ from the measurements. The likelihood estimator can be seen as a probability density function to observe the measurement x_i given the parameter φ, expressed as:

$$L(\varphi|x) = f(x|\varphi). \tag{2.6}$$

Despite the equality from Eq. (2.6), $L(\varphi|x)$ and $f(x|\varphi)$ do not have the same interpretation. $f(x|\varphi)$ is the density of probability to observe a measurement x_i for different values of φ, while

$L(\varphi|x)$ corresponds to the likelihood of the parameter φ for certain values after observing the measurements x_i. In other words, to find the parameter φ, it is essential to take measurements. In an experiment, after measurements, we obtain experimental data in the form of $y = \{y_1, y_2, \dots, y_m\}$, resulting from m measurements made to estimate the parameter φ. The probability of obtaining these measurements given φ is described by:

$$L(\varphi|y) = \prod_i f(y_i|\varphi). \tag{2.7}$$

The Maximum Likelihood Estimator (MLE) is a function that maximises the likelihood estimator and is given by.

$$MLE(\varphi) = \text{argmax}_\varphi L(\varphi|x) \tag{2.8}$$

The MLE is asymptotically unbiased, and for a large number of measurements y_i, it converges toward the true value φ, saturating the Cramér-Rao bound [30, 91]. Therefore, to maximise the likelihood, we solve:

$$\frac{\partial L}{\partial \varphi} = 0. \tag{2.9}$$

However, because Eq. (2.7) is a product, Eq. (2.9) can be challenging to solve. Therefore, we often solve the same equation with the log-likelihood instead. The product becomes a sum, and the log-likelihood $l(\varphi|y)$ is given by:

$$l(\varphi|y) = \sum_i \log(f(y_i|\varphi)) \tag{2.10}$$

Eq. (2.9) becomes more manageable to solve when the log-likelihood $l(\varphi|y)$ is used. Finally, in physics, when the sample size m is large enough, we can use the central limit theorem, which specifies that for a normalised density of probability, the sampled probability distribution merges to a normal distribution $N(\mu,\sigma)$. After estimating the parameters μ and σ, we usually have $\hat{\varphi} = \mu$ and $\Delta\hat{\varphi} = \sigma$, where $\hat{\varphi}$ is the estimation of the parameter φ from the measurements y_i, and $\Delta\hat{\varphi} = \sigma$ represents the uncertainty on this estimation. The interval $[\mu - \sigma, \mu + \sigma]$ corresponds to a confidence interval of 67%, and intervals with 2σ or 3σ can be used to increase the confidence level[1].

In statistics, for a frequentist point of view, no hypothesis is made and the probability of estimating φ is calculated from the probability to observe or not the outcome x. It is easy to implement when a large data set is accessible in an experiment and it assumes that the parameter to be estimated is fixed. The inconvenience of such estimation is its dependence on the number of measurements. Because the number of measured outcomes x is not infinite, there is a discrepancy between the true value and estimated value φ. This can lead to a non-physical estimator for quantum tomography where the estimation of a quantum state can be found outside of the Bloch sphere [39, 143].

---

[1] In Bayes statistics, the credible interval can be used instead of the confidence interval.

For the Bayes point of view, statistics are inferred from the Bayes' theorem given by [155]:

$$P(\varphi|x) = \frac{P(\varphi)P(x|\varphi)}{P(x)}, \tag{2.11}$$

where $P(\varphi|x)$ is the posterior probability distribution, $P(\varphi)$ is the prior probability distribution corresponding to the probability assigned to φ before the experiment, $P(x|\varphi)$ is the likelihood function and $P(x)$ is the evidence from the probability of the data. It keeps updating the probability from a belief (which defines the prior, probability of distribution of the parameter φ over the observable x) whilst new data is taken. The advantage of this method is the fact that the probability is always updated with new data and the estimator can realistically fit the model where measurements errors are occurring within the data set [32]. However the prior is subjective or arbitrary and requires advanced statistics on the model [92].

2.3.2 Measurement optimisation: Fisher information & Cramér-Rao bound

The Fisher information $\mathscr{F}(\varphi)$ is a mathematical tool widely used in quantum metrology [13, 36, 96, 99]. For a likelihood function $f(x|\varphi)$, $\mathscr{F}(\varphi)$ quantifies the information gain from the measurements of x over φ [57, 98]. For discrete variables it is defined as:

$$\mathscr{F}(\varphi) = \sum \left(\frac{d}{d\varphi} log\left(f(x|\varphi)\right)\right)^2 f(x|\varphi) \tag{2.12}$$

whilst for continuous variables we write:

$$\mathscr{F}(\varphi) = \int \left(\frac{d}{d\varphi} log\left(f(x|\varphi)\right)\right)^2 f(x|\varphi)\, dx. \tag{2.13}$$

$\frac{d}{d\varphi} log[f(x|\varphi)]$ is known as the score function and corresponds to the sensitivity of the model to a small variation of the parameter at the different values of φ.

In experimental physics, $\mathscr{F}(\varphi)$ is particularly useful when it is combined with the Cramér-Rao bound (CRB). The CRB is the ultimate bound on the variance which can be achieved from a strategy of measurements [42, 116]. It gives a bound on the variance $\sigma^2_{\hat{\varphi}}$ for an estimator $\hat{\varphi}$ and can be written as:

$$\sigma^2_{\hat{\varphi}} \geq \frac{1}{N\mathscr{F}(\varphi)}, \tag{2.14}$$

where N relates to the number of trials the experimental strategy is repeated (*e.g.* the number of photons probing the sample). An optimal strategy of measurements saturates Eq. (2.14). Therefore, $\mathscr{F}(\varphi)$ is a great tool to reach the best precision $\sigma_{\hat{\varphi}}$ for an estimator by saturating the CRB. However, it does not take into account experimental imperfections such as drift within the measurements due to environmental perturbations and focus on one strategy of measurements only. However, it allows to know a theoretical bound on the precision of the strategy of measurement.

2.3.3 Quantum Fisher information

In quantum mechanics, when the source in a state ρ interacts with the sample to extract the parameter φ, the measurements are done via positive operator-valued measures (POVMs) described by a set of operators $\{\hat{E}_x\}$. $\{\hat{E}_x\}$ are non-negative Hermitian operators where $\int \hat{E}_x dx = \mathbb{1}$ and x corresponds to the observable outcomes from the POVM. Then, the probability to observe x dependant of the parameter φ is given by [22]:

$$f(x|\varphi) = Tr[\hat{E}_x \rho_\varphi]. \tag{2.15}$$

Here, ρ_φ is a density matrix containing the parameter to estimate φ encoded in the state $|\Psi(\varphi)\rangle$, (for a pure state) and in this case $\rho_\varphi = |\Psi(\varphi)\rangle\langle\Psi(\varphi)|$. Hence, a new quantity known as the quantum Fisher information (QFI) $\mathscr{F}_Q(\varphi)$ is defined as [19]:

$$\mathscr{F}_Q(\varphi) = Tr(\rho_\varphi \mathscr{L}_\varphi^2), \tag{2.16}$$

where $\mathscr{L}_\varphi$ is an hermitian operator called the symmetric logarithmic derivative and is implicitly defined by:

$$\frac{1}{2}(\mathscr{L}_\varphi \rho_\varphi + \rho_\varphi \mathscr{L}_\varphi) = \frac{\partial \rho_\varphi}{\partial \varphi} = -i[K_\varphi, \rho_\varphi]. \tag{2.17}$$

$\mathscr{L}_\varphi$ is related to K_φ, known as the Hermitian generator of displacement and is given by:

$$K_\varphi(t) = i\frac{\partial U_\varphi(t)}{\partial \varphi} U_\varphi^\dagger(t), \tag{2.18}$$

for $U_\varphi(t)$ the unitary operator describing the time evolution of the quantum state, dependant of the parameter φ. Then, for pure state only, the QFI can be reduced as [19, 53]:

$$\mathscr{F}_Q(\varphi) = 4(\Delta x_\varphi), \tag{2.19}$$

where Δx_φ is the uncertainty (or standard deviation) on the observable x. While the classical FI quantifies the information over an unique strategy of measurement, the QFI quantifies how well a parameter φ can be estimated based on the given quantum state by calculating the information gain over all possible POVMs. Therefore from the QFI we can deduce an ultimate bound, called the quantum Cramér-Rao bound (QCRB) given by [23, 24]:

$$\sigma_{\hat{\varphi}}^2 \geq \frac{1}{N\mathscr{F}(\varphi)} \geq \frac{1}{N\mathscr{F}_Q(\varphi)}. \tag{2.20}$$

It works for some specific classes of state and non-unitary processes [46, 49, 102] but for mixed state this is not trivial and sometimes $\mathscr{F}_Q(\varphi)$ cannot be calculated. Finally, it is important to note that despite the fact that $\mathscr{F}_Q(\varphi)$ quantifies the information over all POVMs, this does not give any information about what these measurements are.

2.4 Quantum optical theory for discrete variable states

This section covers the theory behind the generations of photon pairs source via spontaneous parametric down conversion (SPDC), the interference of a two-photon state used to describe the Hong-Ou-Mandel microscope in chapter 3 and the detection of the photons with avalanche photodiode detectors and time-tagging electronic.

2.4.1 State generation: the spontaneous parametric down conversion

Spontaneous parametric down conversion (SPDC) is widely used in quantum optics to generate photon pairs in quantum metrology [99, 103], quantum communication [64, 144] and quantum computation [16, 170]. It is a second order non-linear response of a medium to an electromagnetic (EM) field. It occurs for non-centrosymmetric crystals, meaning that the medium does not display inversion symmetry[2] [21]. When the medium interacts with an EM field, the dipole moment per unit volume (also called polarisation **P**) of the material can be written as:

$$\mathbf{P} = \varepsilon_0 \chi \mathbf{E}. \tag{2.21}$$

E is the electric field from an optical source, ε_0 is the permittivity of the vacuum and χ is the electric susceptibility defined as:

$$\chi = \sum_{i=1}^{n} \chi^{(i)} E^{i-1}. \tag{2.22}$$

Hence, by combining Eq. (2.21) and (2.22), **P** can be written as a sum of power series of **E** as:

$$\mathbf{P} = \varepsilon_0 \left(\chi^{(1)}\mathbf{E} + \chi^{(2)}\mathbf{E}\mathbf{E} + \chi^{(3)}\mathbf{E}\mathbf{E}\mathbf{E} + ... \right). \tag{2.23}$$

$\chi^{(1)}$ is the linear response of the medium, where the real part $\Re[\chi^{(1)}]$ is known to be the refractive index of the medium dependant of the EM's optical frequency and the imaginary part $\Im[\chi^{(1)}]$ is the absorption profile of the medium. $\chi^{(2)}$ and $\chi^{(3)}$ are the non-linear susceptibilities of the medium of the second and third order and contribute to the non-linear response of the medium. SPDC is a non-linear process of order 2 triggered by a laser propagating within a non-linear crystal. In chapter 3, the pump laser is a continuous laser and is not bright enough to trigger the higher non linear effects such as such $\chi^{(3)}$ (see section 3.5).

Fig. 2.3 shows a diagram of the SPDC process. A pump photon oscillating at a angular frequency ω_p propagates in a non-linear crystal (*e.g.* potassium titanyl phosphate, KTP) along a direction given by its momentum $\overrightarrow{k_p}$. Due to the non-linear interaction with the crystal, it generates two correlated photons commonly called signal (s) and idler (i) oscillating at angular frequencies ω_s and ω_i with their respective direction of propagation $\overrightarrow{k_s}$ and $\overrightarrow{k_i}$. Hence, the

---

[2] For centrosymmetric medium such as silicon fibre used in chapter 4, $\chi^{(2)} = 0$ and even-number non-linear interactions cannot occur.

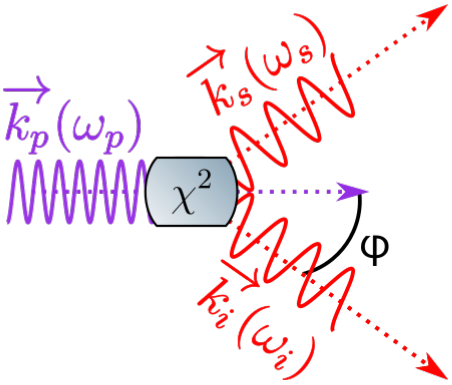

FIGURE 2.3. **Spontaneous parametric down-conversion diagram.** Pump photon with an angular frequency ω_p generates two daughter photons (s for signal and i for idler) via spontaneous parametric down conversion (χ^2), where the conservation of energy and momentum are fulfilled. One pump photon gives two correlated photons. Note that this non-linear effect is spontaneous and therefore has a very low efficiency, where most of the pump photons are transmitted through the medium.

conservation of energy and momentum can be written as follows:

$$\omega_p = \omega_i + \omega_s \tag{2.24}$$

$$\vec{k}_p = \vec{k}_i + \vec{k}_s. \tag{2.25}$$

Where $|\vec{k}| = \frac{\omega n(\omega)}{c}$, $n(\omega)$ the refractive index dependant on ω and c the speed of the light, and where Eq. (2.25) corresponds to a perfect phase-matching. However because $n(\omega_p) \neq n(\omega_s) + n(\omega_i)$, perfect phase-matching along the crystal is not possible for SPDC due to the wavelength difference between the downconverted photons and the pump photon. Hence in Eq. (2.25), we can consider the quantity Δk corresponding to the phase mismatch between the pump and the downconverted photons, with Δk defined by:

$$\Delta k = k_p - k_i - k_s - \frac{2\pi}{\Lambda} \approx 0. \tag{2.26}$$

Where k_p, k_i and k_s are respectively the wavenumbers of the pump, idler and signal photons, and where Λ corresponds to the period of the polling done on the crystal to correct the phase mismatching.

In a quantum mechanical formalism of this phenomenon, we can describe the generation of the downconverted photons by the following two-photon state $|\Psi\rangle$ [71, 110, 123]:

$$|\Psi\rangle = |0_s, 0_i\rangle + \xi \int d\omega_s d\omega_i \alpha_p(\omega_s + \omega_i) h(\omega_s, \omega_i) \hat{a}_s^\dagger(\omega_s) \hat{a}_i^\dagger(\omega_i)|0\rangle \tag{2.27}$$

with ξ characterising the nonlinear interaction strength, $\alpha_p(\omega_s + \omega_i)$ the spectral amplitude of the pump field centred at the frequency ω_p fulfilling Eq. (2.24) and $\hat{a}_s^\dagger(\omega_s)$ and $\hat{a}_i^\dagger(\omega_i)$ are the creation operators for the signal and the idler photons with $\hat{a}_s^\dagger(\omega_s)\hat{a}_s^\dagger(\omega_s)|0\rangle = |\omega_s, \omega_i\rangle$. $h(\omega_s, \omega_i)$ is the consequence of the phase mismatch and is defined by:

$$h(\omega_s,\omega_i) = h(L\Delta k) = e^{-i\frac{L\Delta k}{2}} sinc\left(\frac{L\Delta k}{2}\right), \tag{2.28}$$

where L corresponds to the length of the crystal and Δk is defined by Eq. (2.26). The phase mismatch induces an oscillation in the light generated through the SPDC process whilst the pump laser propagates within the crystal (see Fig. 2.4, black curve). To generate downconverted photons through the crystal, quasi phase matching (QPM) is done on the crystal by using periodic poling [3],[4]. This technique partially corrects the phase mismatch and avoids the generated light to oscillate around 0. In Eq. (2.26), QPM is done by adding the correction factor $2\pi/\Lambda$ to the phase mismatch Δk.

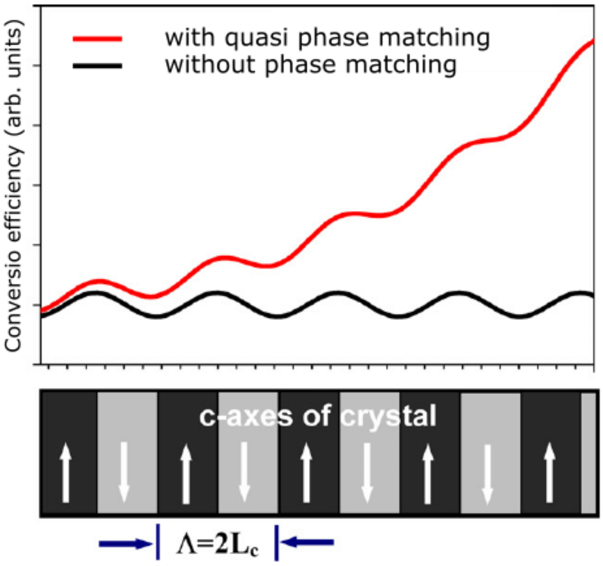

FIGURE 2.4. **Quasi phase-matching scheme.** Conversion intensity (arb. units) of the non-linear process versus the length of the crystal with no phase matching (black trace) and quasi phase matching using periodically poling (red trace). Figure from [34].

The most common technique is known as ferroelectric domain engineering and consists of periodically varying the sign of the nonlinear susceptibility by applying a strong electric field to a ferroelectric crystal such as potassium titanyl phosphate (KTP) or lithium niobate (LN) crystals [1, 74, 163]. For non ferroelectric crystal such as barium titanate (BTO), the phase-matching is done whilst the crystal is grown in laboratory [20, 37]. Semi-conductors can also

---

[3] QPM is used for other non linear process such as second harmonic generation (SHG) for the generation of bright pulses. The pulse is stretched, amplified and then recompressed. Therefore the period of the polling is nonuniform and is called chirped QPM [59]. Note that this technique of high-intensity ultrashort optical pulses led to a Nobel prize in 2018 to Gerard Mourou and Donna Strickland [104, 142].

[4] For non-collinear such as barium borate crystal, exact phase-matching is possible without QPM [110].

be used where the QPM is engineered by micro-structuring it with a method called orientation-patterned growth [74]. Because the QPM is dependant on the refractive index, the temperature of the crystal and the incident angle of the pump need to be controlled. Fig. 2.4 shows the conversion efficiency without QPM (black) where an oscillation with a period of $\Lambda = 2L_c = 2\pi/\Delta k$ is apparent. $L_c = \pi/\Delta k$ is known as the coherence length and it corresponds to the distance for which the pump and downconverted waves accumulate a phase difference of π [74]. The red trace corresponds to QPM with periodically poling in the crystal inducing a variation in the sign of the non linear susceptibility with a period of $\Lambda = 2L_c$. The period of the polling Λ is chosen to fulfil [56]:

Thus, the period of the poling needs to be wisely chosen to generate downconverted photons with the desired wavelength for the right laser pump. Usually, the crystal is in an oven where its temperature can be controlled with a PID temperature controller. In chapter 3, the wavelength separation of the downconverted photons for the two-colour entangled state is done by changing the temperature of the crystal with an oven. Λ and λ_p are fixed, whilst n_p, n_i and n_s are temperature dependant. These changes in the refractive index modify the length of the wave vectors $|\overrightarrow{k}|$, causing a change in the wavelength of the downconverted photons [35].

Finally, the temporal shape of the photons can be inferred from the type of the crystal. For a type-II crystal (used in chapter 3) the signal has the same polarisation as the pump but the idler's polarisation is orthogonal to them inducing $n(\omega_i) \neq n(\omega_s)$. With the absence of narrowband spectral filtering, the downconverted photons ideally match the temporal shape of a top-hat function [123, 134] with $\tau = DL$, where D is the difference between the inverse group velocities of the two downconverted photons. The bandwidth of a downconverted photon at the wavelength λ from a type-II SPDC is given by [55, 123]:

$$\Delta\lambda = \frac{\lambda^2}{\Delta n L}, \tag{2.29}$$

where Δn is the refractive index difference seen by the signal and the idler and L the length of the crystal.

2.4.2 Two-photon interference: Hong-Ou-Mandel effect

Originally discovered in 1987 to measure subpicosecond time delay between two photons, Hong-Ou-Mandel (HOM) interference is a two-photon interference observed when two photons in separate temporal modes, but otherwise indistinguishable, are made to overlap at a beamsplitter (BS) [72]. As the relative arrival time t shown in Fig. 2.5 between the two photons is reduced to zero ($a \to c$), the detection rate of the photons exiting the BS on separate paths (anti-bunching) ideally drops to zero, while the proportion of detection events with photons output on the same path (bunching) increases.

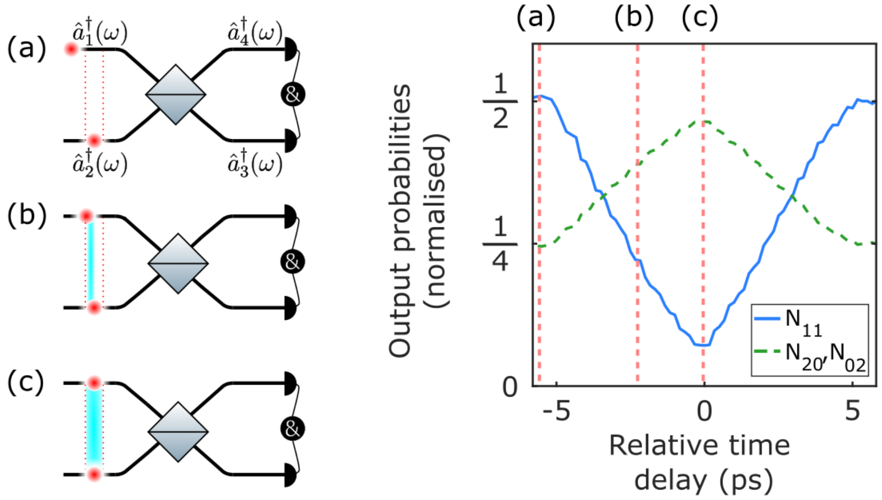

FIGURE 2.5. **Hong-Ou-Mandel inteferometer:** (a-c) Photon pairs incident on a beamsplitter with zero (a), partial (b) and complete (c) temporal overlap. Anti-bunching state (blue, N_{11}) destructively interfere while the photons get indistinguishable, bunching state (green dashed, N_{02}, N_{20}) constructively interfere while the photons get indistinguishable.

2.4.2.1 Single-mode photons interpretation

For a single-mode photon interpretation, we consider photons emitted at a unique frequency ω_k. In a Dirac notation, we can write:

$$|\Psi\rangle = \hat{a}_j^\dagger(\omega_k)\,|0\rangle = |\omega_k\rangle_j = |1\rangle_{j,k}\ , \tag{2.30}$$

where $\hat{a}_j^\dagger(\omega_k)$ is the creator operator, generating a photon in the mode j oscillating at the angular frequency ω_k. The state propagating toward the BS is given by:

$$|\Psi\rangle = \hat{a}_1^\dagger(\omega_k)\,\hat{a}_2^\dagger(\omega_k)\,|0\rangle, \tag{2.31}$$

where the indices 1 and 2 are the input modes of the HOM interferometer shown on Fig. 2.5(a). BS is a unitary operator transforming the input state as follow:

$$\begin{aligned} \hat{a_1}^\dagger(\omega_k) &= \frac{1}{\sqrt{2}}\left(\hat{a}_3^\dagger(\omega_k) + \hat{a}_4^\dagger(\omega_k)\right), \\ \hat{a_2}^\dagger(\omega_k) &= \frac{1}{\sqrt{2}}\left(\hat{a}_4^\dagger(\omega_k) - \hat{a}_3^\dagger(\omega_k)\right), \end{aligned} \tag{2.32}$$

the indices 3 and 4 are, respectively, the bottom and top modes after the beamsplitter. Hence, after transformation from the BS on $|\Psi\rangle$, we obtain:

$$|\Psi\rangle_{out} = \frac{1}{2}\left[\left(-\hat{a_3}^\dagger(\omega_k)\right)^2 + \left(\hat{a_4}^\dagger(\omega_k)\right)^2 + \hat{a_3}^\dagger(\omega_k)\,\hat{a_4}^\dagger(\omega_k) - \hat{a_4}^\dagger(\omega_k)\,\hat{a_3}^\dagger(\omega_k)\right]|0\rangle. \tag{2.33}$$

Two photons are indistinguishable when they have the same spatial modes, frequency, polarisation and time of arrival at the BS. If both photons are indistinguishable, the two operators commute and we have:

$$\left[\hat{a}_i, \hat{a}_j\right] = \hat{a}_i \hat{a}_j - \hat{a}_j \hat{a}_i = 0. \tag{2.34}$$

Then, due to the indistinguishability of the photons, we can write:

$$|\Psi\rangle_{out} = \frac{1}{2}\left[\left(-\hat{a_3}^{\dagger}(\omega_k)\right)^2 + \left(\hat{a_4}^{\dagger}(\omega_k)\right)^2\right]|0\rangle, \tag{2.35}$$

where the anti-bunching terms cancel each other. The photons bunch either in the top or bottom mode of the interferometer which is known as a NOON state [75, 77]. The probability to detect the output state $|11\rangle$ tends to 0 if the two photons are completely indistinguishable[5], whilst the probability of detecting two photons from the same detectors is 1/2. However, this single mode interpretation does not explain the pattern of the interference which is caused by the temporal shape of the photons.

2.4.2.2 Multi-mode photons interpretation

In a multi-mode photon interpretation, we consider a photon emitted over a spectrum of frequencies on a defined bandwidth. When a photon is generated at the frequency ω_k with a linewidth of $\Delta\omega$ in mode j, the representation is expressed as follow:

$$|1\rangle_{j,k} = \int^{\Delta\omega} \beta_j(\omega)\, \hat{a}_k^{\dagger}(\omega)\, d\omega\, |0\rangle = \hat{A}_{j,k}^{\dagger}(\omega)\, |0\rangle, \tag{2.36}$$

with $\int^{\Delta\omega} = \int_{\omega_k - \Delta\omega/2}^{\omega_k + \Delta\omega/2}$, $\beta_j(\omega)$ is the amplitude of the photons in the frequency domain with $\int^{\Delta\omega} |\beta_j(\omega)|^2 d\omega = 1$. We can write its representation in the time domain, where both of the domains are connected via the Fourier transformation. Hence,

$$|1\rangle_{j,k} = \int^{\Delta\tau} \beta_j(t)\, \hat{a}_k^{\dagger}(t)\, dt|0\rangle = \hat{A}_{j,k}^{\dagger}(t)\, |0\rangle, \tag{2.37}$$

with $\int^{\Delta\tau} = \int_{t_k + \Delta\tau/2}^{t_k + \Delta\tau/2}$, where $\Delta\tau$ is the temporal width of the photon. Thus Eq. (2.34) becomes:

$$\left[\hat{a}_i(t), \hat{a}_j(t)\right] = \delta(t_i - t_j), \tag{2.38}$$

giving:

$$\left[\hat{A}_{i,k}(t), \hat{A}_{j,k}(t)\right] = \int^{\Delta\tau} \beta_i^*(t)\beta_j(t)\, dt = |I_{ov}|^2 \tag{2.39}$$

where $|I_{ov}|^2$ computes the overlap of the temporal wave packets of both photons in the time domain.

Instead of doing the evolution of the wave function after transformation from the unitary operator, we can instead do an evolution of the operator (both are equivalent, and are respectively

---

[5] Which is not the case in Fig. 2.5 as the anti-bunching coincidence counts are not equal to 0. These are experimental data.

known as the Schrödinger and Heisenberg picture). We measure coincidence through the following operator:

$$\hat{N}_2(t) = \int\int_{-\infty}^{+\infty} \hat{A}_3^\dagger(t_1)\hat{A}_4^\dagger(t_2)\hat{A}_4(t_2)\hat{A}_3(t_1)\, dt_1 dt_2, \tag{2.40}$$

and after transformation given by Eq. (2.32), we have:

$$\langle\Psi|\hat{N}_2(t)|\Psi\rangle = 1 - \frac{1}{2}|I_{ov}|^2. \tag{2.41}$$

with $|\Psi\rangle$ the input state from Eq. (2.31) in a multi-mode interpretation. Hence, if we use filters (usually of Gaussian shape) the wave packets of the two photons in the input modes labelled 1 and 2 are given by:

$$\begin{aligned} \beta_1(t) &= \sqrt{\frac{\delta}{2\pi}}\, e^{-\delta^2 \frac{t^2}{2}} \\ \beta_2(t) &= \sqrt{\frac{\delta}{2\pi}}\, e^{-\delta^2 \frac{(t-\tau)^2}{2}}. \end{aligned} \tag{2.42}$$

Here, $1/\delta$ is related to the temporal width of the wave packet and τ is the time delay between the two photons. Finally, the probability to detect an anti-bunching state from the output of a HOM interferometer with the input state $|\Psi\rangle$ from Eq. (2.31) by varying the relative time delay τ between the two photons is given by:

$$\langle\Psi|\hat{N}_2(t)|\Psi\rangle = \frac{1}{2}\left[1 - \alpha e^{-\delta^2 \frac{\tau^2}{2}}\right], \tag{2.43}$$

where α is the visibility of the interference and expresses the indistinguishability between the two photons. The visibility depends on the indistinguishability between the two photons and is proportional to $|I_{ov}|^2$ from Eq. (2.39). The panel (a) from Fig. 2.6 shows HOM interference from Eq. (2.43) where the photon pair exhibits a temporal wave packet with a Gaussian shape and a full half width maximum (FHWM) of $\approx 2.4/\delta$.

The HOM interference in this thesis exhibits a triangular shape similar to the interference showed in Fig. 2.6(b). The crystal to generate the photon pairs is type-II and the photons are unfiltered. Hence from section 2.4.1, the phase matching condition for such a nonlinear crystal induces photons with a temporal wave packet in the shape of a top-hat function with a width $\tau = DL$, where L is the length of the crystal and D is the inverse group velocity of the two downconverted photons. The HOM interference can be seen as an overlap in time of the temporal wave packet, this mathematically results to a convolution between the two temporal wave packets, ending up in a triangular shape. For such photon pairs, the probability to detect the anti-bunching state is given by [110]:

$$P_{11}(t) = \begin{cases} 1/2\left[1 - \alpha\left(1 - \left|\frac{t}{\tau}\right|\right)\right], & \text{for } |t/\tau| \leq 1 \\ 1/2, & \text{for } |t/\tau| > 1 \end{cases} \tag{2.44}$$

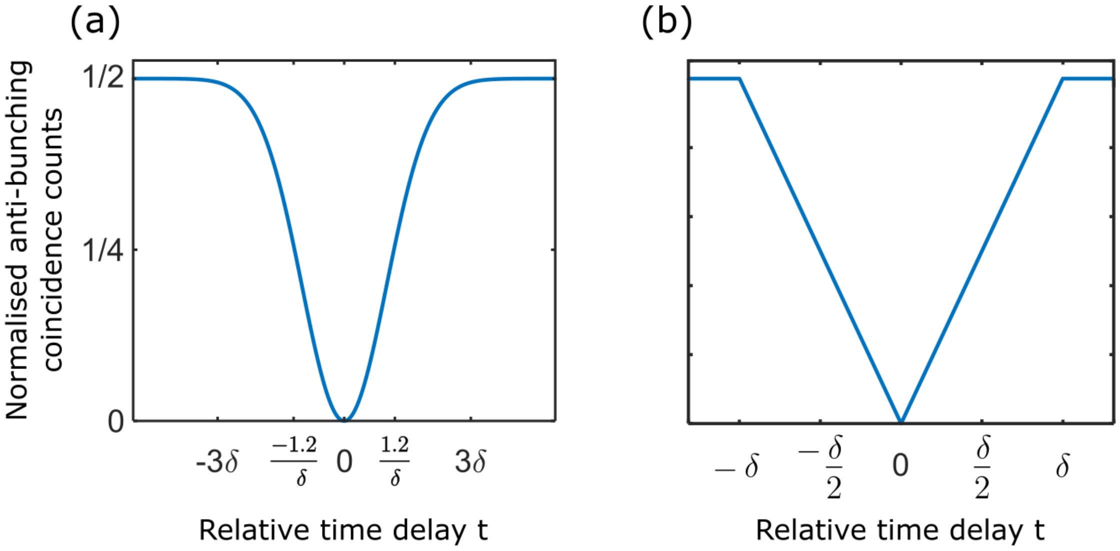

FIGURE 2.6. **Hong-Ou-Mandel interference:** HOM interference with photon pairs exhibiting a temporal wave packet with a Gaussian shape ($\sigma^2 = 1/\delta^2$) (a) and a top-hat shape (width $\tau = DL = \delta$) (b).

The HOM interference is a probabilistic event, the two photons interfering either bunch or anti-bunch. Hence, we have:

$$1 = P_{11}(t) + P_{20}(t) + P_{02}(t), \tag{2.45}$$

where $P_{02}(t)$ and $P_{20}(t)$ are the probability of detecting two photons either in the bottom or top mode after interference for a given time delay t.

During the experiment, the indistinguishability of the downconverted photons can be controlled with a crystal engineered to generate downconverted photons with the desired wavelength and at the right temperature. The crystal is placed in an oven, where the temperature is controlled with a PID controller to stabilise it. Furthermore, to match the polarisation of the downconverted photons, half and quarter-waveplates can be used before the interference occurs, whilst the spatial mode can be filtered out with single-mode fibre, however, multi-mode HOM interference has been demonstrated and can be done by matching the spatial overlap of the two photons at BS [106, 157]. The time delay is often the parameter to vary to show HOM interference. It can be controlled with a translation stage either translating the BS or one of the input modes for bulk optics experiments [106, 117] or by controlling the temperature of a waveguide for integrated photonic chips [112, 138].

2.4.2.3 Two-colour entangled photon pair source

Let us consider HOM interference obtained with a two-colour entangled photon pair source as an input state given by:

$$\begin{aligned} |\Psi\rangle &= \frac{1}{\sqrt{2}}\left(\hat{A}_1^{\dagger}(\omega_1)\hat{A}_2^{\dagger}(\omega_2) + e^{i\phi}\hat{A}_1^{\dagger}(\omega_2)\hat{A}_2^{\dagger}(\omega_1)\right)|0\rangle \\ &= \frac{1}{\sqrt{2}}\left(|\omega_1,\omega_2\rangle + e^{i\phi}|\omega_2,\omega_1\rangle\right). \end{aligned} \tag{2.46}$$

The spectrum of the input state can be seen as a superposition of two photons with a wave packet $\beta(\omega)$ centred at two distinct frequencies ω_s and ω_i and gives [35]:

$$f(\omega) = [\delta(\omega-\omega_s) + \delta(\omega-\omega_i)] * \beta(\omega). \tag{2.47}$$

As discussed previously, the HOM interference is an overlap of the temporal wave packet of the photon state. Temporal and frequency wave packets are connected via the Fourier transform [141]. The Fourier transform of the convolution of two functions $FT[f*g]$ corresponds to the multiplication of the Fourier transform of these two functions $FT[f]\cdot FT[g]$ [141]. Therefore, from the spectrum of the input state on Eq. (2.47), by applying the previous relationship, we can observe that a cosine function with a frequency of $\Delta\nu = |\omega_s - \omega_i|$ will feature in the temporal wave packet of the input state. The temporal wave packet of this entangled two-colour state can be seen as a cosine function multiplied by the temporal wave packet of the downconverted photons. From this, the temporal overlap of the new wave packets will lead to the same probability as detecting the anti-bunching state given by Eq. (2.43) and (2.44) with a cosine function in it exhibiting a spatial beat note relative to the time delay between the two photons interfering [110]. Thus for a photon pair source generated by a type-II crystal we have:

$$P_{11}(t) = \begin{cases} 1/2\left[1-\alpha\left(1-\left|\frac{t}{\tau}\right|\right)cos(2\pi\Delta\nu t)\right], & \text{for } |t/\tau| \leq 1 \\ 1/2, & \text{for } |t/\tau| > 1 \end{cases} \tag{2.48}$$

The HOM interference for such an input state exhibits a spatial beat note with a frequency $\Delta\nu$ dependant on the frequency separation between the signal and the idler [35, 109, 118]. The indistinguishability between the two photons is kept due to the entanglement of the input state and the visibility of the HOM interference becomes dependant of the entanglement fringe visibility of the quantum state. Finally, the probability of detecting the bunching terms can be found using Eq (2.45).

2.4.3 Detection of the photons pairs

An avalanche photodiode detector (APDs) is a semiconductor-based photodetector with a similar structure to a p-i-n (PIN) detector with a built-in stage for amplification through avalanche multiplication. Fig. 2.7 shows a diagram of the functioning of such a device. A photon with an energy $h\nu$ is absorbed in the intrinsic region (I) where an electron-hole pair is generated

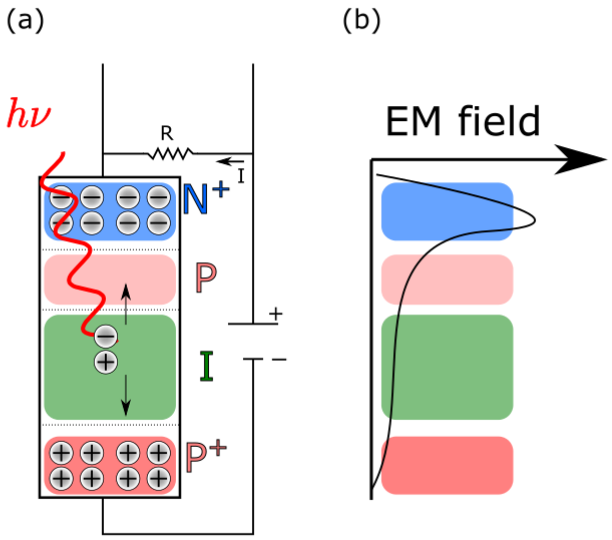

FIGURE 2.7. **Avalanche photodiode detectors diagram:** (a) semi-conductor where a high reverse voltage is applied. N^+ and P^+ are electron and hole doped regions. I and P are slightly doped regions. (b) Electromagnetic field in function of the region. The avalanche occurs in the $P-N^+$ regions and is where the multiplication of the photocurrent happens.

via the photoelectric effect. Due to the high reverse voltage applied on the semi-conductor, the holes and the electrons are, respectively, accelerated toward the P^+ and N^+ doped regions. In this case, the avalanche occurs only for the electron which is multiplied via electron impact ionisation, but depending on the semiconductor material this can vary. Finally, a voltage above the threshold (manually chosen) is measured, indicating the presence of a photon. After measuring the photocurrent, the device needs to come back to its initial state and cannot detect any photon during this lapse of time. This is known as the dead time and is typically around hundreds of ns. This limits the detection rates to $\sim 10^7\ Hz$. The rate of the generation of the photon pairs is below this threshold and was not a limiting factor in this thesis. Furthermore, APDs cannot resolve the number of photons by themselves (except under specific conditions [82]), therefore a quasi-photon number resolving detector scheme (PNRDS) has been used in this thesis [4]. To resolve multi-photon terms, PNRDS split the state into different spatial modes either with a beamsplitter, or a $1 \times n$ fused fibre couplers where each photon has a probability $1/n$ to be transmitted to one channel. Afterwards, coincidences between n detectors connected to the output of the fused single mode couplers are monitored and constitute to the detection of the multi-photon term with n photons. It can be easily implemented in an experiment for $n = 2$. However due to the scheme of detection, there is a probability that more than one photon is transmitted through the same channel, consequently the multi-photon term cannot be completely resolved. To decrease the intrinsic loss with such a detection scheme, the output channel needs to be split into more other channels, thus increasing the number of detectors and the order of coincidence counting. It requires a lot of detectors and output channels for large n, making it less practical to use in a real experiment.

In this thesis, the detectors used are *SPCM-AQRH* from *Excelitas* with a detection efficiency of ~ 45 % at 830 nm. Detectors working at low temperatures (~ K) can reduce the number of dark counts such as superconducting nanowire single-photon detector (SNSPD) with an efficiency of detection above 90 % [65, 132]. The detectors used in the chapter 3 work at room temperature, where fake detections can occur due to the thermal fluctuations within the semi-conductor. These fake counts are known as dark current or dark counts and are typically around hundreds of single counts per second for the detectors used for HOM microscopy. These can be decreased by cooling the temperature of the detector to a few K [160]. This was not necessary as the HOM microscope uses coincidence counts to estimate the thickness of the sample. Because dark counts are uncorrelated in time, the rate to measure coincidences between two dark counts within a coincidence windows is very low and can be considered as negligible. To realise it, a time-tagger electronics (or time-to-digital converter) is capable of timing each detection event with a given time bin width. The time-tagger electronic used in chapter 3 has a time bin width of 78 ps. Then, a custom control software post-process of the time tag events and calculates the number of coincidences for a given coincidence window.

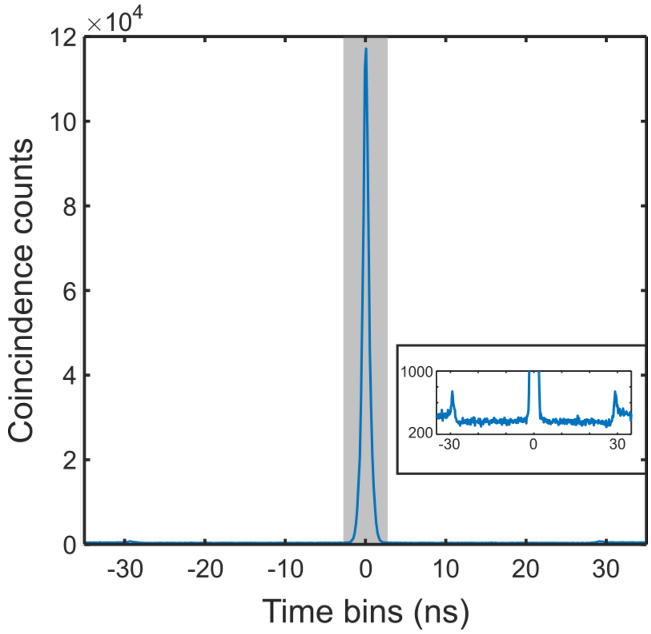

FIGURE 2.8. **Arrival time histogram of photon pairs.** The blue trace is a timing histogram of between two detectors from the output $\mathscr{A}$ and $\mathscr{B}$ in Fig. 3.12. The grey rectangle is the coincidence window of 3 ns used to monitor coincidences in chapter 3. The bottom right inset is a zoom on the Y axis showing afterpulsing effect centred at the time bin of ±30 ns.

Fig. 2.8 shows an example of a time histogram of the coincidences between two detectors with a PNRDS monitored for $\sim 5\ mins$. The blue histogram corresponds to coincidence counts between two detectors of two different outputs from the photon pair source shown from Fig. 3.12. We can observe that all coincidence counts happen in a time window of 3 ns. Therefore, for this whole thesis, the coincidence window has been set to 3 ns (grey zone). The full width half maximum of the coincidence peak is the jitter of the detector and it sets the timing resolution. The inset at the bottom right of the figure corresponds to a zoom on the Y axis to highlight the two coincidence peaks centred at the time bins $\pm 30\ ns$. These coincidence peaks result from an error in the measurement and is known as afterpulsing effect [51, 172]. This effect occurs when one of the carrier is trapped and is released at a random time, generating an avanlache process in the absence of a photon. Afterpulsing can be avoided in the measured signal by setting the coincidence window centred around the coincidence peak.

2.5 Quantum optical theory for continuous variable states

Squeezed states of light attract a huge interest in quantum technologies due to their noise properties. One can generate a squeezed state, where the noise in one quadrature of the electric field is decreased at the expense of increasing the noise of the other quadrature. Vacuum squeezed light can be generated via four-wave mixing or SPDC [162, 169]. When the two photons are indistinguishable, we consider the state as single-mode vacuum squeezed state with only even photon number terms, whilst when they are distinguishable the state resulting is known as two-mode squeezed vacuum state [9, 97]. Whilst the brightness of squeezed vacuum state for spontaneous emission is of a thousand to up millions of photons per pulse [6, 76, 111], this scheme can be amplified further by adding a cavity such as in optical parametric oscillation (OPO) [50] or in a single pass scheme known as an optical parametric amplifier [29]. The last one requires ultrashort pulses where such a state has been used for stimulated Raman spectroscopy [29] and has experimentally demonstrated the highest squeezing value achieved up to date [151].

Another technique to generate squeezed light is through Kerr squeezing [159]. It is a non-linear process from the third order $\chi^{(3)}$. Kerr squeezing is inherently phase-matched and is more flexible concerning the wavelength of the signal compared to vacuum squeezing. In this section, we discuss Kerr squeezing to generate bright amplitude squeezed light. It allows the displacement of a coherent state to a squeezed state via self-phase modulation with an output power of $\sim 200 \mu W$ to be experimentally achieved [9, 13, 130].

2.5.1 Kerr squeezing with photonic crystal fibre

Kerr squeezing is a non-linear process from the third order. A bright coherent beam interacts with a non-linear medium, here a photonic crystal fibre (PCF), to generate a bright amplitude squeezed state. PCF makes an excellent candidate for Kerr squeezing as it provides tight confinement in a small core with a higher $\chi^{(3)}$, low loss and long interaction lengths compensating the weak interaction. This non-linear effect needs more power than SPDC described in the section 2.4.1 to achieve non-linearity. Therefore ultra-short pulses were used as an input beam for the generation of Kerr-squeezed light and have demonstrated higher levels of squeezing than cw probe beam [159].

PCF is a centrosymmetric medium and $\chi^{(2)}$ vanishes, therefore the polarisation defined in Eq. (2.22) for such a medium can be written as:

$$\mathbf{P} = \varepsilon_0 \left(\chi^{(1)} + \chi^{(3)}\mathbf{E}\mathbf{E}\right)\mathbf{E}. \tag{2.49}$$

If the frequency of the input beam oscillates at a frequency ω_0 far away from the absorption band, then $\chi^{(3)}$ can be considered to be real and the effect of the non-linear susceptibility is to only modify the refractive index n. From the Kerr-effect we can write the refractive index of the medium depending of the intensity I whilst the pulse propagates. This is defined as [8]:

$$n = n_0 + n_2 I, \tag{2.50}$$

where $n_0 = \sqrt{1+\chi^{(1)}}$ is the linear refractive index of the medium and $n_2 = 3\chi^{(3)}/4n_0^2\varepsilon_0 c$ is known as the non-linear refractive index. The pulses propagating within the fibre experience an additional nonlinear phase shift from n_2 which is given by [8]:

$$\Phi_{NL} = \gamma L \langle P \rangle, \tag{2.51}$$

with the nonlinear coefficient $\gamma = \omega_0 n_2 / cA$, $\langle P \rangle$ the average peak power over an area A and L the length of the nonlinear medium. Hence, the PCF can be engineered to generate optical soliton squeezed light from Kerr squeezing. This was demonstrated for the first time in 1996, achieving up to 4.3 dB of amplitude noise reduction and an output power of 0.15 mW [130]. The dispersion within the fibre can decrease the efficiency of the generation of the squeezed state, thus the fibre can be engineered to generate a squeezed soliton where temporal and spatial dispersion can be overcome by the non-linearity [28, 122]. Fig. 2.9(a) shows a diagram of the Kerr effect with the PCF as a non-linear medium. The Sagnac interferometer allows the input beam to propagate within the same non-linear medium with an anti-clockwise (AC) and clockwise propagation (C) and was first proposed by Shirasaki & Haus in 1990 [137]. However, it has been demonstrated that unbalancing the splitting ratio of the beamsplitter improves the noise reduction from the squeezed state. The first to demonstrate Kerr squeezed light with an unbalanced non-linear interferometer with a Sagnac configuration was Schmitt et al. in 1998 [129]. In their work, they demonstrated that the highest noise reduction achievable can be done with a splitting ratio 92.5 : 7.5, where we approach it in Fig. 2.9(a) with a splitting ratio of 90 : 10. A bright coherent beam (AC) interacts with a medium triggering the $\chi^{(3)}$ non-linearity. Through self-phase modulation (SPM), the coherent input state is rotated by an angle depending on its amplitude in the quadrature space as shown on Fig. 2.9(b). To generate an amplitude squeezed state of light, SPM is not sufficient and the state needs to be displaced to allow a noise reduction in the direction of the amplitude quadrature [86, 95, 139]. Thus, another coherent beam (C) not bright enough to trigger the non-linearity of the medium propagates clockwise within the interferometer and interfere with the AC pump beam at BS. The interference between the two directions of propagation results in a displacement of the AC beam in the quadrature space, ending up with an amplitude-squeezed state at the output of the Sagnac interferometer as shown in Fig. 2.9(c).

Finally, the PCF used in chapter 4 to demonstrate precision enhancement for absorption microscopy with bright amplitude squeezed light can generate up to $-4\ dB$ of noise reduction (simulation from [14] for this specific fibre), but with the loss and the third order chromatic dispersion, a maximum of $\sim -1.6\ dB$ amplitude squeezed light can be experimentally achieved [14]. A difference between the theoretical noise reduction and the experimental achievements was reported and it was caused by the third-order dispersion of the ultra-short pulses [14]. The third-order dispersion broadens the optical pulses and decreases the power of the light propagating within the PCF. Therefore the non-linear interaction is weakened and the generation of amplitude squeezed light depending on this non-linear process is degraded.

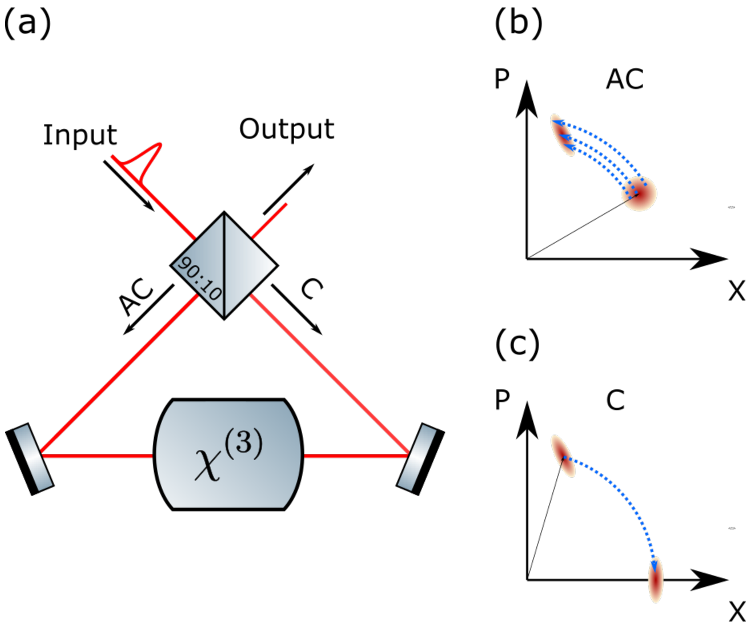

FIGURE 2.9. **Kerr squeezing for photonic crystal fibre.** (a) A bright coherent beam propagates anticlockwise (AC) within the Sagnac interferometer within a medium to trigger the $\chi^{(3)}$ non linear effect. Via self-phase modulation, the coherent beam experiences noise reduction as shown in (b). A second beam propagates within the Sagnac in the clockwise direction and is not bright enough to trigger $\chi^{(3)}$ effect. At the beamsplitter, the C and AC interfere, resulting in a displacement in the quadrature space of the AC beam to be amplitude-squeezed as shown in (c).

2.5.2 Detection of the squeezed light

In chapter 4 direct detection is used to detect squeezed light. In most of the experiments using squeezed light, homodyne detection with balance detectors is preferred over direct detection. It allows comparison of the signal beam (squeezed light) to a reference beam (local oscillator, LO) by interfering them on a beamsplitter and measuring the subtraction from balanced detectors [131]. By adjusting the relative phase between the beams, it is possible to select the quadrature that we wish to measure. However, this requires a local oscillator brighter than the signal beam. This is because the subtracted photocurrent is proportional to the intensity of the LO, increasing the signal-to-noise ratio for bright LO [68]. Therefore, due to the brightness of the signal beam $\sim 200\mu W$ (corresponding to a peak power of 25 W), direct detection has been chosen instead of homodyne detection.

The direct detection uses PIN detectors (*Thorlabs*, *PDB440A-AC*) with a quantum efficiency (QE) of $\eta_q = 0.85$. The QE corresponds to the ratio between the number of photon propagating to the detector and the number of electron converted via the photoelectric effect. Not detecting a photon is the same than losing the photon from absorption within the experiment. Therefore, a detector with a QE of η can be seen as a perfect detector with a beamsplitter exhibiting a transmission $\sqrt{\eta}$ [95]. Because squeezed light does not perform well with loss as discussed in section 4.5.1, a high QE is necessary and it was the reason why these detector has been chosen. Compared to the APDs from Fig. 2.7, PIN detector is a semiconductor composed of two heavily n-type and p-type doped regions with an undoped intrinsic region in between. The reverse voltage does not need to be as high as in the case of the APD as there is no avalanche multiplication in the detection of the photons. Because of the absence of the avalanche process, PIN detectors are less sensitive than APDs but can deal with higher level of brightness [84].

CHAPTER 3

SUB-MICROMETRE AXIAL PRECISION DEPTH IMAGING WITH ENTANGLED TWO-COLOUR HONG-OU-MANDEL MICROSCOPY

The Hong-Ou-Mandel (HOM) effect is a widely known and used quantum interference that has proved its usefulness in quantum photonics. When two indistinguishable photons are transmitted toward two different inputs of beamsplitter, the photons exit through the same output (they bunch) as the relative arrival time of the photon is reduced to zero. Therefore, it has been originally discovered to measure subpicosecond time interval (t) between two photons (and by consequence the length of the photon wave packet) produced by spontaneous parameter down conversion. Hence, HOM interference is of interest to generate $NOON$ states, showing a quantum advantage in the sensitivity for phase estimation [5, 75] or for quantum imaging [77, 108]. Quantum computing has taken advantage of HOM interference for photonic two-qubit quantum logic gates [70, 107, 115] and it is the underpinning physical phenomena of optical quantum computational advantage experiments [170].

For applications of the HOM effect to imaging and sensing, more recent demonstrations have extracted higher sensitivities to measure t with attosecond precision [99], and have utilised the effect for polarisation measurements [67], spectroscopy [36], multi-mode depth imaging [106] and refractive index measurement [120]. In these works, the Cramér Rao bound (CRB) relates the Fisher information ($\mathscr{F}(t)$) to the variance (σ_t^2) of a measurement through the inequality $\sigma_t^2 \geq 1/\mathscr{F}(t)$. The limit of this bound quantifies the maximum achievable precision σ_t for an unbiased estimator measuring t. $\mathscr{F}(t)$ can be modelled from analytic probability functions $P_i(t)$, with $\{i = 11, 02, 20\}$ corresponding for the bunching and anti-bunching events describing the HOM interference:

$$\mathscr{F}(t) = \sum_i \frac{1}{P_i(t)} \left(\frac{\partial P_i(t)}{\partial t} \right)^2, \tag{3.1}$$

which highlights the dependence on the maximum precision bound on the shape of the interference features given by $P_i(t)$. For degenerate photons, $\mathscr{F}(t)$ can be increased by broadening the photon spectrum to yield steeper HOM interference features [99]. However, increasing the bandwidth of photons leads to a tradeoff between measurement precision and dynamic range, while highly broadband photons can also exacerbate complications arising from dispersion in the apparatus optics. While sensitivity to dispersion is addressed by some terahertz pulsed imaging techniques which are widely use in bio-imaging, these can suffer from other issues such as comparatively poor lateral and axial resolution [33, 73, 161]. More broadly, for many high-precision classical imaging techniques, such as super-resolution microscopy, the intensity of illumination required to achieve sub-micron level precision is between 8 and 12 orders of magnitude greater than the microscope proposed in this chapter [114, 128]. Consequently, the HOM microscope can reach a higher Fisher information per photon, which can be an important consideration for photo-sensitive samples and can otherwise be a limiting factor for measurement precision. In this chapter, the alternative to increase the HOM interferometer sensitivity is to use an entangled two-colour state [35, 118] where a beat note within the interference appears for which its frequency is given by the spectral separation of the downconverted photons. The frequency separation is controlled by changing the temperature of a single non-linear crystal, changing the phase-matching condition of the spontaneous parametric down conversion process. It allows a detuning from 0 to 30 THz (60 nm) without tuning the wavelength of the pump laser.

The chapter is written as follows: first, depth imaging with Hong-Ou-Mandel interferometry is described in section 3.2. It shows how HOM interferometry can achieve depth imaging by monitoring the relative time delay induced by the thickness of a sample, where 2D imaging is performed with confocal microscopy. Section 3.3 is dedicated to parameter estimation. It investigates an estimator based on Bayesian inference, and then a maximum likelihood approach is used to infer the relative thickness of the sample from the output of the HOM interferometer. The Fisher information is defined and shows through the Cramér-Rao bound that the estimator used is optimal by saturating the bound. Sections 3.4 and 3.5 describe the two photon pair source used for HOM interferometry. It shows that by using a two-colour entangled photon pair source, one can achieve a beat note within the HOM interference, increasing the Fisher information and therefore the precision of the microscope. Section 3.6 demonstrates depth imaging with a two-colour entangled state where sub-μm axial precision is experimentally demonstrated with 10^4 photon pairs detected. The performances of the microscope are experimentally characterised with the use of the Fisher information. Finally, section 3.7 proposes future work to improve the performance of the microscope based on the experimental results from the previous sections. It describes HOM microscopy with high dynamic range for single-shot measurement whilst fringe ambiguity can be avoided, delivering a robust quantum microscope with $\sim fW$ probe of illumination on a sample with high resolution. This could enable depth imaging for live biological samples that are highly sensitive to light exposure.

3.1 Statement of the work

Alex McMillan was my day to day supervisor. Jonathan Matthews was the coordinator of the experiment. The single-mode filtering and the wavelength-entangled photon pair source to achieve a beat note within the HOM interferometer were his ideas. The degenerate photon pair source and HOM interferometer was originally built by Mateusz Piekarek, where I applied some modification, changed components and the architecture of the HOM to make it more compact and brighter. I designed and built the wavelength-entangled photon pair source. I did the active phase-locking, where Giacomo Ferranti kindly lend me the PID controller from his experiment. I did the data acquisition/analysis. I designed the KET sample and Jorge Monroy-Ruiz made it. The fish scale was given by Martin Genner from the University of Bristol. Section 3.6.5 and 3.6.6 relate to the published manuscript with the doi:10.1103/PhysRevA.108.023726, and this manuscript is from my work made during my PhD.

3.2 Quantum imaging with Hong-Ou-Mandel microscopy

As discussed in section 2.4.2, the Hong-Ou-Mandel (HOM) effect is a two-photon quantum interference characterised by an increase in the measured bunching coincidence rates (n_{20} and n_{02}) and a decrease of the anti-bunching coincidence rate (n_{11}) at the output of the interferometer when the two photons become indistinguishable. It was originally used to measure a subpicosecond time delay between two photons of the same pair [72]. The two photons become indistinguishable when they exhibit the same polarisation, the same spatial mode, the same wavelength (if the input state is wavelength-entangled, the indistinguishability is still maintained despite different wavelengths between the two photons, see section 2.4.2.3) and the same time of arrival at the beamsplitter (BS). Depth imaging with such quantum interference is possible due to the variation in thickness on a semi-transparent sample. Fig. 3.1(a) shows a HOM interferometer where each photon of a pair is transmitted through the input path $\mathscr{C}$ and $\mathscr{D}$. A semi-transparent sample with a thickness ΔL and with a refractive index n_2 is added on the input path $\mathscr{D}$. The sample is between two lenses in a confocal configuration and allow raster-scan imaging by translating the sample on a 2D plane orthogonal to the direction of propagation of the probe photon. Fig. 3.1(b)

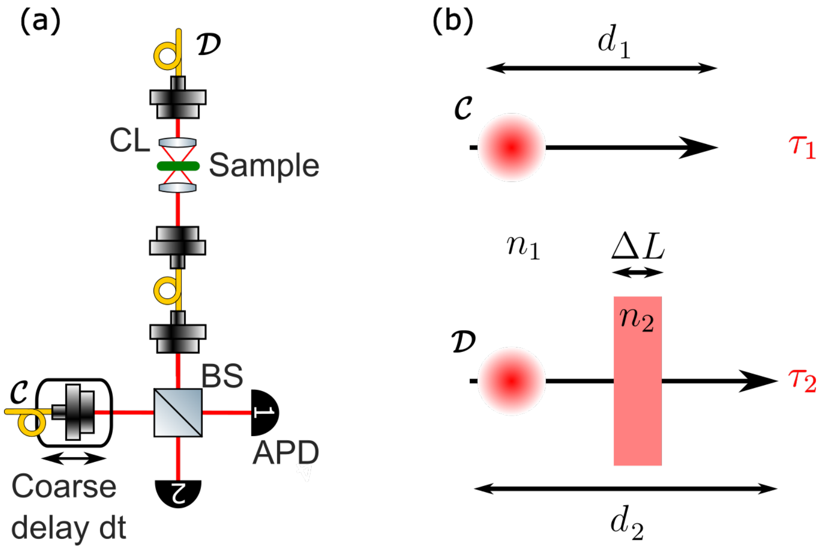

FIGURE 3.1. **Hong-Ou-Mandel microscope.** (a) HOM interferometer with the reference photon (input $\mathscr{C}$ with a translation stage to control the coarse delay dt), and the probe photon (input $\mathscr{D}$ with the sample between two lenses in a confocal configuration). The anti-bunching coincidence counts (N_{11}) are monitored while the sample is raster scanned in a 2D-plane with motorised stages. (b) Time of propagation τ for both photons. The probe photon (from input $\mathscr{D}$) propagates through a medium with a refractive index $n_2 \neq n_1$ and a thickness ΔL.

illustrates the travel time τ for both photons before they reach the BS and which are given by:

$$t_1 = \frac{d_1 n_1}{c}, \tag{3.2}$$

$$t_2 = \frac{(d_2 - \Delta L) n_1}{c} + \frac{\Delta L n_2}{c}, \tag{3.3}$$

where c is the speed of the light, n_1 is the refractive index of air, d_1 and d_2 are, respectively, the length of the inputs $\mathscr{C}$ and $\mathscr{D}$ paths before the BS. Hence, the time difference between the two photons Δt is given by:

$$\Delta t = \frac{n_1 \Delta d}{c} + \frac{\Delta L}{c} \Delta n, \tag{3.4}$$

where $\Delta d = d_2 - d_1$ and $\Delta n = n_2 - n_1$. The change in the temperature can cause a variation in the optical length of the fibres used in the HOM microscope affecting Δd, however because the temperature of the environment is controlled $\Delta d << \Delta L$. We can assume that only the variation in thickness ΔL of the semi transparent sample causes variation in the relative time delay Δt, which can be inferred by monitoring the anti-bunching coincidence counts N_{11} at the output of the interferometer.

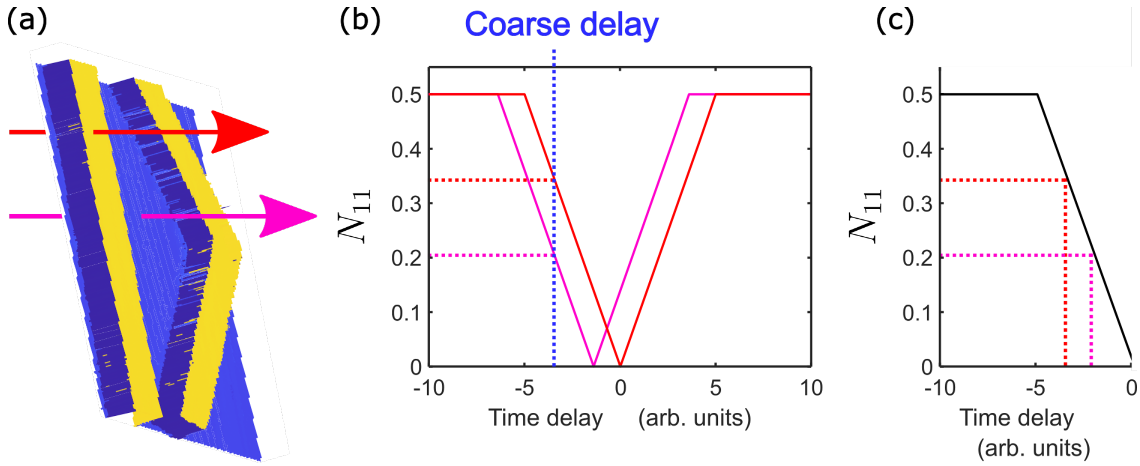

FIGURE 3.2. **Depth imaging with Hong-Ou-Mandel interference.** (a) Sample with variation in its thickness ΔL between two steps (blue and yellow). (b) N_{11} are monitored whilst the coarse delay from Fig. 3.1(a) on input $\mathscr{C}$ moves toward the beamsplitter when the probe photon transmit through the yellow step (red plot) and blue step (magenta plot). Then, the coarse delay is set to a position (blue dashed line) and the N_{11} for each step are monitored (red dashed line for yellow step and magenta dashed line for blue step). (c) N_{11} for both steps is reported to a reference interferogram (half fringe in black). The time delay τ for each step can be inferred from it.

Fig. 3.2 shows how the variation in the thickness ΔL is measured with HOM microscopy on a semi-transparent sample. In (a) the sample exhibits a variation in thickness on two steps in the shape of a "KET". The probe photon from Fig. 3.1(a) on the input $\mathscr{D}$ is transmitted through two different steps, either the yellow step (red arrow) or the blue step (magenta arrow). This can be done by moving the translation stages holding the sample in the confocal microscope. Panel (b) reports their corresponding interferogram by monitoring N_{11} in both cases whilst the translation stage on $\mathscr{C}$ moves toward the BS. The horizontal shift is caused by the relative time delay between these two steps caused by the thickness ΔL of the sample. It is equivalent to removing the sample and adding a fine translation stage for which between the two measurements the translation stage has been moved by $\Delta L = c\Delta t/\Delta n$ from Eq. (3.4). Taking HOM interferences for every single-pixel of the sample to compare the time shift between every interferogram would be too long and unnecessary as the amount of Fisher information would not be optimised. Subsequently, the coarse delay (blue dashed line) is set to a position within the dip to avoid fringe ambiguity. Fringe ambiguity occurs when the measurements between each pixel are not within the same half fringe of the interference [1]. Fig. 3.2(c) displays the measurements of the N_{11} from both steps (red and magenta dashed lines) on a reference HOM interferogram and we assume no fringe ambiguity. Fringe ambiguity can be avoided from two pieces of knowledge: 1) the half-period of the HOM interference, and 2) the order of magnitude in the variation thickness which can be approximated from the shift of the two interferograms in (b). Afterwards, depth imaging with HOM interferometry can be done by monitoring the anti-bunching coincidence counts for every pixel by raster-scanning the sample in the confocal microscope.

Furthermore, the HOM microscope presented in this thesis has one single-mode fibre between the sample and the BS to filter the spatial mode after transmission of the probe photon. Otherwise, due to the roughness of the sample, the photon transmitting through the sample has its path slightly deviated. This path deviation will cause a miss overlapping of the spatial mode at the BS between the two photons interfering, and therefore it will decrease the visibility of the interference. Because this strategy of measurement relies on counting coincidences whilst the sample is raster-scanned, there is no way to distinguish a drop of coincidence counts either due to the thickness of the sample or due to a drop of visibility. Therefore the miss-overlapping of the two photons will cause artefacts to the measurements (see section 3.6.2). For such an entangled input state, the HOM interference exhibits a beat note with a frequency of oscillation proportional to the frequency separation between the signal and the idler (discussed in section 2.4.2.3). Thus, the Fisher information can be tuned by controlling the wavelength separation of the two photons, increasing the precision and the dynamic range of the microscope whilst fringe ambiguity can be avoided. This imaging technique can provide depth imaging with confocal microscopy experimentally demonstrated in the section 3.6.5 and where sub-μm axial precision has been demonstrated with $\sim 10^4$ photon pairs detected in the section 3.6.6.

---

[1] Note: In the absence of the beat note, the term "half-fringe" corresponds to one half of the HOM interference.

3.3 Parameter estimation

As discussed previously, the variation in the sample's thickness ΔL is inferred from the change in the anti-bunching coincidence counts N_{11} at the output of the interferometer. As the HOM effect depends on the detection of coincident photons, all results in this section (and chapter) estimating the relative time delay measured with the interferometer consider only photons which are post-selected on successful detection. Hence, $P(N_{11}|t)$ is the probability to detect N_{11} photons function of the relative time delay t, where:

$$P(N_{11}|t)+P(N_{02}|t)+P(N_{20}|t)=1. \tag{3.5}$$

N_{02} and N_{20} are the bunching coincidence counts, and for N photon pairs detected, we have:

$$N_{11}+N_{20}+N_{02}=N. \tag{3.6}$$

In this section, the Bayesian approach has been investigated to estimate the parameter t over the distribution of the photon pairs between the anti-bunching and bunching states. Then a frequentist approach with a maximum-likelihood estimation is introduced, explaining how the thickness of the sample can be inferred from the output of HOM interferometry. Furthermore, the Fisher information is used to quantify the performances of such estimator, for a degenerate and two-colour entangled state where the estimator is considered as optimum by saturating the Cramér-Rao bound. Finally, a method using the Klyshko efficiency is described and has been used in this chapter to avoid any artefacts within the estimations due to unbalance detections caused by misalignment between the two outputs of the HOM interferometer.

3.3.1 Bayesian inference approach

The Bayesian inference is a method of statistical inference, derived from Bayes' theorem (see section 2.3.1) [155]. It consists of assuming a probability distribution for the parameter t over the observable N_{11} that we measure from Hong-Ou-Mandel (HOM) interferometry. Then, for each measurement, the density probability to estimate t dependent on N_{11} is updated after each measurement and correspond to one Bayesian loop. A Bayesian loop can be repeated several times to decrease the standard deviation (*i.e.* the error) of the measurements until the desirable resolution is reached. The numerical simulation for the Bayesian inference is modelled by two main functions.

The sampling function shown in Fig. 3.3 models the measured probability of the anti-bunching coincidence counts Pm_{11} from HOM interference. First, a number of downconverted photon pairs N_{tot} is generated. Spontaneous parametric down conversion (SPDC) is the non-linear effect considered in this chapter to generate the photons pairs. SPDC is a low efficient process, and therefore the generation of N_{tot} follows a Poissonian distribution with $\lambda = N$, corresponding to the average of photon pairs generated for each trial. Then, the anti-bunching coincidence counts

N_{11} and the bunching coincidence counts N_{02} and N_{20} are sampled from the HOM interference modelled by a binomial distribution $\mathscr{B}(N_{tot}, P_{11})$, where P_{11} is the probability of the HOM interferometer to output N_{11}, for an input N_{tot} of photon pairs in the interferometer. Afterwards, to model the detection of the bunching and anti-bunching terms, quasi photon number resolving detectors scheme (PNRDS) is modelled through binomial distributions. Each state is detected with a probability D_i, where i refers either for N_{11}, N_{20} or N_{02}. The detection of probability depends on the loss and the detection efficiency of each single photon detector. Not detecting a photon because the photon is lost during its travel time is equivalent to not detecting the photon because of the detector inefficiency. For the bunching state, due to the PNRDS there is an intrinsic loss of $1/n$ for a scheme splitting each output of the interferometer into n different channels with a single photon detector at the end of each of the channels. This intrinsic loss is due to the probability of both photons from the bunching state to be transmitted to the same channel, subsequently the state cannot be resolved from a single photon detector. Finally, the

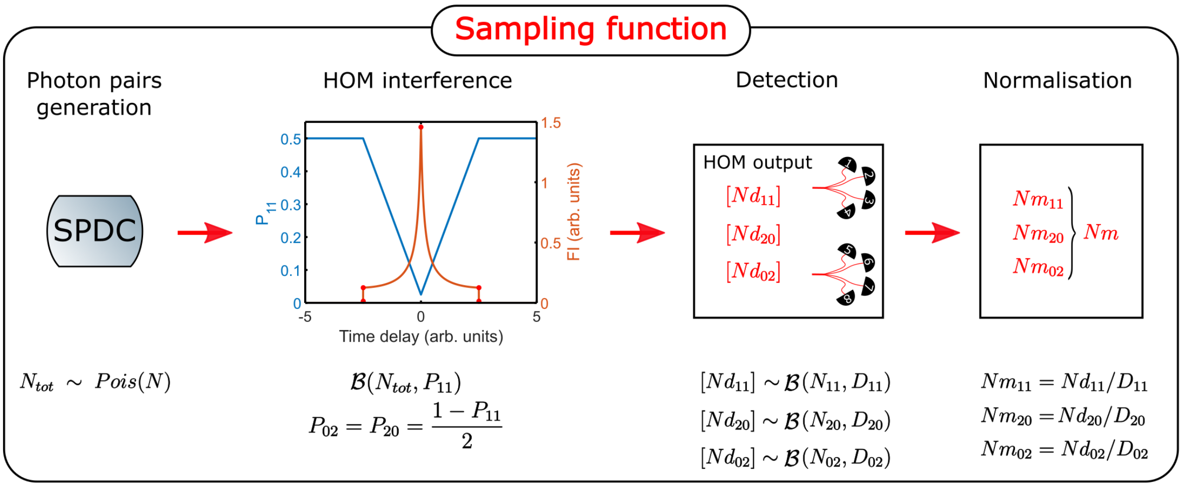

FIGURE 3.3. **Sampling functions diagram.** Numerical simulation of the sampling method. The downconverted photon pairs are generated through SPDC process following a Poissonian distribution. Then, following a binomial distribution, anti-bunching (N_{11}) and bunching coincidence (N_{02} and N_{20}) counts are sampled. HOM interference is given by Eq. (2.48) (left axis, blue trace) with its corresponding Fisher information (right axis, orange trace) whilst the red dots correspond to coordinates where the Fisher information is not defined due to the discontinuity of the HOM function. The detection is done with quasi-photon number resolving scheme following a binomial distribution with their probability D to be detected. Then, the coincidence counts are normalised where the probability of detection for each coincidence counts can be estimated through Klyshko coefficients K (defined in section 3.3.5).

bunching and anti-bunching detected coincidence counts are normalised with the use of Klyshko efficiency as described in section 3.3.5. The probability Pm_{11} is given by:

$$Pm_{11} = \frac{Nm_{11}}{Nm_{11} + Nm_{02} + Nm_{20}}, \tag{3.7}$$

where Nm_i corresponds to the coincidence counts of the anti-bunching or bunching state after correction from Klyshko coefficient, whilst the bunching state are corrected from the intrinsic loss caused by the PNRDS.

To sample from a binomial distribution MATLAB uses the n-choose-k function given by:

$$C_k^n = \frac{n!}{k!(n-k)!}. \tag{3.8}$$

For a large number of photons N_{tot} (n), this can take very long to compute. Therefore, to decrease the time of computation, the Stirling's approximation is used and given by [121]:

$$ln(n!) \approx n\ln(n) - n, \tag{3.9}$$

hence we can write

$$C_k^n \approx \frac{n^n}{k^k(n-k)^{(n-k)}}. \tag{3.10}$$

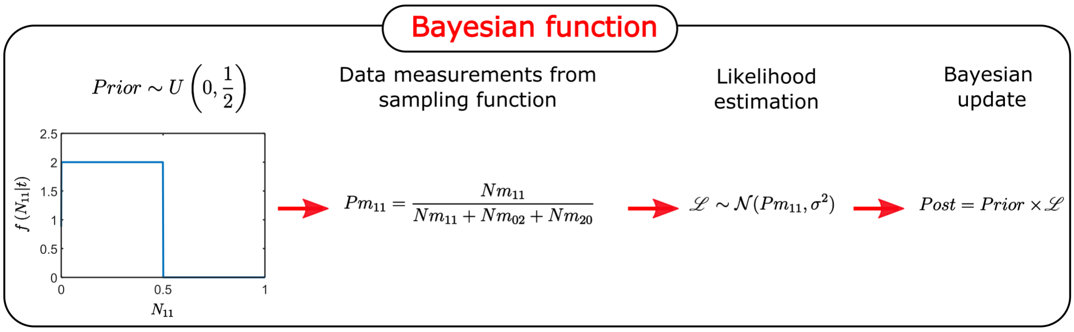

FIGURE 3.4. **Bayesian function diagram.** First the $Prior$ is defined by a uniform distribution $U\left(0, \frac{1}{2}\right)$. Then, the probability of anti-bunching coincidence counts Pm_{11} is estimated using the sampling function from Fig. 3.3. The Likelihood distribution $\mathscr{L}$ is computed. Finally the new $Prior$ for the next Bayesian loop is given by the $Posterior = Prior \times \mathscr{L}$

Secondly, Fig. 3.4 describes the script modelling the Bayesian update. The probability of the anti-bunching coincidence counts P_{11} is between 0 and 1/2 for HOM interference with degenerate photon pairs. Thus the $Prior$ can be defined by an uniform distribution $U(0, 1/2)$ where P_{11} can take any value within this interval. Then Pm_{11} is sampled from the sampling function described on Fig. 3.3. Afterwards, a likelihood estimation from the measured outcome Pm_{11} is inferred. The likelihood function $\mathscr{L}$ is a binomial distribution and is given by:

$$\mathscr{L}(p|n,k) = \binom{n}{k} p^k (1-p)^{(n-k)}, \tag{3.11}$$

where p is the probability of measuring the anti-bunching coincidence counts given by Pm_{11}, n is the total number of photon detected given by $Nm = Nm_{11} + Nm_{02} + Nm_{20}$ and k the total number anti-bunching coincidence counts detected Nm_{11}. Because the number of photons is large ($Nm >> 1$), we can use the central limit theorem where the likelihood function can be approximated to a normal distribution $\mathcal{N}(\mu,\sigma^2)$ with [27]:

$$\mu = Pm_{11} \tag{3.12}$$

$$\sigma^2 = Pm_{11} \times \frac{1-Pm_{11}}{Nm} \tag{3.13}$$

$$\mathcal{N}(\mu,\sigma^2) = \frac{1}{\sigma\sqrt{2\pi}} e^{-\frac{(x-\mu)^2}{2\sigma^2}}. \tag{3.14}$$

Finally, the $Posterior$ is updated by multiplying the $Prior$ to the likelihood $\mathscr{L}$ and it gives the $Prior$ for the next Bayesian update, also called Bayesian loop.

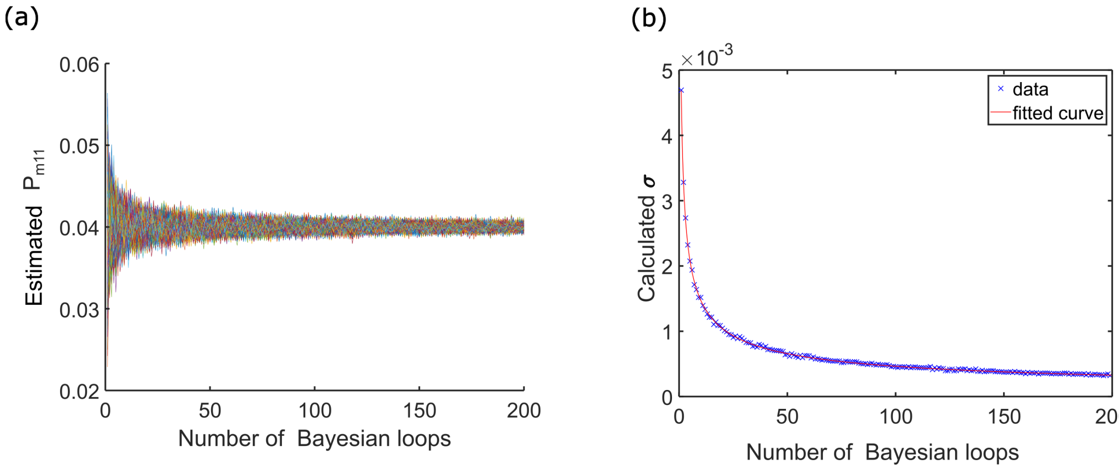

FIGURE 3.5. **Numerical simulation for Bayesian inference.** (a) Each trace is the anti-bunching probability P_{11} estimated using the sampling and Bayesian function described in Fig. 3.3 and Fig. 3.4 for each step of the Bayesian loop. (b) Calculated standard deviation from (a) between the traces for each step of the Bayesian loop and the true value P_{11}. The function is fit following a power function $f = ax^b$ according to Eq. (3.13), with $a = (4.68 \pm 0.03) \times 10^{-3}$ and $b = (-5.02 \pm 0.02) \times 10^{-1}$ and a R-square of 99.92 %.

With these two functions described above, the probability P_{11} is estimated for HOM interferometry. The parameter N from the sampling function corresponds to the number of photon pairs generated by the non-linear crystal for each trial and it follows a Poissonian distribution. This parameter takes in account the loss from the heralding efficiency and the coupling efficiency between fibres before the detection. Increasing the heralding and/or the coupling efficiencies results of having more photons pairs per second and will help to achieve a better precision for a smaller acquisition time. This imaging technique requires monitoring P_{11} for each pixel of the sample, therefore assuming a long acquisition time is not realistic. The measurements in this chapter were $\sim 10^4$ photon pairs detected for an acquisition time of 0.5 s. Hence, for this simulation, $N = 5000$ is chosen and corresponds to a data acquisition of 0.25 s per pixel for a source with the same brightness than the one reported in this chapter. The second parameter is P_{11} which has been set to $P_{11} = 0.04$. It corresponds to a probability of distribution where the Fisher information is high, and therefore the precision on the estimate can be maximised. The probability distribution of the HOM interference is given by Eq. (2.44) in this simulation and is characterised from a V-shape function due to the nature of the quasi phase-matching (see section 2.4). The visibility of the interference is set to 95% and corresponds to the best visibility achieved with the HOM interferometer presented in the experimental section of this chapter. Changing the shape or the visibility of the HOM interference will change the Fisher information and the probability for which the Fisher information is high. However, in an experiment this knowledge is accessible by scanning a HOM interference before processing the raster-scan imaging on the sample. The third parameter is the efficiency of the detector η. The single photons detectors used in this chapter are avalanche photodiode detectors, operating at wavelength $\lambda \sim 800\ nm$. At this wavelength, the efficiency of the detector is $\sim 60\ \%$. Then, a total of 8 detectors is used for the PNRDS (4 for each output). From this scheme, we know that 25 % of the bunching state will not be resolved and this number is used to correct the intrinsic loss. The detection scheme for this simulation uses the same characteristics of the experimental setup from this chapter, where the efficiency η_i of the i^{th} detector is randomly chosen by following an uniform distribution $U(0.55, 0.65)$.

Fig. 3.5(a) shows an estimate of P_{11} with the two functions described above. The eqstimates are plotted for each step of the Bayesian inference with a total number of 200 Bayesian loops. This has been repeated 1000 times to model the behaviour of the Bayesian inference. We can see that the estimates converge to the true value $P_{11} = 0.04$ when the number of Bayesian loops increases. Then, using these 1000 traces, the standard deviation around the true value is calculated for each number of the Bayesian loops and the results are reported in Fig. 3.5(b). The data points are fit to a power function $f(x) = ax^b$, with $a = (4.68 \pm 0.03) \times 10^{-3}$ and $b = (-5.02 \pm 0.02) \times 10^{-1}$ for a confidence interval of 95% and a R-square of 99.92 %. We can see that the standard deviation σ is dependant of the square root of the number of Bayesian loop. The number of detected photons pairs for each step of the Bayesian inference is ~ 1400 (according to the efficiency of the detectors and the intrinsic loss from the PNRDS). Hence, we can see that the dependence of the standard deviation is $\sim 1/\sqrt{Nm}$ as we would expect it from Eq. (3.13). This corresponds to the shot-noise limit for which the standard deviation for N measurements is proportional to the inverse square root of the number of photons ($\sigma \sim 1/\sqrt{N}$). Therefore, the Bayesian inference is shot-noise limited and a Bayesian inference of N loops in this simulation is equivalent to the frequentist interpretation with one measurement and the same number of detected photon pairs. Subsequently, the estimates in the following sections are not using the Bayesian inference for the reasons cited previously.

3.3.2 Maximum-likelihood estimation

HOM interference leads to a probability distribution P_{11} of the anti-bunching coincidence counts N_{11} for a relative time delay t between the two photons interfering at beamsplitter. As discussed in the section 2.4.2, for a type-II non-linear crystal P_{11} is defined by:

$$P_{11} = \begin{cases} 1/2 \times \left[1-\alpha\left(1-\left|\frac{t}{\tau}\right|\right)\right], & \text{for } |t/\tau| \leq 1 \\ 1/2, & \text{for } |t/\tau| > 1 \end{cases} \tag{3.15}$$

Where α is the visibility of the HOM interference and τ the temporal width of the photons. After the interference, three outcomes are possible; 1) each of the photon anti-bunch (N_{11}), 2) photons bunch in one output of the interferometer (N_{02}) and 3) photons bunch in the other output of the interferometer (N_{20}). Hence, we have:

$$\sum_i P_i = 1, \tag{3.16}$$

with $i = \{11, 02, 20\}$. P_{02} and P_{20} are equiprobables, therefore from Eq. (3.16) we can find:

$$P_{02} = P_{20} = \frac{1-P_{11}}{2}. \tag{3.17}$$

As the HOM effect depends on the detection of coincident photons, all results in this chapter for estimating the thickness of the sample consider only photons which are post-selected on successful detection. N_{02} and N_{20} are measured by counting coincidences between two detectors from the same output with quasi-photon number resolving detectors scheme (PNRDS) (see section 3.6.3), whilst N_{11} corresponds to coincidences between two detectors of different outputs of the HOM interferometer. Experimentally, we can extract the probability P_{11} by measuring the coincidence counts:

$$P_{11} = \frac{N_{11}}{N_{11}+N_{02}+N_{20}}. \tag{3.18}$$

where N_{02} and N_{20} are corrected from the intrinsic loss given by the detection technique of the bunching events with PNRDS. Furthermore, an uneven coupling efficiency of each output channel can lead to errors in the estimation of the measured P_{11} and is corrected by normalising the data with the use of Klyshko efficiency (see section 3.3.5) [87].

In this chapter, HOM interferences are realised with a two-colour entangled photon pair source to increase the precision of the measurements. For such an input state, Eq. (3.15) is rewritten to:

$$P_{11} = \begin{cases} 1/2 \times \left[1 - \alpha\left(1 - \left|\frac{t}{\tau}\right|\right) cos(2\pi\Delta\nu t + \phi)\right], & \text{for } |t/\tau| \leq 1 \\ 1/2, & \text{for } |t/\tau| > 1 \end{cases} \tag{3.19}$$

Where $\Delta\nu$ is the frequency separation of the downconverted photons and ϕ the phase between the two sub-states (see section 2.4.2 for more details). P_{11} is estimated from experimental data, then with a fit using Eq. (3.19) of the HOM interference initially measured before depth imaging, the time delay t is found numerically. The fit of the interference is done via a script calculating the $L2$-norm cost function $C_2(\alpha, \Delta\nu, \tau, \phi)$ for each list of parameters $(\alpha, \Delta\nu, \tau, \phi)$. We write:

$$C_2(\alpha, \Delta\nu, \tau, \phi) = \frac{1}{N}\sum_{i=1}^{N}\left(HOM_F^{(i)} - HOM_M^{(i)}\right)^2. \tag{3.20}$$

The unique solution is given by an unique list of parameters minimising Eq. (3.20). $HOM_F^{(i)}$ is the estimated fit of the P_{11} function of the list of parameters and $HOM_M^{(i)}$ is the experimental P_{11} from N measured data points that the script is initially trying to fit. The $L2$-norm cost function calculates an unique solution via Euclidean distance and is more robust compared to the $L1$-norm cost function, justifying why it was been chosen over $L1$. To make the script faster, the parameters can be initially estimated. First, the visibility α can be calculated from the maximum and minimum of N_{11} within the interference. The frequency separation $\Delta\nu$ is calculated from a Fourier transform of the interference. This does not work very well for low frequency ($\leq 0.10\ THz$) where the frequency is too low and not enough periods are within the HOM interference to give a good approximation. The parameter τ is inferred from the temporal width of the photon and is known to be $\tau = 5.5\ ps$. Finally, ϕ can be initially guessed by looking at the number of anti-bunching coincidence counts for $t = 0$. The interference fringe on which the measurements are done is known from the fit and the coarse delay which is chosen before depth imaging. Then, within this half-fringe period, the relative time t can be associated with each measured P_{11}. Finally, using Eq. (3.4) and assuming $\Delta d = 0$, the relative thickness of the sample for a difference in the refractive index $\Delta n = n_2 - n_1$ is given by:

$$\Delta L = c\frac{\Delta t}{\Delta n}. \tag{3.21}$$

3.3.3 Fisher information

As discussed previously, the variation in thickness within the sample ΔL is inferred from the relative time delay Δt after fitting the HOM interference. The Fisher information $\mathscr{F}(t)$ quantifies the information over the parameter t for the observed random variable N_{11} (see section 2.3.2). Furthermore, it has been discussed that $\mathscr{F}(t)$ gives a bound on the variance σ_t^2 and is known as the Cramér-Rao bound (CRB). Thus, $\mathscr{F}(t)$ can be used to quantifies the precision on the HOM microscope, where it is important to maximise it to achieve the best precision for the estimation of the parameter.

Using the definition of $\mathscr{F}(t)$ from Eq. (2.12), we have:

$$\mathscr{F}(t) = \frac{1}{P_{11}}(\partial_t P_{11})^2, \tag{3.22}$$

with P_{11} the probability to detect anti-bunching coincidence event for a given relative time delay t and ∂_t the first derivative over the variable t. However, in this chapter the bunching coincidence counts N_{20} and N_{02} are monitored to normalise the measurements. Hence, the corresponding Fisher information is given by:

$$\mathscr{F}(t) = \sum_i^n \frac{(\partial_t P_i)^2}{P_i} \tag{3.23}$$

with $i = \{11, 02, 20\}$ corresponding to the anti-bunching and bunching events. As mentioned previously, in this chapter we only consider successful event. From the relationship between the bunching and anti-bunching coincidence counts given by Eq. (3.17), we can write:

$$\mathscr{F}(t) = (\partial_t P_{11})^2 \left(\frac{1}{P_{11}} + \frac{1}{1 - P_{11}} \right) \tag{3.24}$$

where $1 - P_{11} = P_{02} + P_{20}$ corresponding to the contribution of the bunching events on the Fisher information. For a degenerate HOM interference, $0 \leq P_{11} \leq 1/2$. Therefore, the contribution of the bunching event on the Fisher information is negligible as $(1 - P_{11}) \rightarrow 1$ when $t \rightarrow 0$, corresponding to the maximum of $\mathscr{F}(t)$ for the anti-bunching event. However, for a two-colour entangled state, the beat note within the interference makes the bunching and anti-bunching events oscillate between 0 and 1 with a phase shift of $\Lambda/2$, where Λ is the period of the beat note. The contribution of the bunching state on $\mathscr{F}(t)$ for the degenerate and non-degenerate with entangled two-colour state for HOM interference can be observed on Fig. 3.6. For both graphs (a) for the two-colour entangled state and (b) for the degenerate state, $\mathscr{F}(t)_{TOT}$ corresponds to the total amount of Fisher information by summing the contribution of the anti-bunching and bunching state (blue), whilst $\mathscr{F}(t)_{bunch}$ is the Fisher information from the bunching state only. For the two-colour entangled state, the temporal width of the photon τ is set to 5.5 ps to correspond to the HOM interference scanned in this chapter with a detuning $\Delta\nu = 5\ THz$. For (b), τ has been chosen to have the same maximum of $\mathscr{F}(t)_{TOT}$ than (a). Note that due to the discontinuity of the HOM interference (V-shape), $\mathscr{F}(t)$ is not defined for $t = 0$ and at the edge of the interference. The visibility for the HOM interferences used to calculate $\mathscr{F}(t)$ is the same for both cases. First, we can observe that the contribution on $\mathscr{F}(t)$ for the bunching state is much higher for the two-colour entangled state than for the degenerate state. As discussed previously, where P_{11} oscillates between 0 and 1 for an entangled two-colour state and with $P_{22} = 1 - P_{11}$, the HOM bunching interference will oscillate too but with a phase shift of π. Because the contribution of the bunching state for HOM interference with an entangled two-colour state are significant on $\mathscr{F}(t)_{TOT}$, in this chapter quasi photon number resolving scheme (PNRDS) is used to measure the bunching terms (see section 3.6.3). Therefore, $\mathscr{F}(t)$ can be maximised and the precision of the estimation can be increased. Secondly, from this figure we observe that to achieve the same amount of $\mathscr{F}(t)_{TOT}$, the temporal width of the two-photon state needs to be way shorter than for the two-colour entangled state. This reduces the width of the HOM interference from 3 mm for the two-colour entangled state to $\sim 60\ \mu m$ for the degenerate state. Hence, decreasing the temporal width to increase $\mathscr{F}(t)$ has the consequence to decrease the dynamical range of the HOM microscope and is discussed further in section 3.7.

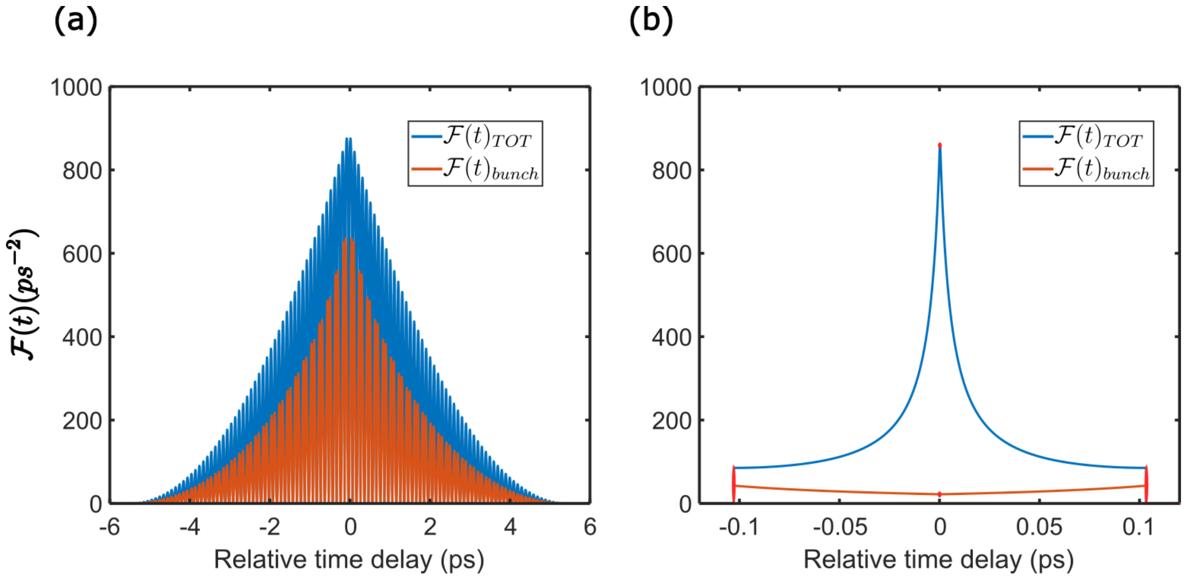

FIGURE 3.6. **Contribution of the bunching state on the Fisher information.** Fisher information per photon $\mathscr{F}(t)$ (blue trace) calculated from Eq. (3.24) for (a) two-colour entangled state (detuning $\Delta\nu = 5\ THz$, visibility $\alpha = 0.95$, temporal width $\tau = 5.5\ ps$) and (b) for a degenerate two photons state (visibility $\alpha = 0.95$, temporal width $\tau = 0.103\ ps$) for HOM interferometry. The contribution on $\mathscr{F}(t)$ for the bunching state is shown by the orange trace. The temporal width τ for the degenerate HOM interference on (b) is set to have the same $\mathscr{F}_{TOT}$ between (a) and (b).

In this chapter, the axial precision of the microscope is characterised with a Fisher information analysis. If the number of photon pairs detected is increased, either due by a brighter source or by reducing the loss within the experiment, the precision of the estimate will improve. Therefore, to compare measurements with different number of photon pairs detected, $\mathscr{F}(t)$ is multiplied by the number of photons detected N to calculate the total amount of Fisher information per measurements. Therefore we define:

$$N \cdot \mathscr{F}(t) = (\partial_t P_{11})^2 \left(\frac{N_{11}}{P_{11}} + \frac{2N_{02} + 2N_{20}}{1 - P_{11}} \right). \tag{3.25}$$

The contribution from the bunching events is limited by its detection scheme used to detect them (see section 3.6.3), where there is an intrinsic loss of 25% in the detection of the bunching events. Improving the method of detection with photon resolution number or by increasing the number of single photon detectors for PNRDS could improve the precision of the measurements. Finally, the Fisher information defined by Eq. (3.25) is used in this chapter to characterise a theoretical limit on the precision from the measurements via the Cramér-Rao bound defined in section 2.3.2.

Finally, Fig. 3.7 shows the maximum $\mathscr{F}$ per photon whilst the frequency separation between the signal and the idler increases. $\mathscr{F}$ has been calculated numerically for the parameter τ and α reported in the experimental section. Increasing the frequency of the beat note improves the precision of the measurements from the CRB (see section 3.3.4) by increasing the Fisher information per photon. The two-colour entangled photon pair source for HOM microscopy can provide tuneability of the precision on the measurements.

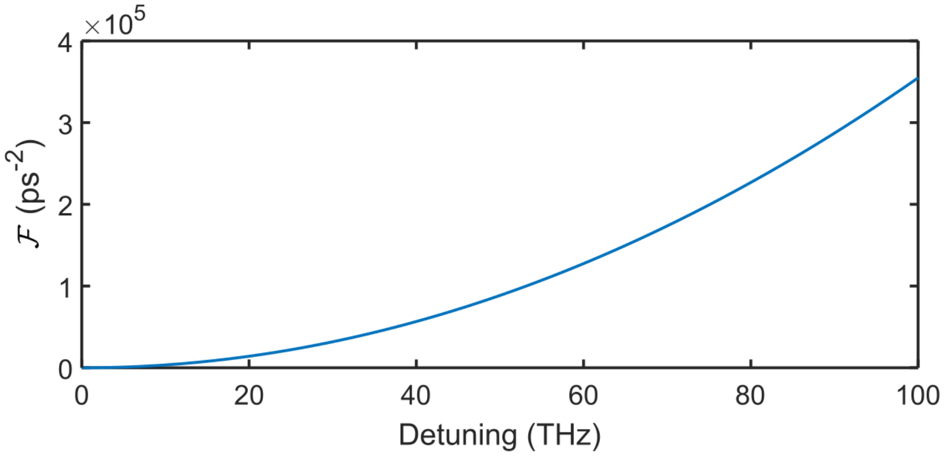

FIGURE 3.7. **Maximum $\mathscr{F}$ per photon function of the detuning.** Maximum of the Fisher information per photon $\mathscr{F}$ calculated from Eq. (3.24) for a two-colour entangled state whilst the frequency separation increases (x axis).

3.3.4 Saturation of the Cramér-Rao bound

An estimator becomes optimal when it saturates the Cramér-Rao bound (CRB) (see section 2.3.2). To saturate the CRB, the following equality must be satisfied:

$$\sigma^2(t) = \frac{1}{N\mathscr{F}(t)}, \tag{3.26}$$

where $\sigma^2(t)$ is the variance of the estimated parameter t and $\mathscr{F}(t)$ its corresponding Fisher information calculated from Eq. (3.23) for N repetitions. The relative time t is inferred from the probability outcomes P_{11} from Eq. (3.15) for a degenerate two-photon state. Hence, we have [91]:

$$\sigma^2(t) = \left(\frac{2\tau}{\alpha}\right)^2 \sigma^2(P_{11}), \tag{3.27}$$

where α is the visibility of the interference and τ the temporal width of the downconverted photons. The variance of P_{11} can be calculated by propagating the error and it gives [91]:

$$\sigma^2(P_{11}) = (\partial_{N_{11}} P_{11})^2 \sigma^2(N_{11}) + (\partial_{N_{22}} P_{11})^2 \sigma^2(N_{22}) \tag{3.28}$$

with ∂_i the partial derivative over the parameter i, N_{11} the monitored anti-bunching coincidence counts and $N_{22} = N_{02} + N_{20}$ the bunching coincidence count. On the other hand by using the definition of the Fisher information from Eq. (3.23) and P_{11} given by Eq. (3.15) we have:

$$\mathscr{F}(t) = \left(\frac{\alpha}{2\tau}\right)^2 \frac{1}{P_{11}(1-P_{11})}, \tag{3.29}$$

with P_{11} experimentally extracted by Eq. (3.18), we have::

$$\mathscr{F}(t) = \left(\frac{\alpha}{2\tau}\right)^2 \frac{N^2}{N_{11}N_{22}}, \tag{3.30}$$

with $N = N_{11}+N_{22}$ the total of photon pairs detected. From the definition of the variance P_{11} given by Eq. (3.28), we assume the random variables N_{11} and N_{22} following a Poissonian distribution. This is due to the low efficiency of the generation of the photon pairs from spontaneous parametric down conversion. Hence we have $\sigma^2(N_{11}) = N_{11}$ and $\sigma^2(N_{22}) = N_{22}$. Therefore, from Eq. (3.28) we can write:

$$\sigma^2(P_{11}) = \frac{1}{N}\frac{N_{22}N_{11}}{N^2}. \tag{3.31}$$

Finally, by combining Eq. (3.27) with Eq. (3.28), we find:

$$\sigma^2(t) = \frac{1}{N} \times \frac{1}{\mathscr{F}(t)}. \tag{3.32}$$

The Eq. (3.26) is saturated, where the variance of the parameter extracted experimentally is equal to the Cramér-Rao bound. Furthermore, the outcome of HOM interference follows a binomial distribution, with the probability P_{11} corresponding to the probability to measure an anti-bunching event N_{11}. The estimator given by Eq. (3.15) is then unbiased, as the estimator of a binomial distribution is unbiased [91]. We can conclude that the estimator used in this chapter for a degenerate HOM interference is optimum over the parameter t. Finally, for a two-colour entangled state, P_{11} is given by Eq. (3.19). Because the Fisher information is maximised for $t \to 0$, therefore we have $cos(2\pi\Delta\nu t) \to 1$ when $t \to 0$. Hence, the calculation for such an input state are similar, consequently the CRB is saturated too for a two-colour entangled photon pairs source for HOM interferometry.

3.3.5 Correction with the use of Klyshko efficiency

Fig. 3.8(a) shows a 1×4 fused fibres coupler (splitter) after each output of the HOM interferometer with single photon avalanche photodiode detectors (APD) at the end of them. Detection of a coincidence event between two detectors of the same output results the detection of a bunching event (N_{20} for the top and N_{02} for the bottom), whilst the detection of a coincidence event between two detectors of two different outputs results in the detection of an anti-bunching event (N_{11}). The detection of the bunching event is possible due to the splitter where a photon has a 25% chance to be transmitted to one of the four channels[2]. We can understand from it that for this detection scheme there is a 25% chance ($4 \times (25\%)^2$) for both of the photons (signal in blue and idler in red) to be transmitted to the same channel and not being resolved by an APD. Hence, before normalisation of N_{11} with Eq. (3.18), the bunching coincidence counts are corrected to this intrinsic loss of the PNRDS used in this chapter.

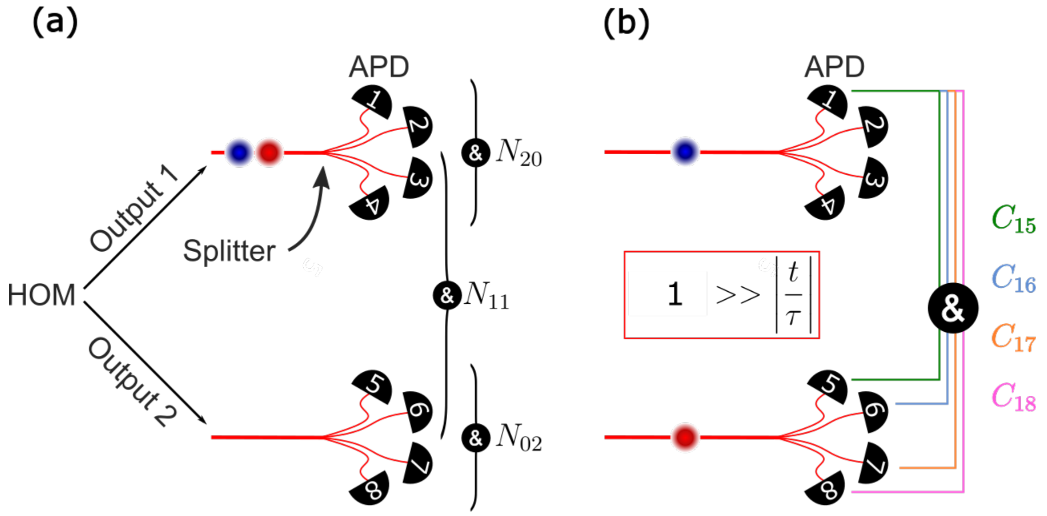

FIGURE 3.8. **Quasi photon number resolving scheme & normalisation through Klyshko coefficient.** (a) Each of the HOM output is followed by a 1×4 fused fibre coupler (splitter) to resolve bunching coincidence counts. Coincidence between detectors of the same output results to a detection of the bunching event whilst detection of coincidence between two detectors of two different outputs result to the detection of a anti-bunching event. (b) Example of an experimental characterisation of the transmission η_1 from the Klyshko coefficients calculated from anti-bunching coincidences on the HOM interferometer for a time delay $|t| >> \tau$. These measurements are repeated for all other channels with their corresponding coincidence events.

Miss-alignment and unbalanced loss between the two outputs of the HOM interferometer might lead to errors within the parameter estimation. Therefore, to estimate the loss in the microscope, the Klyshko efficiency [87] is implemented to calibrate N_{11}, N_{02} and N_{20} by measuring the transmission η for each of the output channels. To characterise the transmission η of each channel, the coarse delay of the HOM interferometer t_{HOM} is set to be large enough where no interference occurs giving $P_{11} = 1/2$. Fig. 3.8(b) shows an example of how η_1 is experimentally

---

[2] also called PNRDS for pseudo (or quasi) photon number resolving detectors scheme

characterised. The signal and idler (respectively represented by a blue and red dots) will be transmitted through one of the channels when the coincidence between the detector 1 and any detector from the output 2 is monitored. We have:

$$C_1 = \eta_1 \sum_j \eta_j \overline{C_{1j}}, \tag{3.33}$$

where $\overline{C_{1j}}$ are the coincidence counts with no loss between the channel 1 and j with $j = 5,\ 6,\ 7,\ 8$ and C_1 all coincidence events measured between the channel 1 and the channel j. Then, for the single counts we can write:

$$S_j = \eta_j \overline{S_j}, \tag{3.34}$$

where again, $\overline{S_j}$ corresponds to the single counts with no loss of the channel j. Assuming that the photons we are detecting are only from the spontaneous parametric down conversion process, then every single counts is associated with another photon, either detected (giving a coincidence) or lost (giving a single count). Then, for any channel j we can write:

$$\overline{S_j} = \overline{C_{1j}}. \tag{3.35}$$

Because the measurements are done at the output of the HOM interferometer with $P_{11} = 1/2$, 1/3 of the single counts will be from the contribution of the anti-bunching coincidence C_1 and 2/3 from the bunching coincidence counts that we are ignoring. Therefore, by combining Eqs. (3.33), (3.34) and (3.35) we finally have:

$$\eta_1 = \frac{1}{4} \sum_{j=5}^{8} \frac{C_{1j}}{2/3 \cdot Sj}. \tag{3.36}$$

We can generalise this to every channels from the output of the interferometer to

$$\eta_i = \frac{1}{4} \sum_{j=5}^{8} \frac{C_{ij}}{2/3 \cdot Sj}, \tag{3.37}$$

with $(i = 1,\ 2,\ 3,\ 4)$ and where C_{ij} are the raw coincidence counts between the detectors i and j. S_j corresponds to the single counts detected by detector j $(j = 5,\ 6,\ 7,\ 8)$. When $t_{HOM} >> |t/\tau|$, we have $P_{11} = 1/2 = 2 \times P_{02} = 2 \times P_{20}$. Hence only 2/3 of the single counts from the detectors j will correspond to the state N_{11} while 1/3 of these single counts belong to the anti-bunching state N_{20}. Likewise, similar expressions can be derived for the other detector channels, where the roles of i and j are reversed. Finally, each coincidence count total C_{ij} can be normalised using the corresponding heralding efficiency coefficients to account for unbalanced losses.

3.4 Degenerate photon pair source

The target state for HOM interferometry with degenerate photon pairs is generated with the source shown in Fig. 3.9, which have been mounted and aligned following the protocol from appendix A.1. A CW pump laser centred around 404 nm with a linewidth $\Delta\lambda_p = 5\ MHz$ (*Topmode*

405, *Toptica*) is coupled to a single-mode fibre to clean the spatial mode with a coupling efficiency of ~ 55% (L-404). Then, a bandpass filter (BP) centred at 405 nm and linewidth of 10 nm removes the undesirable fluorescence photons after the laser is transmitted through the fibre. The laser pumps a 3 cm long type-II periodically poled potassium titanyl phosphate (ppKTP) crystal through the spontaneous parametric down conversion (SPDC) process. Via this process, a pump photon at 404 nm is converted into a correlated pair of photons at 808 nm by fulfilling the conversation of energy (see section 2.4.1). The polarisation of the pump beam is cleaned to a linear polarisation with a quarter (Q) and half (H) waveplates (WP) followed by a Glan-Taylor (GT) prism. Afterwards, a second HWP ensures the pump to be horizontally polarised to fulfil the phase-matching condition of the birefringent crystal. SPDC is a very low efficient process, therefore a 750 nm longpass filter (LP) removes the excess pump from the downconverted photons centred at 808 nm. To produce degenerate photons, the temperature of the crystal is stabilised by an oven and a PID temperature controller (*TC 200*, *Thorlabs*) set at ~ 32 °C. Every now and then, the central wavelength of the pump laser was varying by a few hundred of nanometres between each switch on/off. Thus, the temperature of the oven needed to be reset between each day and was set to optimise the visibility of the HOM interference. Due to the type-II of the crystal, the signal and the idler have their polarisation orthogonal to each other, hence a polarising beamsplitter (PBS) is transmitting the signal to $\mathscr{A}$ and reflecting the idler to $\mathscr{B}$. The downconverted photons are coupled to spatial single-mode fibre (SF) with lenses of focal length $f = 11.0\ mm$, generating the following input state:

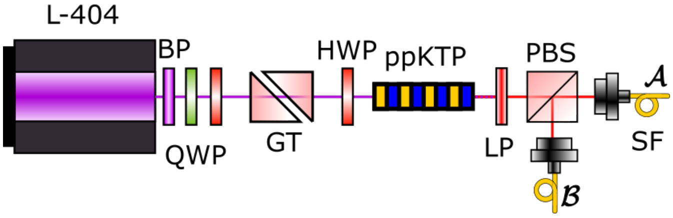

FIGURE 3.9. **Type-II photon pairs source:** CW 404 nm laser (L-404) is pumping the ppKTP crystal. Pump laser is filtered with longpass filter (LP), while the downconverted photons are collected with single-mode fibres (SF). Half (HWP), quarter waveplates (QWP) and Glan-Taylor (GT) are used to control the input polarisation to the crystal. The polarising beamsplitter (PBS) transmit the signal to $\mathscr{A}$ and reflects the idler to $\mathscr{B}$. Bandpass filter (BP) is centred around 404 nm with a linewidth of 10 nm to filter out the fluorescence photons after the laser pump has its spatial mode cleaned by a single-mode fibre.

$$|\Psi\rangle = |\nu_{s,H}\rangle_{\mathscr{A}} |\nu_{i,V}\rangle_{\mathscr{B}}. \tag{3.38}$$

The indices s and i stand for signal and idler with their respective horizontal (H) and vertical (V) polarisation, for two different paths labelled $\mathscr{A}$ and $\mathscr{B}$.

The waist of the pump, signal and idler have been optimised to improve the brightness and the efficiency of the source by using SPDCalc (see appendix A.3) and it has been set to ~ 75 μm.

To ensure to focus the pump at the centre of the crystal and to overlap the collection waist of the signal and idler, the lengths between the fibres and the crystal and the focal length from the lenses have been chosen with the help of the software GaussianBeam (see appendix A.4).

3.4.1 HOM interference with degenerate photon pair source

The state from Eq. (3.38) is used as an input state for the HOM interferometer shown in Fig. 3.1. The single mode fibres from $\mathscr{A}$ and $\mathscr{B}$ are connected to the input ports of the interferometer $\mathscr{C}$ and $\mathscr{D}$. Then, the HOM interferometer is mounted and aligned following the protocol explained in the appendix A.5. The number of anti-bunching coincidence counts N_{11} is monitored for each position of the translation stage on $\mathscr{C}$, whilst it is moving toward the beamsplitter. Due to the length of the crystal and by using Eq. (2.29) we find the spectral bandwidth of the downconverted photon to be $\Delta\lambda = 0.25\ nm$, for $\Delta n = 0.0881$ at the wavelength 808 nm and temperature $32.0°C$ [48]. Therefore the downconverted photons are narrow enough and no bandpass filter is used to filter them.

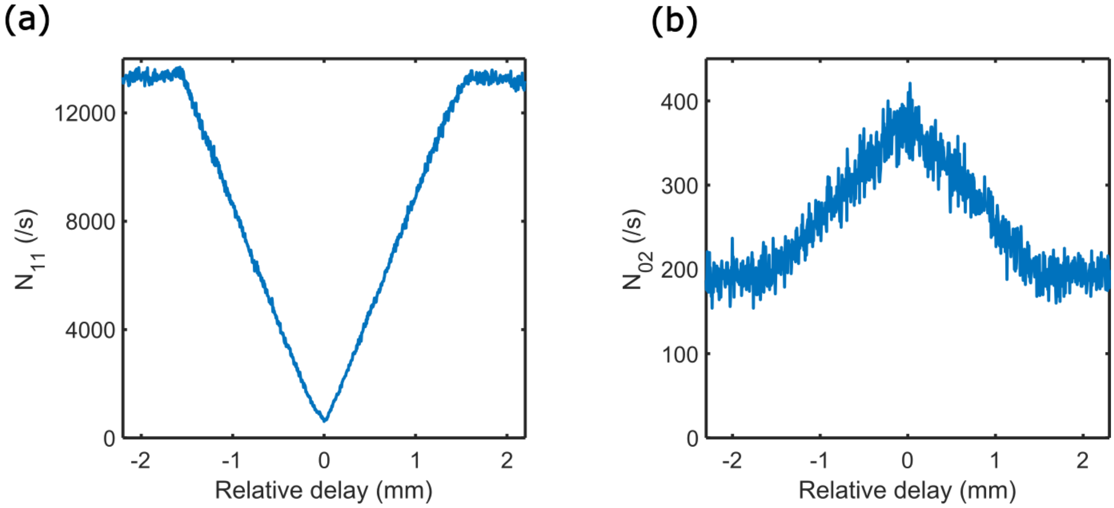

FIGURE 3.10. **Hong-Ou-Mandel interference with type-II degenerate photon pairs source.** (a) HOM interference by measuring the anti-bunching coincidence counts N_{11} while the translation stage is moving forward to the beamsplitter. (b) Bunching coincidence counts N_{02} between two detectors of a single-mode 1×4 fused fibre coupler at one output of the interferometer.

Fig. 3.10 shows two HOM interferences where the anti-bunching coincidence counts (N_{11}) (a) and bunching coincidence counts (N_{02} in (b)) have been monitored for each position of the translation stage. The relative delay d is expressed in mm, where $d = ct$, c is the speed of the light and t the relative time delay between the two photons. The N_{02} are measured by adding a single-mode 1×4 fused fibre coupler at one output of the interferometer and by counting the coincidences between two outputs channel of the coupler with single-photon detectors. The

V-shape of the interference is a characteristic for HOM interference with downconverted photons generated from a type-II crystal, where the phase matching conditions are giving a top-hat shape to the temporal function of the photons [123, 134]. The visibility of the HOM interference in (a) is given by [110]:

$$V_{11} = \frac{C_{+\infty} - C_0}{C_{+\infty}}, \tag{3.39}$$

where $C_{+\infty}$ and C_0 are respectively the number of coincidences for a time delay $t \to +\infty$ (time delay for which there is no destructive interference for the state) and for $t = 0$ (where the number of coincidences is the lowest) and we find $V_{11} = (95.4 \pm 0.2)\%$. For the bunching HOM interference, the visibility is given by:

$$V_2 = 1 - \frac{2C_0 - C_{+\infty}}{2C_0}. \tag{3.40}$$

We find $V_2 = (96.6 \pm 0.6)\%$. The error is higher for the bunching state due to a lower number of photon pairs detected for the bunching state. For the HOM peak illustrated in panel (b), only part of the bunching event was measured. Indeed, the measurements show bunching events between only two detectors from the same output, rather than all different possible combinations of PNRDS using a 1×4 fused coupler single-mode fibre. Hence, because not all N_{02} bunching event has been measured for this interferogram, the number of coincidence counts in this panel is lower than the number of coincidence counts shown in panel (a).

3.4.2 Influence of the waist on the Hong-Ou-Mandel interference

To increase the brightness and the efficiency of the SPDC process, the collection waists of the downconverted photons and the waist of the pump within the non-linear crystal have been chosen following *SPDCalc* (see appendix A.3). As discussed before, due to the length of the crystal the downconverted photons were narrow enough and therefore they were not filtered with bandpass filter. Fig. 3.11(a) shows a Hong-Ou-Mandel interference with a higher anti-bunching coincidence rates compared to Fig. 3.10(a). We can see that the V-shape of the interference is lost and the visibility dropped to $\sim 75\%$. Indeed, by decreasing the size of the waist the local density of energy within the crystal increased and consequently improved the brightness of the photon pairs source. However, the tight focus of the beam within the crystal increased the number of k-vectors and made the overlapping of the pump and downconverted collection waists more challenging at the centre of the crystal by reducing the Rayleigh range.

Fig. 3.11(b) shows three HOM interferences for different configurations of the pump waist ω_P and downconverted photons collection waists ω_C. It seems that increasing the collection waists slightly improve the visibility where the V-shape is apparent for $\omega_C = 100\ \mu m$ and $\omega_P = 75 \mu m$. In the literature, it has been shown that having a wide pumping for a type-II SPDC for HOM microscopy decreased the visibility of the interference with a loss of the symmetry of the interferogram [12, 66, 110]. In the same way that apertures can be used as bandwidth filtering by removing the external k-vector of the light [118], having a tight focus increases the number of

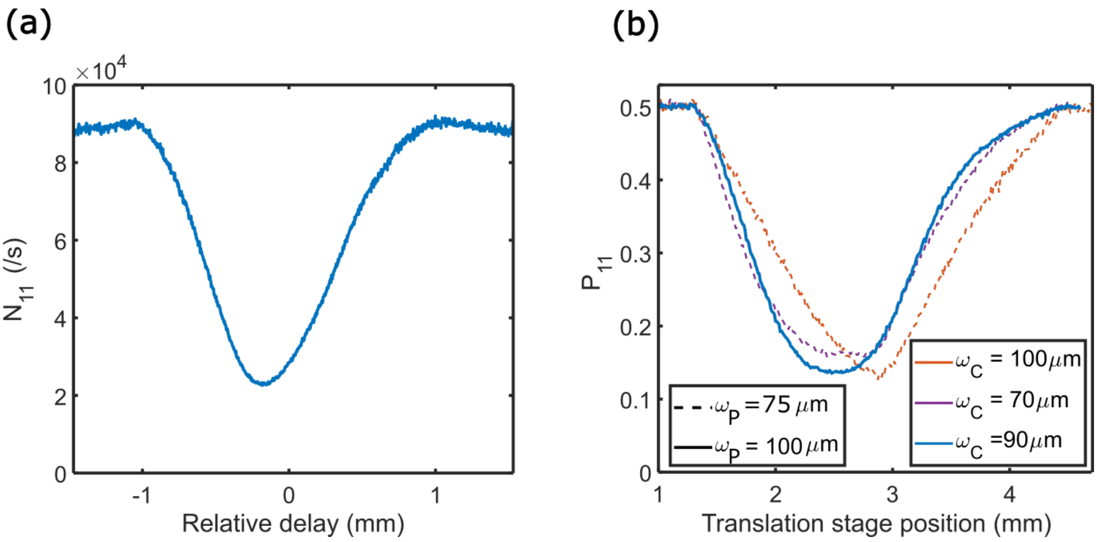

FIGURE 3.11. **Influence of the beam waists for HOM interference.** HOM interferences with different waists of the downconverted photons ω_C and pump waist ω_P. (a) $\omega_C = 60\ \mu m$ and $\omega_P = 65\ \mu m$. A higher number of anti-bunching coincidence counts (N_{11}) is reported than Fig. 3.10 but with a loss of visibility. (b) Normalised anti-bunching coincidence counts (P_{11}) for different pump and downconverted collection waists.

k-vectors and broadens the spectrum of the pump. It induced a smaller Rayleigh range and a miss-overlapping between the collection waist and the pump waist, affecting the spectral bandwidth of the pump. Changing the shape and the visibility of the interference affects the Fisher information per photon. Based on the measurements of Fig. 3.11, to avoid any complications within the experiment for the two-colour entangled photon pairs source, we decided to not go further and to set a pump waist and collection waists of the downconverted photons similar to the orange dashed trace shown on the figure.

3.5 Two-colour entangled photon pair source

The source shown in Fig. 3.12 generates a two-colour entangled photon state with a single type-II ppKTP crystal. It corresponds to a double Sagnac arrangement which has been aligned following the steps enunciated on appendix A.2. First, a diagonally polarised 404 nm CW laser is both transmitted and reflected by a polarising beamsplitter (PBS) propagating toward the non-linear crystal set in an oven. A half-waveplate (HWP) rotates the reflected beam from vertical to horizontal polarisation to fulfil the phase-matching condition. Shortpass dichroic mirrors (DMS) are separating the excess pump from the downconverted photons by transmitting the 404 nm laser and reflecting the downconverted photons towards a second PBS with an efficiency above 98.5%. The type-II of the crystal makes the generation of downconverted photons with an

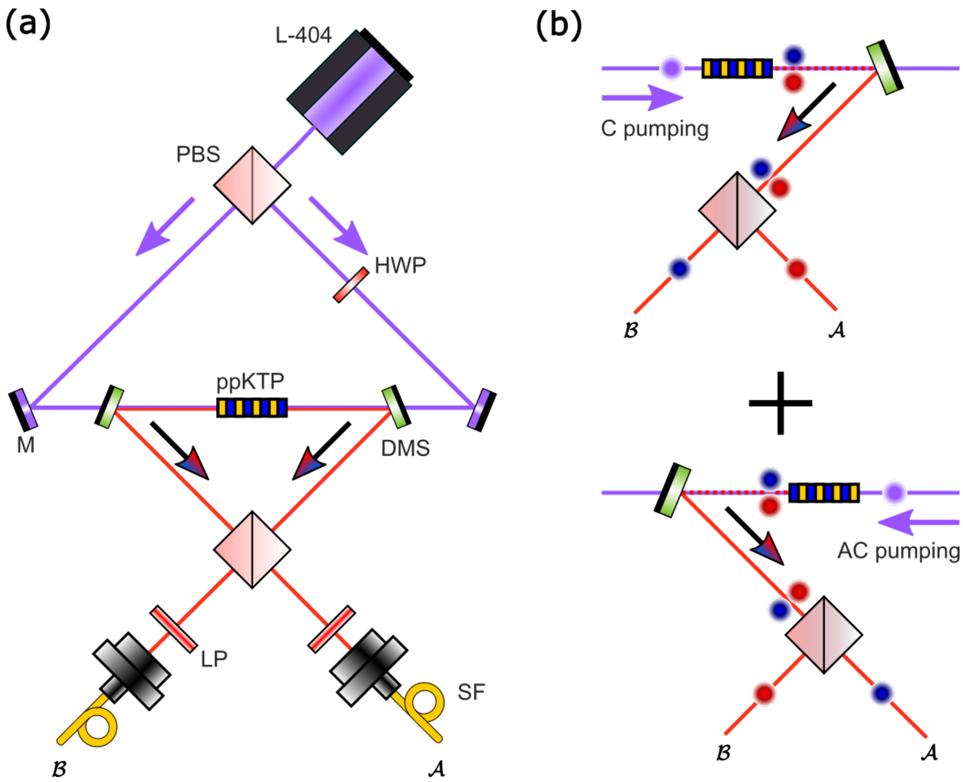

FIGURE 3.12. **Two-colour entangled photon pair source.** (a) Double Sagnac arrangement with a single type-II ppKTP crystal to be pumped in the clockwise (b, top) and anti-clockwise (b, bottom) direction. The CW laser (L-404) with a central wavelength of 404 nm is split by a polarising beamsplitter (PBS). A half-waveplate (HWP) flip the polarisation from vertical to horizontal on the clockwise direction for the phase-matching condition. The dichroic mirrors (DMS) transmit the pump toward the crystal set in an oven whilst the downconverted photons are reflected to a second PBS distributing an entangled two-colour state to the output $\mathscr{A}$ and $\mathscr{B}$, collecting the photons with single-mode fibres (SF) and focal lenses $f = 11.0\ mm$. Longpass filters at 750 nm (LP) removes the excess pump and let pass the downconverted photons. (b) Due to the type of the crystal, the signal (blue dot) and idler (red dot) have respectively a horizontal and vertical polarisation, either sending the signal to $\mathscr{A}$ and idler to $\mathscr{B}$ for a anti-clockwise pumping or the opposite for a clockwise pumping. The crystal is in an oven, controlling the wavelength separation of the downconverted photons by adjusting it. The entanglement relies on the fact that it is impossible to distinguish between the two directions of pumping.

orthogonal polarisation to each other, consequently the PBS is always transmitting the signal and reflecting the idler with an efficiency of ~ 99%[3]. On Fig. 3.12(b) is shown the clockwise pumping (top) where one pump photon (purple) generates a correlated photon pair (blue for signal and red for idler) through the SPDC process. Due to the polarisation of the photons, the signal ends

---

[3] for a wavelength separation $\Delta\lambda = 0\ nm$ and $\lambda = 808\ nm$.

up in the output $\mathscr{B}$ and the idler in the output $\mathscr{A}$. Whilst for the anti-clockwise pumping, the signal and the idler end up, respectively, on the output $\mathscr{A}$ and $\mathscr{B}$ corresponding to the opposite of the clockwise pumping. Because it is impossible to distinguish if the diagonally polarised pump photon will be either transmitted or reflected by the first PBS, the two cases becomes indistinguishable making the source entangled in wavelength. To maximise the fidelity of the entangled state, the second Sagnac interferometer has been aligned with the help of an alignment laser to achieve classical interference with a visibility above 98.5%. Finally, 750 nm longpass filters (LP) remove the remaining pump reflected by the DMS and the downconverted photons are collected to single-mode fibre (SF) with confocal lenses of $f = 11\ mm$.

The photon pair source generates $\sim 200\ k$ coincidences per second for a pump brightness of $\sim 20\ mW$ with a heralding efficiency up to 25% for the following state:

$$|\Psi\rangle = \frac{|\nu_{s,H}\rangle_{\mathscr{A}}|\nu_{i,V}\rangle_{\mathscr{B}} + e^{i\phi(t)}|\nu_{i,V}\rangle_{\mathscr{A}}|\nu_{s,H}\rangle_{\mathscr{B}}}{\sqrt{2}}. \tag{3.41}$$

$\mathscr{A}$ and $\mathscr{B}$ are the outputs showed in Fig. 3.12(a) whilst s and i stand for signal and idler with their respective horizontal (H) and vertical (V) polarisation. $e^{i\phi(t)}$ corresponds to the phase between the two sub-states and is given by the path difference before the downconverted photons interfere at the PBS. By using a double Sagnac arrangement to generate the entangled state from Eq. (3.41), the phase $e^{i\phi(t)}$ becomes unstable. Indeed, the clockwise and anti-clockwise paths from the source do not share common mirrors like we can find for sources using single Sagnac arrangement [85, 135]. Therefore, the mechanical vibrations of the mirrors (that are completely random and uncorrelated between them) are causing instabilities within the phase leading to extra noise within the HOM interference. To correct these instabilities, the source is actively phase-locked as it is discussed in section 3.5.1.

Finally, the wavelength separation of the source is controlled by changing the temperature of the crystal. The PID temperature controller can tune the temperature between 20 $°C$ and 200 $°C$ and applies a mechanical strain to the crystal affecting the density of the medium, consequently modifying the refractive index [158]. This induces a modification in the phase-matching condition by affecting the optical length of the periodical polling Λ discussed in the section 2.4.1. The limitation of this technique is found in the performance of the PBS. When the temperature of the crystal is above $\sim 150\ °C$, the PBS of the downconverted Sagnac does not transmit and reflect only horizontal or vertical polarised photons. Therefore the state sent to the HOM interferometer is not a pure entangled state which can be described by Eq. (3.41) but more by a mixed state. This affects the visibility of the HOM interference and significantly decreases the Fisher information (*i.e.* degrades the precision) of the measurements. For this reason the measurements characterising the performance of the microscope have been made for a temperature of the crystal below 150 $°C$. Using a different technique to tune the separation wavelength of the downconverted photon such as tuning the wavelength of the pump photon could prevent this experimental problem.

3.5.1 Active phase-locking of the two-colour entangled photon pairs source

The photon pair source previously described in Fig. 3.12(a) generates a two-colour entangled state with a double Sagnac arrangement. To fulfil the phase-matching condition, the reflected beam of the pump needs to have a half-waveplate to rotate the polarisation from vertical to horizontal direction. However to generate the two-colour entangled state, we need to be in the situation exposed in Fig. 3.12(b) where between each direction of pumping (clockwise and anti-clockwise), the signal and idler have a different outputs. This cannot be possible with a single Sagnac arrangement where the pump and the downconverted photons share the same path forcing the downconverted photons to be transmitted through the HWP. Consequently the downconverted photons from the different direction of pumping do not share common mirrors and uncorrelated mechanical vibrations cause phase instabilities within the phase $\phi(t)$ from the state in Eq. (3.41).

Fig. 3.13(a) shows a noisy HOM interference with the entangled two-colour photon pair source, whilst Fig. 3.13(b) shows measurements of the normalised anti-bunching coincidence counts P_{11} for a fixed position of the translation stage in the HOM interferometer (red dashed line on (a)). We can see that P_{11} oscillates between a minimum and a maximum despite the time delay being fixed. This does not allow depth microscopy with HOM interference as for a fixed time delay, the probability of anti-bunching are not stable across time.

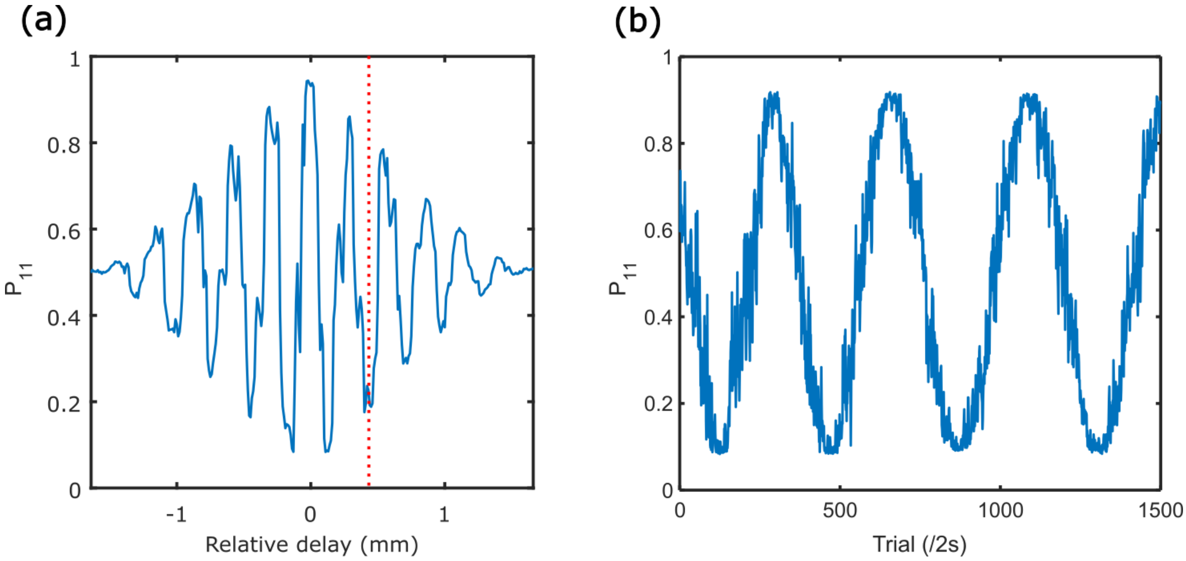

FIGURE 3.13. **Phase instabilities for HOM interference with two-colour entangled state.** (a) HOM interference with the entangled two-colour state. The HOM interference is noisy due to instabilities in the phase $\phi(t)$ from Eq. 3.41. (b) Monitored normalised anti-bunching coincidence counts for a fixed position of the translation stage (red dashed line on (a)).

Therefore, to correct these instabilities within the phase, the photon pair source is actively phase-locked. The principle is simple, perturbations are probed with a back-propagating laser within the source while the PID controller applies a correction in real time. Fig. 3.14(a) shows the phase-locking scheme used to stabilise the source. A longpass dichroic mirror (DML) reflects ~ 10% of a single-mode CW Ti:Sapphire laser (*Solstis*, *MSQUARED*), whilst the downconverted photons from the same path are transmitted with ~ 98% of efficiency to enable phase-locking while the source is running. The wavelength of the laser is set at 730 nm which corresponds to the cut-off wavelength of the dichroic mirrors (DMS) allowing the beam to be partially reflected and transmitted by them. The probe beam is diagonally polarised and is transmitted and reflected by the polarising beamsplitter (PBS). After the PBS, for both polarisation modes the transmitted light from the DMS is blocked by beam dump (BP) whilst the reflected light propagates toward the crystal to be transmitted by the following DMS and reflected by the purple mirrors (standard

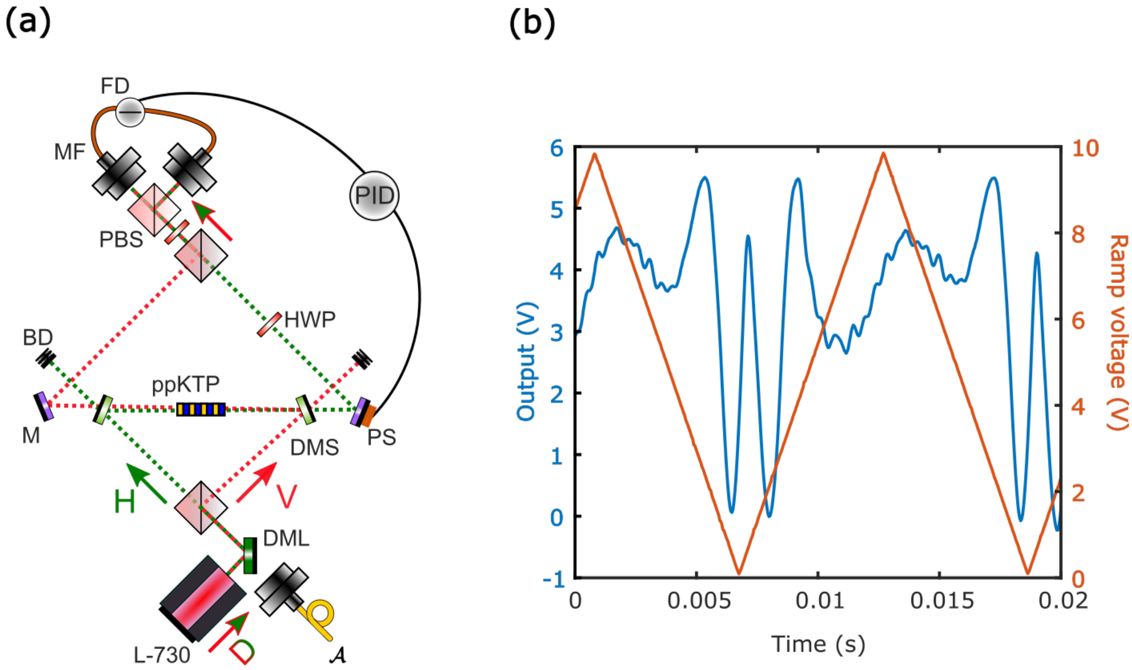

FIGURE 3.14. **Active phase-locking on the two-colour entangled photon pair source.** (a) A diagonally polarised CW laser (L-730) centred at the cut-off wavelength of the shortpass dichroic mirrors (DMS) is back propagating within the source (dashed red line for vertical polarisation and dashed green line for horizontal polarisation), split by the first polarising beamsplitter (PBS) and partially reflected and transmitted by the DMS. A second PBS recombine the beams where a half-waveplate (HWP) and another PBS are projecting the state on the diagonal/anti-diagonal basis. The light is collected by multimode fibres (MF) and measured with fast-balanced amplified photodiode detectors (FD), sending the subtracted electric signal to a PID controller actuating a piezo stack (PS) glued to the mirror (M) of the clockwise pumping path. (b) Measured output from the FD (blue) by applying a 10 Hz ramp voltage to the piezo stack (orange).

mirrors) toward a second PBS. Afterwards, the two polarised light recombine at the second PBS and the measurements are projected onto a diagonal/anti-diagonal basis with a half-waveplate (HWP) and another PBS. The light is collected with multi-mode fibres (MF) to be detected by amplified balanced photodetectors with fast outputs (FD, *PDB450A*, *Thorlabs*). Finally, the subtracted electric signal between the two photodetectors is sent to the PID controller (*LaseLock*, *TEM Messtechnik GmbH*) actuating a 150 V piezo stack with 2.1 μm of maximum travel (PS, *PA4HEW*, *Thorlabs*) glued to one of the mirror of the source. The phase-locking is monitored with an electronic data logger (*Moku:GO*, *Liquid Instruments*) to ensure the stability of the photon pair source during the data acquisition.

The PID controller is correcting the error $e(t) = s - p(t)$ between a desired set point s and the perturbation $p(t)$ by sending an electric signal $u(t)$ to the piezo stacks. The electric signal can be expressed by [78]:

$$u(t) = K_P e(t) + K_I \int_0^t d\tau e(\tau) + K_D \frac{de(t)}{dt}. \tag{3.42}$$

K_P, K_I and K_D are the coefficients denoting the proportional, integral and derivative terms.

Fig. 3.14(b) is showing the subtracted output with the FD while applying a ramp voltage to the piezo stack with the PID controller. The interference fringe can be seen, however the visibility is dropping while the piezo stack reaches half of its full length. The PID controller allows to chose a set point where the visibility of the interference is maximised. With its function of re-locking and its capability to deal with low-frequency which was the order of magnitude of the perturbations on the phase ($\sim kHz$), the PID controller was able to lock the source for few hours enabling enough time to perform depth microscopy presented in the section 3.6.5.

Fig. 3.15(a) shows the same interference from Fig. 3.13(a) after phase-locking the source. The anti-bunching coincidence counts (N_{11}) are normalised by monitoring the bunching coincidence counts with the use of quasi photon number resolving detectors scheme (PNRDS) and is plotted in blue (P_{11}) with the use of Eq. (3.18). We can see that after locking the phase of the source, the noise initially apparent in the HOM interference has been removed[4]. Furthermore, the N_{11} HOM interference in orange shows a slight tilt toward the right side of the figure due to a misalignment whilst the translation stage moves toward the beamsplitter of the interferometer. Normalising the N_{11} with the help of the bunching coincidence counts monitored with PNRDS corrects the tilt reported on the interferogram. Indeed, if the beam is misaligned, the N_{11} detected decrease but with the bunching counts too and therefore P_{11} is not affected by misalignment. It provides measurements despite fluctuations in the brightness of the source.

Finally, despite the source needing active phase-locking, it is important to note that the HOM interferometer demonstrates a higher robustness to phase perturbation within the interferometer compare to a classical interferometer. A 50/50 fibre beamsplitter has been added to the inputs $\mathscr{C}$ and $\mathscr{D}$ of the HOM interferometer to become a Mach-Zehnder interferometer and a CW laser at 808 nm is used as an input beam of the new interferometer. Fig. 3.15(b) shows the output

---

[4] Note that the sampling rate is the same for both figures.

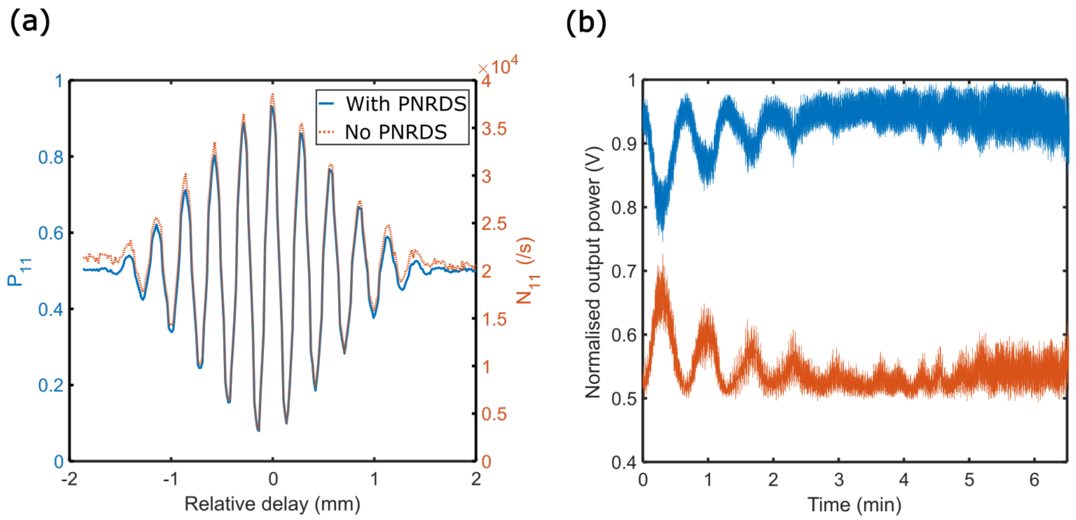

FIGURE 3.15. **HOM interference stabilisation and perturbations on classical interferometry.**(a) HOM interference from Fig. 3.13(a) when the source is phase-locked without normalisation (orange dashed) and with normalisation using quasi photon number resolving detectors scheme (blue trace). (b) A 50/50 fibre splitter has been added to the input of the HOM interferometer. The two outputs (blue and orange trace) are monitored with balanced amplified photodetectors with fast output. The experimental conditions are the same as for the HOM microscope.

light monitored with the amplified balance detectors with fast output used previously for the phase-locking. The experimental conditions are the same than for the HOM interference, the temperature of the lab is controlled and the fibres are taped to the optic table. We can see the output light (blue for one output and orange for the second output) of the new interferometer by using classical light fluctuates due to the instabilities caused by the environmental background. Whilst it has been impossible to scan few interference fringes in these conditions, the HOM interferometer presented in this thesis demonstrates later sub-μm axial precision for depth imaging. We can conclude that the HOM interference is more robust to the environmental background than the classical interference presented here.

3.5.2 HOM interference with the entangled-two colour photon pair source

After generating the two-colour entangled state and actively phase-locking the photon pair source, HOM interferences have been measured across the interferometer. Fig. 3.16(a) shows two HOM interferences between two degenerates photons for the two directions of pumping shown in (b). These two interferograms correspond to HOM interference of the two photons from the same pair. The orange HOM interference have been scanned by monitoring the normalised anti-bunching coincidence counts (P_{11}) and by blocking the clockwise (C) pump photon whilst the anti-clockwise (AC) pump photon have been blocked for the blue trace. The temperature of the crystal is set to

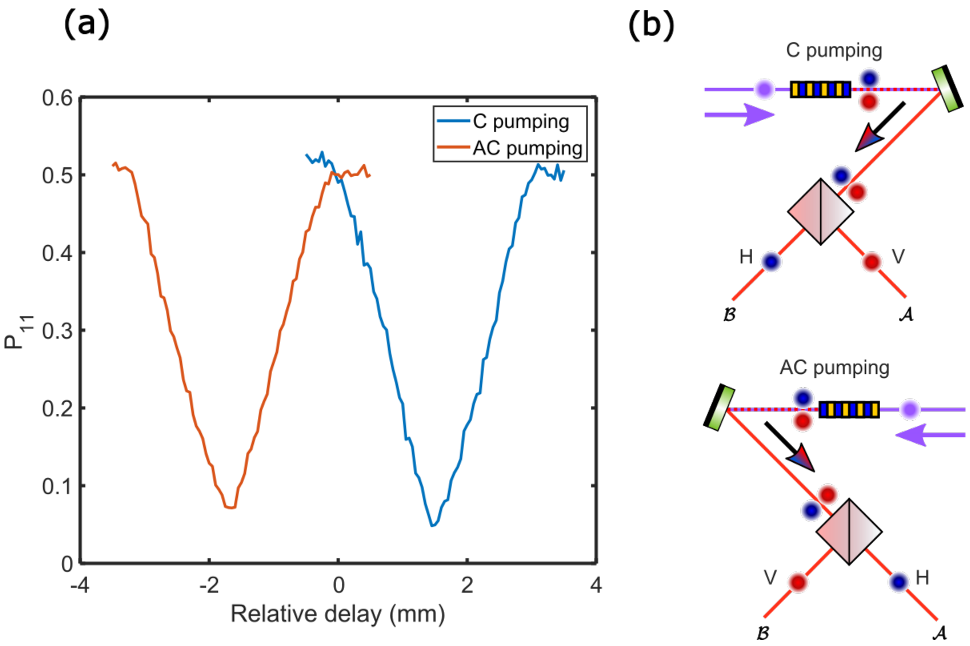

FIGURE 3.16. **HOM interferences for non-entangled source.** HOM interferences with the states from Eq. 3.41. HOM interferences with anti-clockwise pumping (orange) whilst the clockwise pumping is blocked and with clockwise pumping (blue) whilst the anti-clockwise pumping is blocked. The two HOM interferences do not occur for the same position of the translation stage due to the birefringence of the crystal and the orthogonal polarisation of the downconverted photons generated from a type-II crystal.

have degenerate photon pairs, and the waveplates of the HOM interferometer have been set to interfere the photons from the same pair. It is possible to scan these two interferences without blocking any direction of pumping, however because the relative time of arrival is different for the two direction of pumping, it would add noise to both interferences as the two pairs of photons are uncorrelated in time. Hence, the pump have been alternatively blocked to optimise the visibility of the interferences.

The time shift is due to the birefringence of the crystal inducing a different phase velocity regarding the polarisation of the photons. For the blue interference, the translation stage of the HOM interferometer needs to be closer to the beamsplitter than the orange trace. Hence, it means that the photon for which the translation stage changes the time of arrival is a photon with a smaller phase velocity and with a higher refractive index[5]. Rather than for the orange trace, the translation stage needs to be further away from the BS, time delay needs to be added to this photon to see a HOM interference. Therefore in the AC-pumping the translation stage is changing the time of arrival of the faster photon, with the small refractive index.

However, despite the fact that the two pairs of photons are uncorrelated in time, when the

---

[5] the phase velocity is defined as $v_p = c/n$

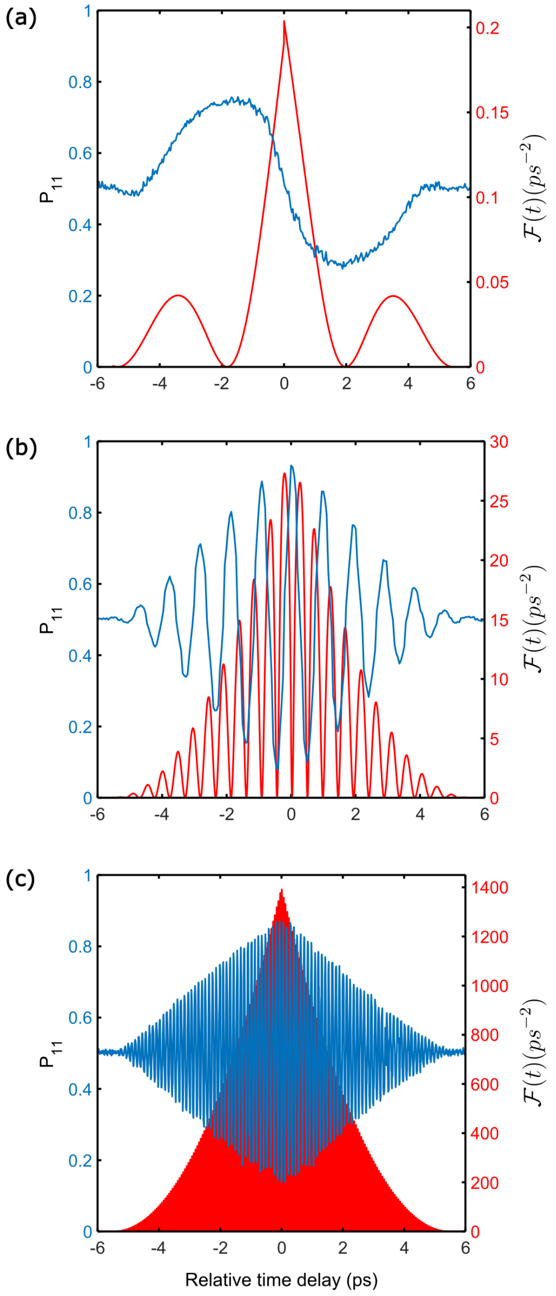

FIGURE 3.17. **Entangled two-colour photon pair source for HOM interference.** Experimental data of the normalised anti-bunching coincidence counts (P_{11}, left axis) using an entangled two-colour photon pair source with a frequency separation of (a) $\Delta\nu = 0.0944\ THz$, (b) $\Delta\nu = 1.05\ THz$ and (c) $\Delta\nu = 8.69\ THz$ with their respective Fisher information $\mathscr{F}(t)$ (red trace, right axis) per photons calculated with Eq. (3.23). Note that the scale for the Fisher information between (a), (b) and (c) is not the same.

waveplates of the HOM interferometer are set to have an interference between the two idlers and the two signals of the two distinct photons pairs, a new HOM interference centred at the relative delay 0 with a beat note appears. Initially, the two photons from each sub-states in Eq. (3.41) have their polarisation orthogonal to each other. Therefore, there is a way to rotate the HWP and QWP before the BS to have an interference between each photon of each sub-state as discussed previously and illustrated in Fig. 3.16. However, when the waveplates are set to induce interference between the two signals of each sub-state, labelled ν_S, and between the two idlers labelled ν_I, the two previous interferences cannot occur. Indeed, the polarisation of the signals and idlers are orthogonal to each other and are no longer indistinguishable. Therefore, the state becomes wavelength-entangled as it is impossible to distinguish between the signals or the idlers of the different direction of pumping. The state cannot be separated into two sub-states as before. Fig. 3.17 shows experimental HOM interferences where the frequency separation $\Delta\nu$ between the signal and the idler has been tuned by changing the temperature of the ppKTP crystal. Their respective Fisher information $\mathscr{F}(t)$ (red trace, right axis) has been calculated using Eq. (3.23) from the fit of the experimental data P_{11} (blue trace, left axis). We can see that for higher $\Delta\nu$, $\mathscr{F}(t)$ increases as it is predicted from the theory. Because the variance of the measurement is $\propto 1/(N\mathscr{F}(t))$, in the following sections the precision of the measurements for depth imaging is controlled by tuning $\mathscr{F}(t)$ through $\Delta\nu$ by tuning the temperature of the crystal.

3.5.3 Wavelength separation of the source

The detuning of the central frequencies of the downconverted photons is readily controlled through phase-matching conditions, which in turn can be tuned by changing the crystal temperature whilst leaving the pump laser frequency unchanged. The crystal is set in an oven where the temperature can be tuned between 20 to 200 $^\circ C$. The change in temperature applies a mechanical strain to the crystal affecting the density of the material [158]. Therefore, the refractive index of the material is changed, inducing a modification in the phase-matching conditions discussed in the section 2.4.1.

Fig. 3.18(a) shows characterisation data for the wavelength of the signal and the idler of the photon pair source (blue for signal and red for idler). The central wavelengths of the signal and idler peaks were measured with a sensitive, high resolution spectrometer (*SR-750-B2-R-SIL*, *Andor*) for a range of crystal temperatures. The pump laser wavelength was measured to be $\lambda_p = 404.093\ nm$ with a linewidth of $\Delta\lambda_p = 5\ MHz$ (*Topmode 405*, *Toptica*). The temperature of the crystal is varying to generate downconverted photons with a wavelength separation $\Delta\lambda$ from $0\ nm$ to $\sim 60\ nm$ ($\sim 30\ THz$). As shown in Fig. 3.18(b), the frequency separation $\Delta\nu$ between the downconverted photons values predicted using the HOM interference beat note (blue) show good agreement with the calibrated detuning curve measured using the spectrometer (red).

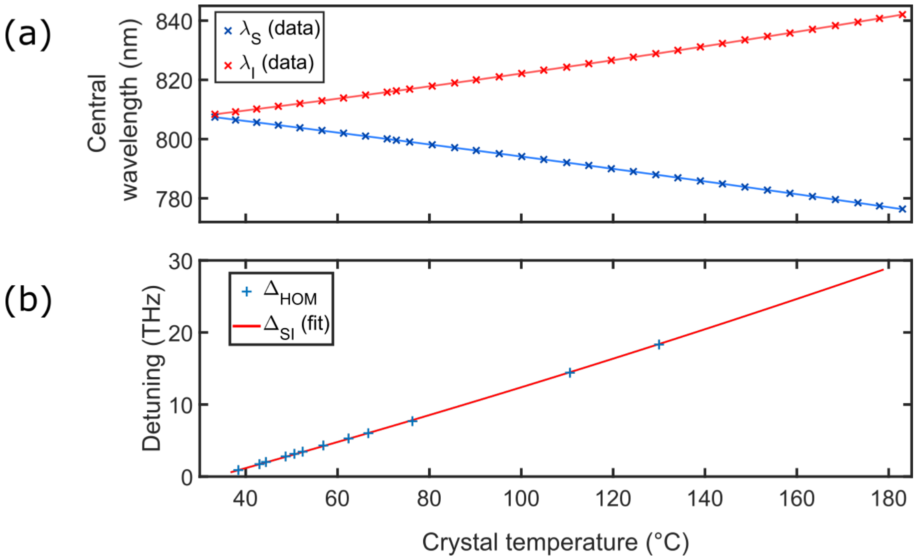

FIGURE 3.18. **Wavelength separation of the photon pair source.** (a) Signal (λ_s) and idler (λ_i) central wavelengths for different temperature of the crystal. (b) Frequency separation (THz) for different temperatures of the crystal with the corresponding frequency of the beat note extracted from the HOM interference (Δ_{HOM}) using the method from section 3.3.2. $\Delta_{SI}(fit)$ corresponds to the fit of the frequency detuning between the central wavelength of the signal and the idler from panel (a).

3.6 The Hong-Ou-Mandel microscope

The HOM microscope used to achieve sub-μm axial precision for depth microscopy is depicted in Fig. 3.19. This microscope has several features allowing depth imaging with HOM interferometry. First, the sample is in between two lenses in a confocal configuration for raster-scan imaging. It decreases the width of the beam to improve the transverse resolution of the image and it is discussed in the section 3.6.1. Then, a spatial single-mode fibre (SF) is placed between the sample and the beamsplitter of the HOM interferometer. It allows to filter the spatial mode of the probe after being transmitted through the sample, removing artefacts within the measurements caused by the roughness of the sample and is discussed in the section 3.6.2. Next feature is the quasi photon number resolving detectors scheme which is implemented with a 1×4 fused fibre couplers (Splitter) to resolve the bunching coincidence counts N_{02} and N_{20} and is defined in the section 3.6.3. Finally, section 3.6.4 introduces the semi-transparent sample used for the microscopy, whilst section 3.6.5 demonstrates depth microscopy with the HOM interferometer. Finally, single-pixel measurements is shown in section 3.6.6 to characterise the performances on the axial precision of the microscopy with the help of the Fisher information.

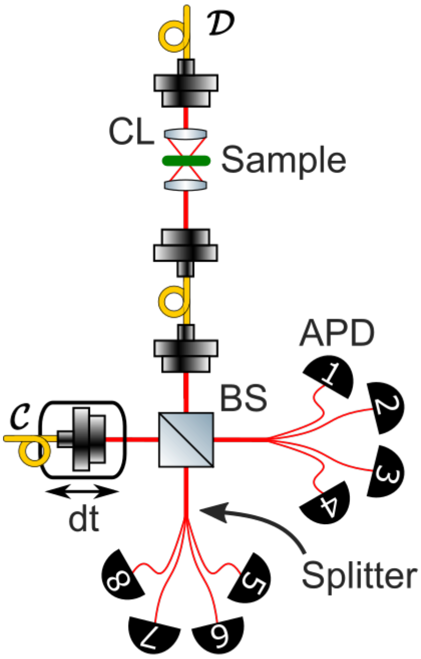

FIGURE 3.19. **The Hong-Ou-Mandel microscope.** The HOM microscope, comprising lenses with focal length $f = 11\ mm$ in a confocal configuration (CL), beamsplitter (BS), 1×4 fused fibre coupler (Splitter), time delay for one input beam controlled by a translation stage (dt) and avalanche photodiode detectors (APD). $\mathscr{C}$ and $\mathscr{D}$ denote the input port of the interferometer. Any coincidences between one detector labelled amongst 1 to 4 with one detector labelled amongst 5 to 8 contribute to N_{11}, while any coincidences between pairs of detectors amongst 1 to 4 correspond to N_{02} and coincidences between pairs of detectors amongst 5 to 8 give N_{20}. This quasi-photon number resolving detection scheme adds an intrinsic loss of 25% for the bunching terms.

3.6.1 Confocal microscopy

The HOM interference is used to estimate the depth of the sample and defines the axial precision. The lateral resolution is given by confocal microscopy where the sample is added between two lenses in a confocal configuration. The imaging is done with single-mode raster scanning technique. This technique of imaging lets the probe beam be spatially filtered out after passing through the sample with a single-mode fibre to avoid path-deviation causing error within the measurements (see section 3.6.2). Two stages (*MTS25/M-Z8*, *Thorlabs*) are translating the sample on a 2D-plane perpendicular to the direction of propagation of the probe photon.

The minimum repeatable increment distance that the stages can achieve is 0.8 μm (given by the supplier). The sample is positioned between two lenses with a focal length of $f = 11.1\ mm$ at 808 nm. The choice of the lenses was based on two criteria and carried out with GaussianBeam

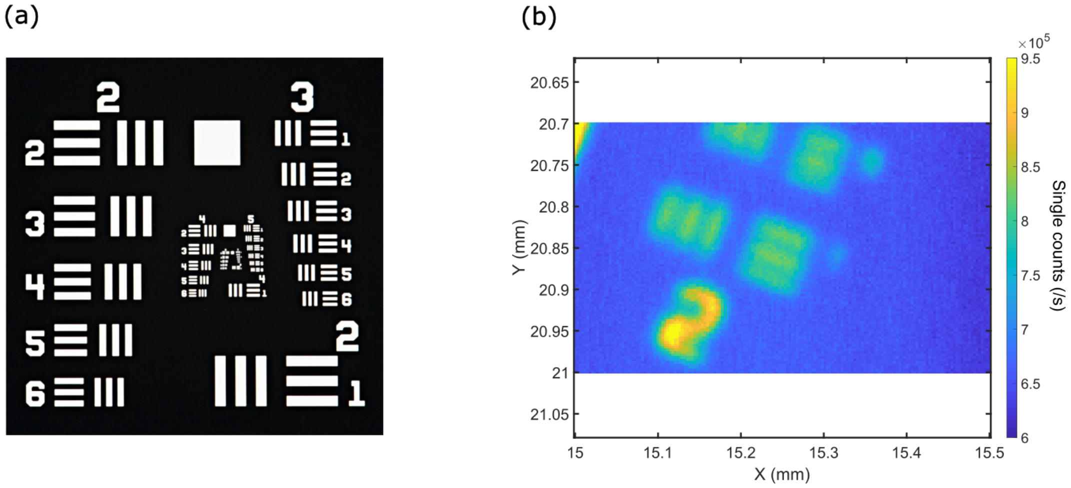

FIGURE 3.20. **Raster-scan image of a resolution target.** Negative resolution target from Thorlabs (a) is raster-scanned while the single counts are measured (right). Group 5 element 1 is resolved with a spacing of 10.4 μm, while the element 2 (line on the top of the right figure) is not resolved (3 lines cannot be distinguished) with a spacing of 9.3 μm between each line.

(see appendix A.4): 1) to decrease the width of the beam to few μm and 2) to allow for enough space for sample placement in between the two lenses. Due to the diffraction limit given by:

$$w_0 = \frac{\lambda}{2NA}, \tag{3.43}$$

where w_0 is the beam waist, NA the numerical aperture of the lenses and λ the wavelength of the beam, the minimum beam waist achievable is $w_{min} = 1.6$ μm (equivalent to a beam width of 3.2 μm).

Fig. 3.20(b) is a raster-scanned image of a negative resolution target (*R3L3S1N*, *Thorlabs*) shown in (a). Because the resolution of the beam profiler was not sufficient, the imaging of the target has been used to characterise experimentally the width of the beam. According to the supplier, the spacing between the first group of the set number 5 (number apparent on the image) is 10.4 μm. The three lines in the horizontal and vertical direction are distinguishable, which is not the case for the group number 2 just above it with a spacing of 9.3 μm. We can conclude that the width of the beam is in between these two values and therefore the waist is half of it leading to $(4.65 < w < 5.2)$ μm. The beam width might have been reduced by improving the alignment of the source, however the confocal lenses were on micro-metric translation stages and the sensitivity was too high to be accurate in the placement of the lenses. Note that it is possible to increase the spatial resolution with confocal microscopy by using better lenses such as microscope objectives or superlensing objective where 100 nm of lateral resolution has been achieved for white light (typically 400 nm to 700 nm) confocal imaging [164]. However the focus of the work for the HOM microscope was on the axial resolution rather than on the lateral resolution and is the reason why no further improvements have been done for the confocal imaging.

3.6.2 Single-mode filtering

The first sample used for HOM microscopy is a fish scale from the species named Astatotilapia calliptera – Eastern Happy[6]. It is a semi-transparent sample once the epithelium is removed and is characterised by uneven depth attributed to the presence of age rings on the surface. The age rings are elevated features in the scale of μm, corresponding to the sensitivity of the microscope. The sample is held in place by two microscope glass cover slips where a small amount of glycerol has been added to avoid the dehydration of the sample. After placing the sample in the confocal microscope, the light collected at the output of the interferometer has been optimised on a single point of the sample. The measurements are made with no spatial filtering with a single-mode fibre and the results are shown in Fig. 3.21. Panel (a) shows HOM interferences by monitoring the anti-bunching coincidence counts N_{11} when the probe photon is transmitted through the glass and the fish scale (blue), only the glass (orange) and no sample (yellow).

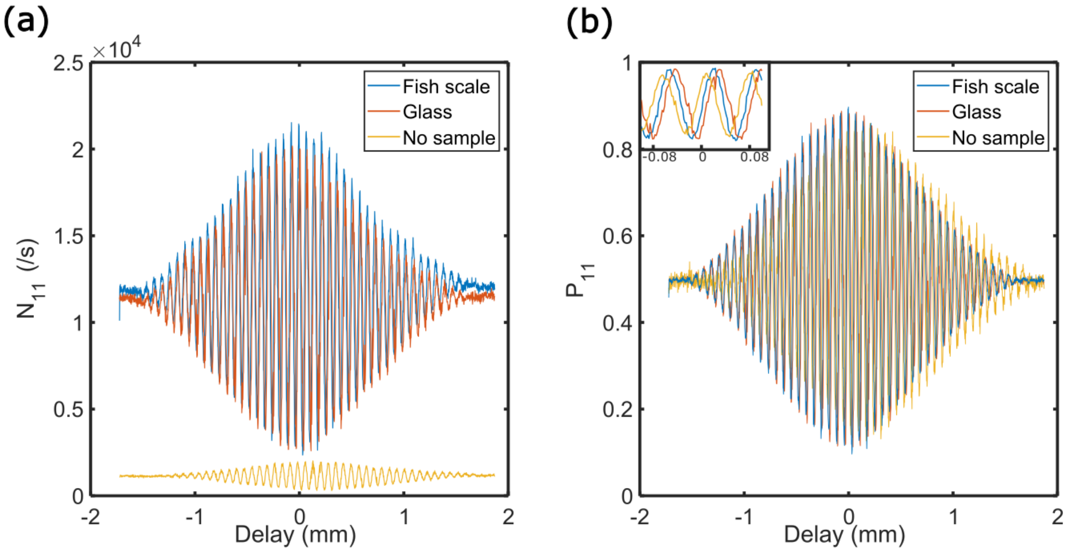

FIGURE 3.21. **HOM interferences through a fish scale without single-mode fibre filtering.** (a) Anti-bunching coincidence counts N_{11} whilst the probe photon is transmitting through the fish scale and the glass holding the sample (blue), only the glass (orange) and no sample (yellow). (b) Normalised anti-bunching coincidence counts P_{11} with the three situations described in (a). Fish: Astatotilapia calliptera – Eastern Happy. The HOM interferences are optimised for a single point of the sample without spatial single-mode filtering.

---

[6] Fish scale given generously by Professor Martin Genner from the University of Bristol, Life science building.

Due to the thickness of the fish scale, a shift of $\Delta d \sim 8\ \mu m$ is apparent between the blue and orange traces. The number of coincidences slightly decreases due to the absorption and misalignment caused by the sample, whilst for the interference with no sample the N_{11} drop significantly. Indeed, the thickness and refractive index of the sample and the glass modify the optical length between the two lenses degrading the performances of the confocal microscope. However, for small thickness features in the range of μm, the performances of the confocal microscope is maintained as the change on the optical length is in the order of the Rayleigh range. By using the normalised anti-bunching coincidence counts P_{11} shown in Fig. 3.21(b), we can see that the visibility for each interference is maintained despite the drop in the N_{11}.

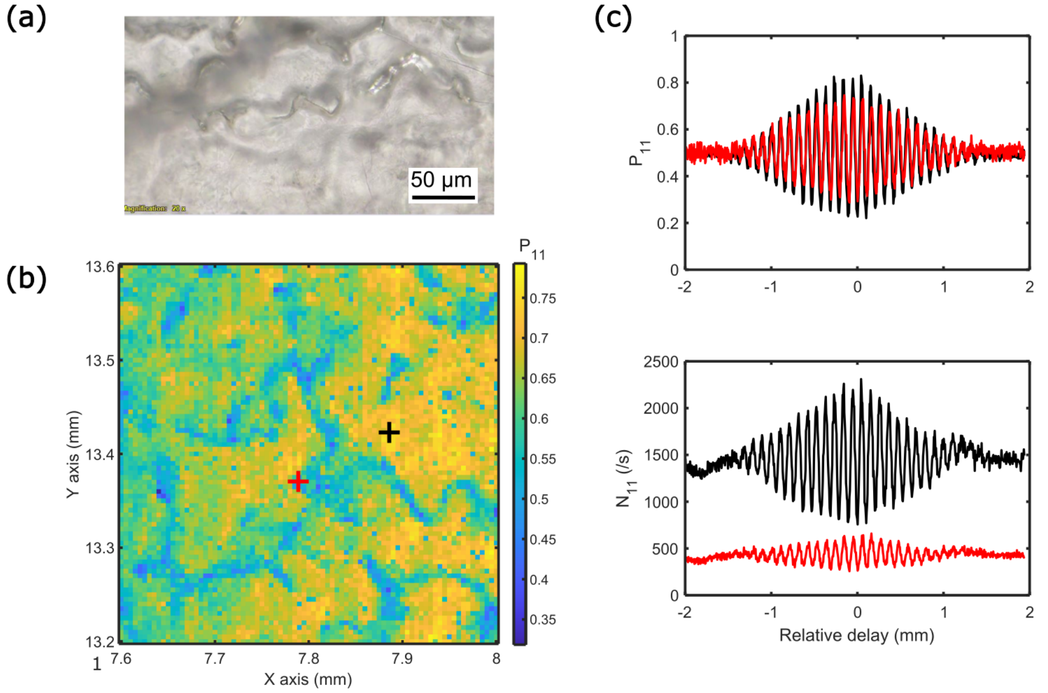

FIGURE 3.22. **Error measurement caused by path deviation for 3D HOM imaging.** (a) Fish scale from a confocal microscope. (b) HOM microscopy on the fish scale by monitoring the anti-bunching coincidence counts P_{11} for every pixels of the sample through raster-scan imaging whilst the coarse delay of the HOM interferometer is fixed. (c) HOM interferences scanned for the two crosses shown in (b). Red and black interference exhibit respectively a visibility of 42.4% and 60.4% with $\Delta\nu = 2.84\ THz$.

With the same experimental setup, HOM microscopy for an area of $0.4 \times 0.4\ mm^2$ is raster-scan by monitoring P_{11} for every pixel with a fixed coarse delay and the results are shown on Fig. 3.22(b). The coarse delay has been set to avoid fringe ambiguity as discussed in the section 3.2. Fig. 3.22(a) shows a picture of the fish scale from a confocal microscope. We can see the age rings in a similar arrangement on the image from the HOM microscope.

The figure at the bottom of panel (c) in Fig. 3.22 illustrates HOM interferences of N_{11} from the two crosses in (b) (red and black). As expected, the features of the sample induce loss in the monitored N_{11}. The figure at the top of the panel (c) shows the same HOM interferences but for the P_{11} instead. The interferences exhibit a visibility of 42.4% for the red trace and 60.4% for the black trace. With no spatial single-mode filtering, we can observe a drop of visibility of the HOM interferences across the sample due to the features causing path-deviation of the probe photon before the beamsplitter. It is a problem for HOM microscopy when the changesin P_{11} are assumed to be only dependent on the relative time delay t due to the thickness of the sample. However here, the sample induces a path-deviation of the probe photon interfering at the BS with the reference photon from the other input. Hence a mismatch in overlap is caused by the depth feature of the sample, directly affecting the visibility of the interference and causing artefact within the measurements. The features remain visible, but their relative thickness cannot be inferred from these measurements.

To correct the mismatch in overlap between the probe and reference photons caused by the roughness of the sample, a spatial single-mode fibre is added between the sample and the BS as shown in Fig. 3.19. Path-deviation from the sample will keep happening, however the

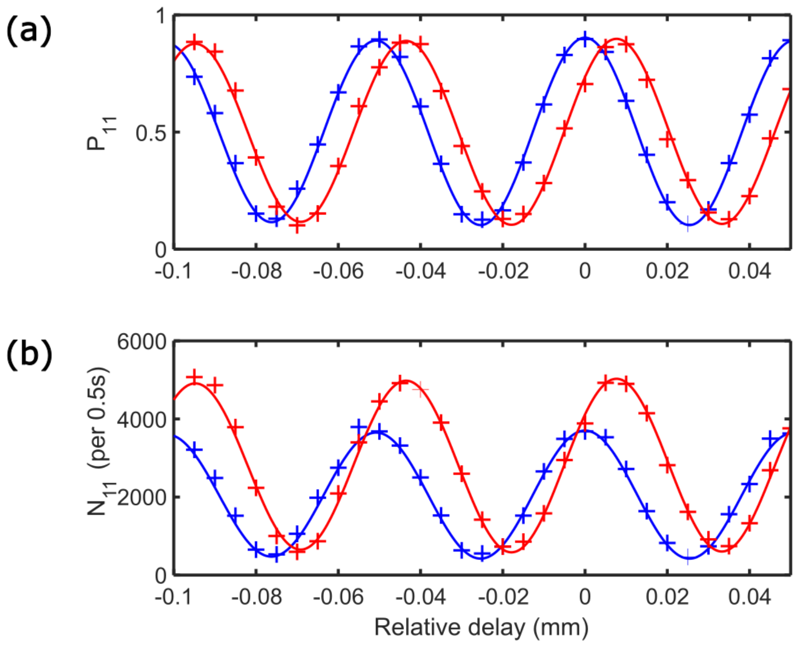

FIGURE 3.23. **HOM interferences between two different thickness after spatial single-mode filtering.** Comparison of the central region of HOM interferences between two pixels with different thickness. In (a) normalised anti-bunching coincidence counts (P_{11}) and (b) without normalisation (N_{11}) for a data acquisition $t = 0.5\ s$. Trace is the fit from the theory and the cross markers are experimental data points.

overlap between the probe and reference photons will be maintained during the scan of the sample and the features of the sample will only cause a drop in the number of photons pairs detected. We noticed from Fig. 3.21 that this drop of N_{11} is not a problem due to the technique of detection which consists to normalise the data by monitoring all events from the output of the interferometer. The single-mode fibre maintains a constant overlap of the two photons at the BS ensuring the same visibility of the interference across the raster-scan imaging and avoids the artefacts reported in the HOM microscopy imaging on the Fig. 3.22(b).

Finally Fig. 3.23 shows two HOM interferences between two pixels of the sample imaged with HOM microscopy shown in the section 3.6.5. The single-mode fibre to filter the spatial mode has been added to ensure the constant overlap at the BS from the two input modes. In (b) we can see a drop of photon pairs detected for the blue trace as discussed previously. However, this time the normalisation of the data brings interferences with the same visibility and is shown in (a). This measurement demonstrates the functioning of the single-mode fibre to avoid the artefact caused by a drop in the visibility of the interference. HOM microscopy can be performed as the variation in the P_{11} is only dependant of the variation in the optical length caused by the sample's thickness.

3.6.3 Quasi photon number resolving detectors scheme

The anti-bunching coincidence counts N_{11} are normalised through Eq. (3.5) by monitoring all events of the HOM interference comprising the bunching coincidence counts N_{20} and N_{02}. Due to the functioning of the detector (see section 2.4.3), multi photon-terms such as the bunching events cannot be resolved. It has been demonstrated by using a multiplexing technique and single photon detectors — also known as quasi photon number resolving detectors scheme (PNRDS) – multi photon terms can be resolved [4, 100].

For this microscope each of the 1×4 fused fibre coupler (splitter) shown in Fig. 3.19 distributes the transmitting photons into 4 output channels. Then the coincidences between detectors from the different splitter correspond to N_{11}, whilst coincidences between two detectors of the same splitter are either N_{02} or N_{20}. Note that PNRDS can be done with only a 1×2 splitter, but fewer bunching events will be detected. Indeed, for a splitter distributing photons across n output channels, there is a probability $p = 1/n$ for the two photons to be transmitted to the same output channel and therefore not being resolved. Hence, by using 1×4 splitter, only 1/4 of the bunching coincidence counts are not resolved and this intrinsic loss to the detection technique is corrected from the normalisation step of the data.

Finally, the table (3.1) shows the transmission of each channel by monitoring singles detections. The splitter has an average of $\sim 25\%$ for the transmission of each output channel. The measurements are done over 1 trial with an acquisition time $t = 1\ s$. The dark counts represent less than 2 % in these measurements.

Detectors	1	2	3	4	5	6	7	8
Raw singles	33 685	32 043	35 387	38 401	34 623	41 326	42 503	41 400
% detections	24.1	23.0	25.4	27.5	21.7	25.8	26.6	25.9

Table 3.1: **Measured singles for each detectors.** Average singles measured in the HOM interferometer over 1 single measurement with an acquisition time of $t = 1\ s$.

3.6.4 Polymer deposition sample

Sub-μm axial precision for depth imaging has been achieved on a sample fabricated by Dr. Jorge Monroy-Ruz, while the design has been made by myself on the software KLayout (see appendix A.6). The semi-transparent sample consists of a 1 mm thick fused silica substrate where a ~ 10 μm thick film of SU-8 polymer was deposited by spin-coating. SU-8 is a negative epoxy photoresist with a high optical transparency making it ideal for this work. Using photolithography, an image of a "KET" was transferred to the polymer by etching the sample, resulting in a semi-transparent sample with two different steps. The difference in thickness is measured to be $(10.62 \pm 0.02)\ \mu m$ between the two steps and it has been characterised with a 3D profilometer where an image of a small part of the sample is shown in Fig. 3.24.

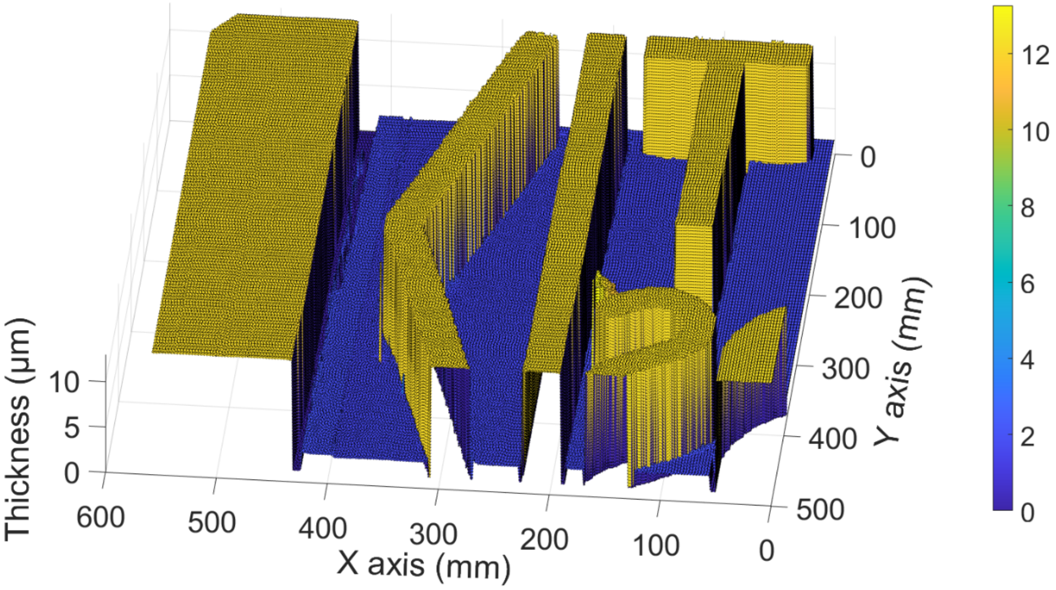

FIGURE 3.24. **Polymer deposition sample.** Image from 3D profilometer (*Profilm3D*®, *Filmetrics*).

3.6.5 Depth imaging with Hong-Ou-Mandel microscope

The transverse resolution of the microscope is limited by the beam waist of the scanning probe and is discussed in the section 3.6.1, whilst the axial resolution, which is the focus of this work, is given by the frequency of the beat note $\Delta\nu$ arising in the HOM interference. Depth imaging with HOM microscopy is performed on the semi-transparent sample described previously and shown in Fig. 3.26(b). As the HOM effect depends on the detection of coincident photons, all results in this section estimating the thickness of the sample consider only photons which are post-selected on successful detection. To maximise the Fisher information for the depth estimate whilst keeping all of the measurements within the same interference fringe half-period (avoiding

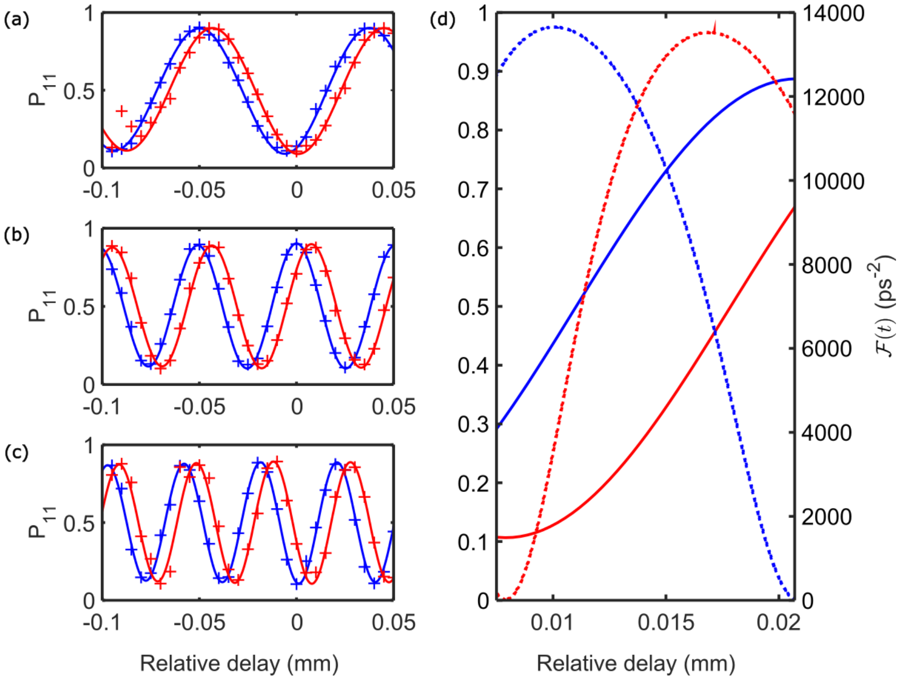

FIGURE 3.25. **Timing offset between interference fringes when comparing measurements at two pixels with different sample thickness.** Comparison of the central regions of the HOM interference fringe patterns when applying different frequencies of the beat note: (a) $\Delta\nu = 3.4\ THz$, (b) $\Delta\nu = 5.9\ THz$, (c) $\Delta\nu = 7.6\ THz$. The blue markers and lines give the results for a selected pixel on the polymer deposition region of the sample, and the red for a pixel in a region with only the substrate and no additional deposited material. Markers correspond to the measured data points, and the lines are a numerical fit to a parameterised model of the interference. (d) Magnified view of a section of (c), with the associated Fisher information per photon shown as dashed lines for both measured positions on the sample. The coarse delay of the reference arm must remain within this range of relative delay to avoid fringe ambiguity. The Fisher information accounts for the intrinsic loss for the bunching terms given by the quasi-photon number resolution scheme used in this experiment.

fringe ambiguity), the signal and the idler photons were detuned by 7.4 THz (16 nm) giving a spatial beat note with a half-period $\Lambda/2 = 20.3\ \mu m$. For comparison to a classical linear optics approach, performing classical interferometry with an equivalent frequency of oscillation would require an electromagnetic radiation source with a central wavelength of $\sim 40\ \mu m$. Operating at such a wavelength would constrain the transverse spatial resolution due to the diffraction limit. On the other hand, classical interference measurements operating at a similar wavelength to the downconverted photons ($\sim 800\ nm$) will suffer from phase instability from the environmental background due to their high sensitivity as shown in Fig. 3.15.

For initial calibration of the HOM microscopy system, the HOM interference features were measured for two pixels positions on the sample (with and without deposited polymer) by translating the coarse delay in the reference arm (Fig. 3.25).

Both measurements showed interference fringes with a visibility of $\sim 80\%$. The sample induces a relative time delay between the reference and the probe photons, leading to an offset of $\sim 8\ \mu m$ between the two interferograms. Assuming a sample refractive index of $n = 1.58$ for the deposited structure, this corresponds to a measured thickness change of 14 μm. For acquiring a full sample image this approach would be prohibitively slow, due to the requirement of repeating the scan of a HOM interference fringe for every pixel. Instead, the coarse delay is set at a fixed position within the range of 0.01 to 0.02 mm (see Fig. 3.25(d)) to avoid fringe ambiguity and the normalised anti-bunching coincidence counts P_{11} are monitored for each pixel. The beat note is chosen to optimise the width of the Fisher information peak such that fringe ambiguity is avoided. Subsequently, the coarse delay is set at the crossing point for the Fisher information curves for the maximum and the minimum required depth measurement values. This provides a compromise by optimising Fisher information and precision at both extremes of the measurement range. Finally, the relative time delay induced by the variation of the thickness within the sample is estimated through the variation in the normalised anti-bunching coincidence counts P_{11}.

The phase-locking was monitored with an electronic data logger (*Liquid Instruments*, *Moku:GO*) to ensure stability of the photon pair source during the data acquisition. If failure in the phase-locking is detected, the system automatically suspends data acquisition and reacquires locking with a new set point for the PID controller. As this results in an unknown offset in the absolute value of the measured sample thickness, it is also necessary in this case to repeat the measurement of the previously acquired pixels. On Fig. 3.26(a) 27×78 pixel positions were measured by monitoring the outcomes P_{11} of the HOM interferometer, with data acquisition time $\sim 20\ min$ ($\sim 40\ min$ total measurement time due to the limited speed of the translation stages) for an area of 0.4 mm^2. The maximum transverse resolution of the HOM microscope was determined to be $\sim 10 \times 10\ \mu m^2$ with a resolution test target (see section 3.6.1), but due to the size of this sample, a reduced transverse resolution ($\sim 15 \times 15\ \mu m^2$) was used to decrease the total acquisition time. Fig. 3.26(c) shows a comparison of a 1D raster scan across a single row of pixels using the HOM microscope with the results from a commercial 3D profilometer (*Profilm3D*®, *Filmetrics*).

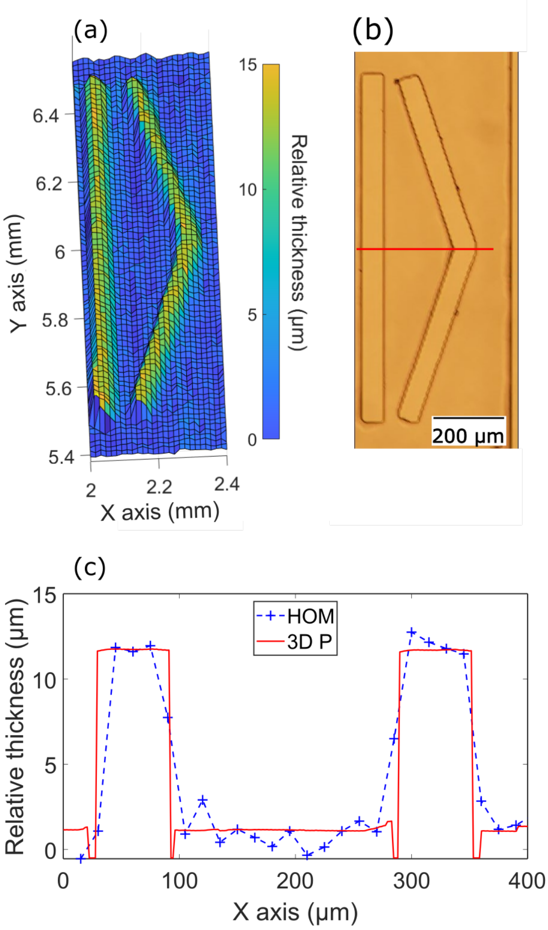

FIGURE 3.26. **Depth sample imaging with HOM microscopy.** (a) Depth HOM imaging by monitoring the number of coincidences for each pixel. Raster scanning of the sample through the single-mode illumination provides the spatial resolution in the 2D transverse plane. The acquisition time is 0.5 s for each pixel ($N \sim 4000$). The frequency beat note is 7.4 THz, where the detuning is chosen such that the characteristic depth features of this sample correspond to measurements across the full range of half of a fringe period from the HOM interference. This attains the maximum Fisher information while avoiding fringe ambiguity. (b) 2D conventional optical microscope image of the sample with a depth profile of (10.62 ± 0.02) μm. (c) 1D scan of depth profile following the path indicated by the red line on (b). Results are shown for HOM microscopy (blue) and for a 3D profilometer (red).

As the raster-scan pattern consisted of a vertical sweep in the Y axis followed by stepwise increment on the X axis, the 1D scan results correspond to data points monitored over a period of ~ 40 min. The results from the HOM microscope agree with the measurements from the 3D profiler (within the given error of 1.1 μm of the HOM microscope system) across the whole time period of the measurement. The sharpness of the edge features observed in the sample profile were limited for the HOM microscope measurement by the reduced transverse resolution. Assuming the known refractive index value for this polymer to be $n = 1.58$ for both the signal and idler wavelengths, the measured relative thickness between the two steps in this sample is determined to be $11 \pm 1\ \mu m$.

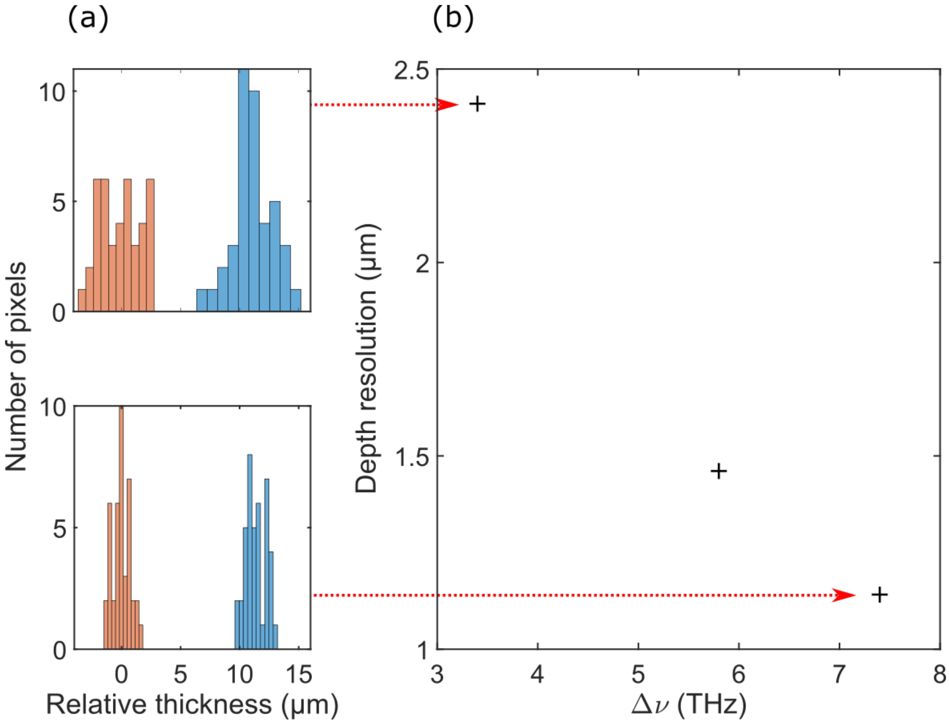

FIGURE 3.27. **Axial precision for varying beat note frequency.** (a) Histograms of the axial depth estimate for the two step measurement for beat note frequencies of 3.4 (top) and 7.4 THz (bottom). (b) Precision of depth estimation calculated from the raw histogram data using Eq. (3.44) after correction for the refractive index of the sample.

Fig. 3.27 shows the results of repeated measurements of the sample for different beat note frequencies, which was used to characterise the axial precision. For each detuning $\Delta\nu$, images similar to Fig 3.26(a) were performed and depth estimates were made by acquiring and combining data from groups of the same 40 pixels (a subset of a pixel column in the image). This was performed on two distinct regions of the sample - with one corresponding to pixels lying on the deposited polymer, which we denote as step 1 (S_1), and the other on a region where no polymer was deposited, which is denoted as step 2 (S_2). As the depth estimates for the two regions are statistically independent, the overall precision combining the two data sets is given by

$$\sigma_t = \sqrt{var(S_1) + var(S_2)}. \tag{3.44}$$

Fig 3.27(a) shows examples of the underlying histogram results of the measured depth for two of the data points in Fig 3.27(b). The effect of increasing $\Delta\nu$ is evident from the reduced variance of the data set of S_1 and S_2 arising from the increase in the Fisher information. Consequently the precision of the measurements is improved and smaller depth features can be more easily distinguished. The best precision result of 0.8 μm for the relative sample thickness of each of the two steps individually, leads to a combined precision of 1.14 μm for the estimate of the relative depth offset between the two steps by using Eq. (3.44).

3.6.6 Single-pixel estimation: precision analysis

In order to decouple thickness variation in the sample from the performance of the microscope, repeated measurements were performed on a single pixel. The normalised anti-bunching coincidence counts P_{11} were measured 500 times for different frequencies of the beat note (from 0.09 THz to 18 THz). For each of the data points, the 500 measurements are split into 10 blocks of 50 measurements. The standard deviation of these 10 blocks is calculated, giving a new data set. The mean of each grouped data set gives the precision value of the corresponding data point shown in Fig. 3.28 and the error bars are given by the standard deviation of the grouped data sets.

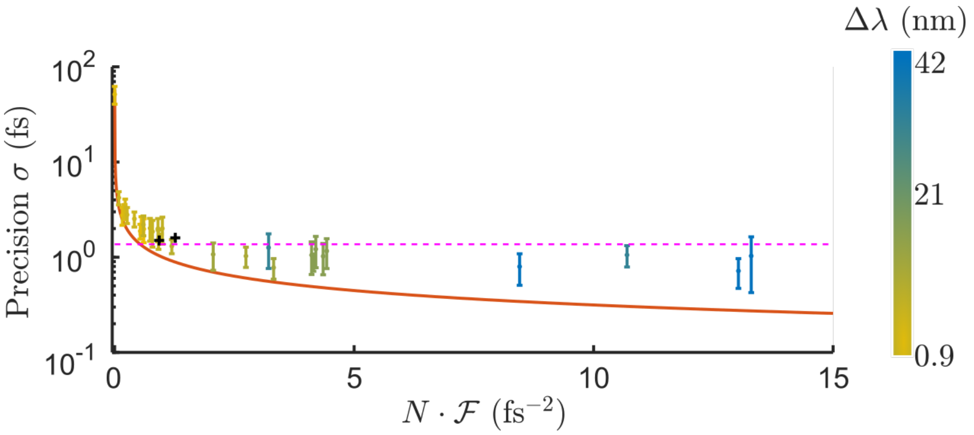

FIGURE 3.28. **Dependence of measured axial precision on total of Fisher information for single pixel estimation**. Total Fisher information is given by the product of the number of detected photon pairs N and the theoretical Fisher information per photon $\mathcal{F}(t)$ (Eq. (3.23)). $\mathcal{F}(t)$ is controlled by varying the wavelength separation $\Delta\lambda$ of the downconverted photons (colour bar on right side). The acquisition time is fixed to 0.5 s and the number of detected photon pairs to $N \sim 10^4$ for every data point. Each point on the graph corresponds to 500 independent time delay measurements split into blocks of 50, where the mean of the standard deviation of these blocks corresponds to the precision. The standard deviation from these 10 blocks gives the error bars. The orange line corresponds to the theoretical bound of the precision for N photons saturating the Cramér-Rao bound (CRB), and the two black crosses correspond to the two step measurement from Fig. 3.26(a). The horizontal dashed line is the threshold for achieving sub-μm axial depth precision ($\sigma \leq 1.4\ fs$), given by Eq. (3.44) for a sample with a refractive index $n = 1.58$.

All data acquisition are done with $N = 10^4$ photon pairs detected where the Fisher information $\mathscr{F}(t)$ is controlled only via the detuning of the downconverted photons. The total amount of Fisher information $N \cdot \mathscr{F}(t)$ is calculated by multiplying the Fisher information per photons with the number of photons detected for each event.

Using Eq. (3.44), it can be shown that sub-μm precision can be achieved for a measurement with total Fisher information $(N \cdot \mathscr{F})$ above 0.5 fs^{-2} and is represented by the pink dashed line for a refractive index $n = 1.58$. We see that it has been achieved for a wavelength separation of 12.3 nm and 10^4 photons pairs detected. Furthermore, the black crosses show the theoretical Fisher information and the precision achieved for each of the step measurements from Fig. 3.26(a) and are in agreement with the single-pixel measurements reported in this figure. Therefore, sub-μm precision for depth imaging would be expected for a source with the same detuning and twice the brightness in the photon pairs detected. The loss in the experiment were mainly caused by the fibre connector FC to FC including 6 dB loss between the source and the output.

The standard deviation on the measurements seems to be sufficiently large. Indeed, we can observe the median of the relative error $\Delta\sigma/\sigma$ from the data set reported to be 26 % and seems to increase for the measurements with higher $N \cdot \mathscr{F}(t)$. As discussed in the section 3.6, the variation in the time delay measurements for HOM interferometry can be caused by a change in the thickness variation of the sample or from a relative change in the optical length Δd between the two inputs. Assuming the instability is primarily due to the changes in the path-length between the two optical fibres before the interference occurs caused by temperature drift. The path difference between the fibres of the two inputs of the HOM interferometer is about 2 cm. The lab is in a controlled environment where the temperature is stable on the order of the $^\circ C$. Therefore, the drift in the measurements from the temperature would be around 10^{-2} fs which is one order of magnitude below the reported precision of the measurements and does not explain the wide spreading of the precision. On the other hand, the Fisher information was tuned by only increasing the wavelength separation between the downconverted photons whilst the number of photon pairs detected N was fixed around $\sim 10^4$ per measurements. As discussed in the section 3.3, the precision of the estimate improves for a higher detuning. The wavelength separation is tuned by controlling the temperature of the crystal. Therefore, we can imagine that for high temperature (> 100 $^\circ C$ for $\Delta\nu \sim 10$ THz), the change in the refractive index affects the laser back-propagating within the source used for the active phase-locking. The most likely cause is that the change of refractive index within the crystal was causing a path-deviation of the laser back-propagating within the source and might have decreased the visibility of the interference shown in Fig. 3.14(b). The phase-locking relies on the interference fringe by actively moving a piezo stack to set the output brightness from the interferometer on a set point.

The oven could also be the cause of these instabilities. The oven of the crystal could be less stable for higher temperature, which can lead to more instabilities within the phase-locking as the reference beam transmits through it. An already phase-locked source such as an integrated photonic chip [138] or bulk-optics source with two crystals in a cross-crystal configuration where both of the downconverted photons share common paths and mirrors [35] could be used to confirm or to refute the hypothesis.

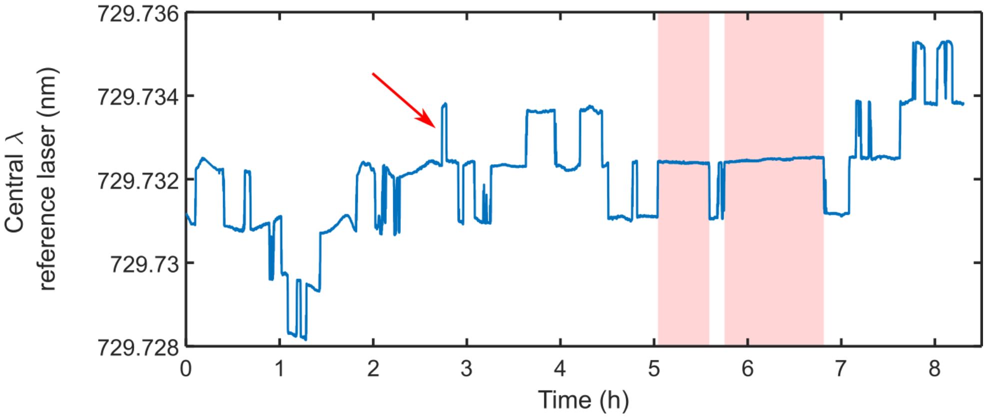

FIGURE 3.29. **Instability in the reference laser to phase-lock the source.** Central wavelength of the reference laser measured with a wavemeter with a wavelength resolution of 200 MHz (*WS6-200*, *HighFinesse*). The mode hoping (red arrow) due to the instabilities in the cavity of the laser makes it unstable to use it for as a reference laser for phase-locking. The pink zone correspond where the laser is stable for a period of time $t \geq 40\ min$.

Finally, in the lab the measurements were stable over a time period of ∼ 40 min and drift in the phase occurred over longer periods of time, which resulted from mode-hopping instability of the laser used to phase-lock the source. Changes in the output wavelength of the reference laser lead to fluctuations in the phase-locking conditions in the interferometer and drifts in the depth estimation. At the end of the experiment, this mode-hopping occurred more frequently and the phase-locking became more unstable and harder to lock. Fig. 3.29 shows the measurements for a period of time of 8 h from a wavemeter (*WS6-200*, *HighFinesse*) of the reference laser used to phase-lock the source. The cavity of the reference laser is phase-locked with a PID controller and a piezo mirror. Usually, when the PID controller diverges from the set point, it tries to re-lock the cavity on another set point, inducing a mode-hoping within the cavity of the laser (*e.g.* see red arrow). This mode hopping changes suddenly the phase of the laser, consequently degrading locking on the photon pair source and it results to a sudden change in the monitored P_{11} from the output of the HOM interferometer. The pink areas from the figure correspond to a period of time longer than 40 min[7] and for which no-mode hopping have been recorded. This correspond to 20 % of the time for which the phase-locking has not been degraded from the instabilities of the laser. Therefore to conduct HOM microscopy with a two-colour entangled state, a more robust

---

[7] Data measurements for HOM microscopy of Fig. 3.26 took ∼ 40 min.

source to phase instability might provide an improvement in the saturation of the CRB for higher frequency of the beat note, such as the source from [35], where the downconverted photons share common mirror and are not affected by the mechanical fluctuations of the optics.

3.7 Future work

The HOM microscope presented in this chapter achieved sub-μm axial precision for depth imaging. By controlling the wavelength separation between the signal and the idler on a wavelength-entangled photon pairs, the sensitivity and the precision of the measurements increased. However, due to fringe ambiguity, the detuning for depth imaging was limited to $\sim 7\ THz$ for a single-shot measurement.

One way to avoid fringe ambiguity is to take more measurements with different beat notes of the HOM interference. For the source used in this thesis, it would require to take imaging for each of the beat note. The time of the imaging can be reduced to target some areas of the sample where an increase of the precision would be required. However this is a time consuming technique as single pass measurement for each pixel would be no longer enough. Furthermore, with consideration of the degradation of the phase-locking in the two-colour entangled photon pairs source due to the perturbations within the reference laser, this strategy of measurement will be harder to experimentally achieve (see section 3.6.6).

The second way to avoid fringe ambiguity is discussed in this section, where the idea relies on generating HOM interferences with different beat note simultaneously. For the photons pair source described in this chapter, this could be done by pumping the ppKTP crystal with different wavelengths and using grating[8] at the output of the HOM interferometer to post-select the right wavelengths and operate coincidence counting for the post-selected wavelength. However, this would need a big amount of detectors, especially if PNRDS would be implemented and therefore not a practicable imaging technique. Instead of using grating, one could use a wavelength division multiplexers (WDM), a technology widely developed in the C-band due to photonic communication which transmits the photon into different channels depending on its wavelength. This has been used on a photonic chip where the photon pairs exhibit a broader spectrum due to the four-wave mixing and the phase-matching condition [138]. In this scientific publication, the HOM interference is given by:

$$P_{11} = \frac{1}{2} - \frac{V}{2}\cos\left(2\pi t\frac{\delta}{\lambda_p^2}\right)\operatorname{sinc}\left(2\pi t\frac{w}{\lambda_p^2}\right), \tag{3.45}$$

where V is the visibility of the interference, t the relative time delay between the two input modes of the HOM interferometer, δ the wavelength separation between the signal and idler, w the width of the WDM channel and λ_p the wavelength of the pump.

Fig. 3.30(a) shows HOM interferences with different detuning reported in [138], where their corresponding Fisher information is shown on Fig. 3.30(b). We can see that $\mathscr{F}(t)$ with a wavelength

---

[8] Apertures can be used to filter k-vectors (then the wavelength) for non-collinear crystal [118]

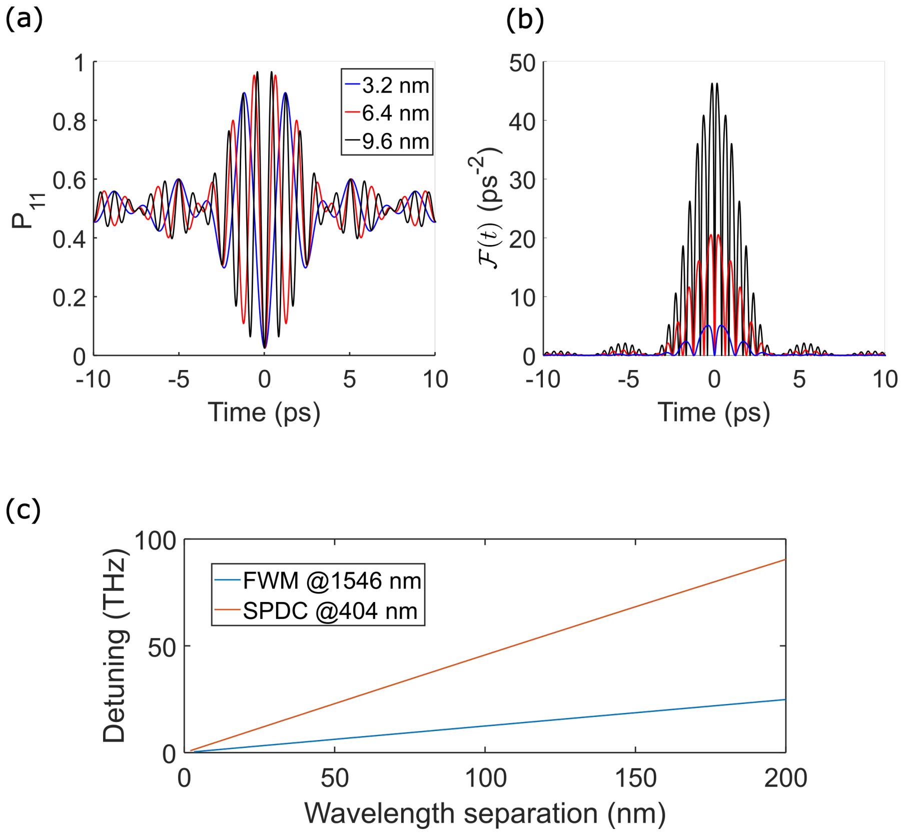

FIGURE 3.30. **HOM interferences from the photonic chip [138].** (a) HOM interference for $\delta = 3.2\ nm$ (blue), $\delta = 6.4\ nm$ (red) and $\delta = 9.6\ nm$ (black) with their corresponding Fisher information plotted in (b). (c) Comparison of the detuning (THz) versus wavelength separation of the signal and idler between the photon pairs source through four-wave mixing on the photonic chips (blue) and the spontaneous parametric down conversion from the bulk source of this chapter (orange).

separation of $\sim 10\ nm$ is lower than $\mathscr{F}(t)$ from the source presented in this chapter with the same wavelength separation. It is because $\mathscr{F}(t)$ is proportional to the frequency of the beat note. The on-chip source is using four wave mixing where the signal and idler have a wavelength similar to the pump ($\sim 1550\ nm$). Fig. 3.30(c) shows the detuning in THz function of the wavelength separation in nm for the SPDC and the FWM source. To obtain the same detuning with the FWM source, the wavelength separation between the signal and the idler needs to be higher than the SPDC source. Huge wavelength separation means more problems due to the dispersion and the good functioning of the optics components working for specific wavelength (*e.g.* detectors). To achieve similar Fisher information, either the wavelength of the generated photon pairs needs to be smaller (which is hard for photonic chips) or more photons probes (brighter photons pair source) would be required. Despite the lower amount of Fisher information due to the centred wavelength of the downconverted photon pairs, this strategy of measurement could provide single-shot measurement with a phase-stable photon pairs source for depth imaging using HOM interferometry without fringe ambiguity.

3.8 Conclusion

In this chapter, it has been shown that with the help of an estimator saturating the Cramér-Rao bound, Hong-Ou-Mandel microscopy can achieve sub-μm axial precision for depth imaging with $\sim 10^4$ photon pairs detected and 12.3 nm of wavelength separation between the signal and idler of a two-colour entangled state. The Fisher information of the microscope has been tuned by controlling the temperature of a non-linear crystal inferring on the wavelength separation of the downconverted photons for narrowband source without tuning the wavelength of the pump.

In section 3.6.5 depth imaging is performed on a semi-transparent sample by monitoring the normalised anti-bunching coincidence counts. Increasing the wavelength separation between the downconverted photons increased the axial precision of depth imaging from 2.4 μm ($\Delta\nu = 3.4\ THz$) to 1.1 μm ($\Delta\nu = 7.4\ THz$) and $N \sim 10^3$ photon pairs detected. Then, the precision of the microscope has been characterised for single-pixel imaging in section 3.6.6, demonstrating that depth imaging with sub-μm could be performed with a wavelength separation of 12.3 nm and $N \sim 10^4$ photon pairs detected. A sub-fs time delay measurement has been realised, corresponding to an improvement in the precision of three order of magnitude over the original HOM paper [72] and applied to depth imaging. This shows how HOM microscopy could be used for photon-sensitive sample such as biological cells to characterise sub-cellular structures with a probe illumination to the sample of $\sim fW$. This signifies that the HOM microscope can achieve performances of super-resolution microscopes with a probe light intensity of $10^{-8}\ W.cm^{-2}$ incident on the sample, corresponding to 8 to 12 order of magnitude below conventional super-resolution microscopy [114, 128]. The work realised in this chapter focus on the axial precision by tuning the frequency separation between the two photons of a wavelength-entangled state. However, another way to improve the resolution would be to increase the brightness (or decreasing the loss) of the source and therefore the number of photon pairs detected. The loss in this experiment were relatively high and have been reported to be $\sim 98\%$ for each photon. This was mainly caused by the FC to FC fibre connectors included 6 dB loss between the source and the output. The second cause explaining the high loss was the heralding efficiency, limited to be $\eta = 30\%$. This is due to the experiment being build with free space optics, where the efficiency of the detectors (60%), the dispersion of the light and the loss within the optics were limiting factors. Reducing the loss and increasing the brightness of the source is directly affecting the number of detected photons N and the Fisher information achievable in the experiment. Therefore, optimising the parameter N improves the precision of the estimates.

Finally, in section 3.7, an alternative is to have the photon pair source on a photonic chip. It would allow the generation of downconverted photons with a broader spectrum. Using wavelength division multiplexer, simultaneous HOM interferences with different beat notes could allow an improvement in the precision of the estimates without having fringe ambiguity. It would increase the dynamic range initially limited by fringe ambiguity due to the variation in thickness of the sample too big compared to the half-period of the beat note. Working with the photonic chip on the source would first avoid the potential errors due to the phase-locking instabilities in the measurement discussed in section 3.6.6, and would allow depth imaging with HOM interferences without fringe ambiguity by simultaneously monitoring HOM interference with different beat notes.

Further improvements could be done for HOM microscopy by engineering wavelength-entangled photon pairs with higher detuning. For a photon pair source with $\Delta\nu = 150\ THz$ ($\lambda_i = 933\ nm$ and $\lambda_s = 700\ nm$), the Fisher information per photon could reach up to $10^6\ ps^{-2}$ (equivalent to $\sigma = 1\ fs$) for measurements saturating the CRB. Combined to a bright photon pair source with periodically poled KTP in a waveguides similar to [56, 154], where pure photons could be generated with a brightness up to 10^6 photons pairs per second could potentially achieve a similar resolution than the work from Lyons et al. [99] for an acquisition time of $\sim 1\ s$. Indeed, Lyons et al. achieved attosecond resolution with a high number of photon pairs detected due to a long acquisition time (1.4 to 15.6 hours), which cannot be applied to raster-scan imaging as the acquisition time of the image would be too long. Therefore, increasing the Fisher information per photon coupled to a bright photon pair source would allow nanometre resolution applied to depth imaging.

From a fourth-order quantum interference originally discovered to measure the time delay between two photons of a same pair, the work from this chapter demonstrates that the same effect can be used for depth imaging with high performances to sub-μm axial precision. Improvements and further work could provide high depth imaging for the nm scale and maintaining a probe of illumination to the sample ultra-low. The dynamic range offered by measurement techniques of this type combined with high precision could be particularly relevant for characterising in situ, sub-cellular structures for semi-transparent samples such as biological cells.

CHAPTER 4

PRECISION ENHANCEMENT WITH BRIGHT-SQUEEZED LIGHT FOR STATIC-LOSS MICROSCOPY.

In metrology, the performance of measurements for sensing and imaging is theoretically limited by the shot-noise limit (SNL, also called QNL for quantum noise limit) due to the Poisson-distribution of photon number in laser radiation. The QNL defines the best sensitivity achievable with classical light for a given apparatus and photon number [147]. However additional noise from experimental imperfections (*i.e.* non-ideal detectors or devices driving the experiment and manipulating the probe state) can lead to a degradation of the measurements [3, 38, 43, 54, 136]. Several noise reduction techniques for the detectors and the probe laser have been developed to approach the QNL. For instance, the noise induced fluctuations to the signal can be averaged and removed from the measurements [171]. However this is not sufficient to reach the QNL and an improvement of this technique consists of simultaneously monitoring the noise with a sample beam and subtracting it from the probe beam with homodyne detectors [69]. With QNL detectors, to limit the perturbations from external noise; for example, QNL high-power laser system for gravitational wave detections have been demonstrated [89, 90]. Furthermore, quantum technologies such as quasi-photon number resolving detections schemes on classical states have shown improvements in the noise reduction to a point where QNL has been reached [60]. Removing thermal noise by cooling down the experiment to few K [47] can help to achieve QNL measurements, or it can be approached at room temperature for interferometry measurements by engineering device dimension and material [171]. Finally, it is possible to develop algorithms and machine learning to remove excess noise within the measurements, approaching the QNL [88, 166]. Because the QNL derives from the inherent fluctuations of the classical states, according to the laws of quantum mechanics measurements below this fundamental limit for a classical probe are forbidden.

Quantum probes of light have shown to enhance in the measurements, achieving experimentally sub-shot noise performance [63, 103]. For instance photon counting experiments using twin-beams [105] have demonstrated sub-shot noise measurements by using the intensity correlation between the two photons of the same pair [124, 145]. Furthermore, the preparation of multi-photon entangled states such as $NOON$ states which correspond to a superposition of N photons across two single optical modes have experimentally demonstrated a super-sensitivity and precision enhancement within the measurements below the QNL [108, 140]. The generation of these probe states exploits a low efficiency process, thus the brightness of such probe beams is typically limited to around a picowatt [6, 111]. It allows improved performance at a low illumination level where photo-damage and photo-toxicity within the sample can be avoided. However, where the performance of a measurement could benefit from a brighter probe, there is usually a gap between the brightness of such quantum states and the limit where damages on the sample can be visible [58].

Brighter quantum probe states such as bright squeezed light can operate in the $\sim mW$ regime and have recently demonstrated improvement in the measurements. By decreasing the fluctuation in one of the quadrature of the electromagnetic field, the optical noise floor can be lowered below the QNL. Consequently, the signal-to-noise ratio, corresponding to the minimum signal observable amongst the noise can be increased by such quantum states for higher probe of light. Therefore, one can increase the sensitivity of the measurements by improving the SNR [18, 29]. Because these measurements are done on higher frequency bandwidth to be shot-noise limited, increasing the modulation depth of the probe beam to increase the power of the signal transfers the amount of low frequency classical noise to the optical sidebands, subsequently sub-QNL sensitivity does not necessary imply sub-QNL precision [13, 147].

Here, we propose a bright Kerr-squeezed light to enhance the precision for absorption microscopy with a signal power of $\sim 200\ \mu W$. With the noise reduction given by the squeezed-state, the probe is modulated in time between two optical paths to move a static-loss measurements to a higher shot-noise limited frequency bandwidth. Working with QNL detectors and laser at this higher bandwidth, enhancement of precision within the measurements is experimentally demonstrated for absorption microscopy. Section 4.2 describes the strategy of measurements and the regime for which a precision enhancement is expected. Section 4.3 discusses about parameter estimation and the calibration of the parameters necessary for such a strategy of measurements. Sections 4.4 to 4.5 show experimental performance of the bright-squeezed source demonstrating precision enhancement in the measurements for single pixel and raster-scanning imaging. Finally, section 4.6 develops three proposals to remove the extra noise apparent in the previous measurements, improving the performance of the microscope for absorption imaging with Kerr-squeezing and section 4.7 concludes the chapter.

4.1 Statement of the work

The visible wavelength Kerr squeezing with photonic crystal fibre has been studied by George Atkinson during his PhD at the University of Bristol [14]. The theory on the Fisher information is based on his work. Furthermore, the laser and detector used in this chapter are the same that George Atkinson characterised during is PhD, showing that the frequency bandwidth $> 2\ MHz$ is shot-noise limited. Alex McMillan was my day to day supervisor. Jonathan Matthews was the coordinator of the project. In the future work, the proposal 1 is from Alex McMillan whilst the proposal 2 is from Jonathan Matthews. I built and designed the confocal microscope. Based on the MATLAB script from George Atkinson, I wrote and adapted the script to the measurement I wanted to realise (*e.g.* confocal microscopy, single-pixel measurements). I did the data acquisition and data analysis presented in the chapter.

4.2 Static loss microscopy with bright-squeezed light source

This imaging technique uses the noise reduction from an amplitude squeezed state to enhance the precision of the measurements for absorption imaging. To achieve such performance, the strategy of measurement needs to be well defined. First, to observe sub-shot noise from a photon number squeezed state, it is important to be shot-noise limited on the laser pump. The stabilisation of laser power can be done with a control-feedback loop where measurements at the quantum noise limit (QNL) at 10 Hz and for an output signal of ~ 10^2 mW have been achieved [90]. However, to achieve this degree of stabilisation, 8 photodiodes (4 to monitor the noise and 4 to monitor the output signal) and two feedback loops (one for the mode cleaner of the laser, and one to stabilise the laser power) are required. Squeezed vacuum light has demonstrated an enhancement of 9.4 dB below the QNL for laser power stabilisation in the kHz regime [152]. But similarly to previous work, the requirements are extensive with a control feedback loop and two cavities to generate squeezed vacuum light. Whilst these applications relatively low frequency can be useful in the gravitational wave detections, it is definitely easier to have a laser power at the QNL in the MHz regime and for an output power of ~ 10^2 μW. The *Mai Tai* from *Spectra-Physics* fulfils the previous requirement where QNL measurements have been done at high frequency bandwidth with the use of one detector [14]. Furthermore, this laser generates ultrashort pulses achieving high peak power and for this reason, it makes a perfect candidate for the generation of bright squeezed light via Kerr effect as discussed in section 2.5.1. As shown in Fig. 4.1, to encode static

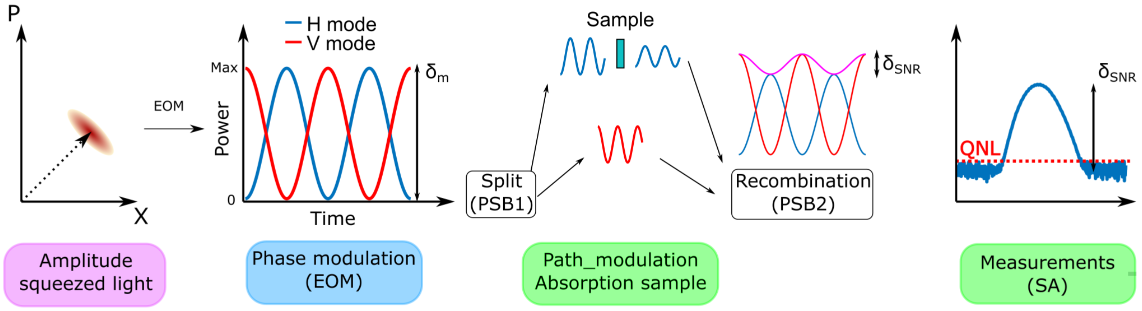

FIGURE 4.1. **Low absorption microscopy with Kerr squeezing.** An amplitude squeezed beam of light is modulated in phase between horizontal (blue) and vertical (red) polarisation modes with an electro-optic modulator (EOM). The two modes are split via polarising beamsplitter (PBS1), one of the modes interacts with the sample. After recombination with PBS2, the output signal (purple) has a modulation depth δ_{SNR} proportional to the loss induced by the sample. A spectral analyser (SA) at the frequency of the modulation is measuring δ_{SNR} for each pixel of the sample by raster-scanning and confocal imaging. The squeezed state lowers the noise floor below the quantum noise limits (QNL).

loss in the MHz bandwidth the probe beam is modulated in time by an electro-optic modulator (EOM) with a modulation depth δ_m between the horizontal (H) and vertical (V) polarisation modes. Then, with a polarising beamsplitter (PBS1) the two polarisation modes are, respectively, transmitted and reflected to two different optical modes, making the probe beam path-modulated in time. Since the PBS causes a π-shift between the two amplitude modulated beams, without the presence of the sample the combined signal exhibits no modulation at the sideband. In the presence of a sample with a transmission $\eta < 1$, one of the modes interacts with the sample and consequently its amplitude decreases due to absorption. After recombination with a second PBS2, the output signal exhibits a modulation depth δ_{SNR} at the sideband frequency due to the interaction of one of the modes with the sample. Finally, the transmission η can be inferred by measuring the signal at the sideband frequency. The detection of the light is performed with a PIN detector which exhibits a saturation level higher than the avalanche photodiode detectors used in chapter 3. The detector needs to have fast response and to be shot-noise limited at the frequency bandwidth of the signal. These requirements are fulfilled by the detector *PDB440A-AC* from *Thorlabs* [14]. Due to the high brightness of the squeezed state, homodyne detection cannot be performed to measure the noise reduction granted by the squeezed-state. Indeed, such a detection technique requires a local-oscillator (LO) much brighter than the signal (several orders of magnitude above [68]). Therefore, the squeezed light is measured on a direct detection technique commonly used for bright squeezed states [13, 29, 167]. To perform such measurements, it is necessary to be shot-noise limited, which is the case for the laser and detector used in this experiment [14].

Fig. 4.2 shows a 100 MHz span of the output signal (orange) and the electronic noise (blue) measured from the detector used in this chapter. The peak at 10 MHz, indicated by the orange arrow, corresponds to the signal, whilst the green arrows indicate the higher harmonics and the blue arrow shows the repetition rate of the laser at 80 MHz. The frequency bandwidth of this detector allows a detection of the signal with a noise clearance (NC) of ~ 3 dB from 3 MHz to 15 MHz (shown on the top right inset). Afterwards, a spectral analyser (SA) measures the output current from the photodiode in the zerospan mode. Based on the description of the SA from [119], to measure the 100 MHz span the SA scans the signal by changing the frequency of the LO in a continuous mode. During the scan the LO is mixed with the signal and sent to an intermediate frequency filter (IF) selecting a frequency component of the signal. The 3 dB bandwidth of the IF corresponds to the resolution bandwidth (RBW) and determines the frequency resolution of the measurements. Then, the signal is logarithmically amplified and an envelope detector output a voltage corresponding to the amplitude of the selected frequency component. Finally, a low-pass video filter (VBW) reduces the fluctuations of the measurement by smoothing out the output signal when $VBW < RBW$. The zerospan mode corresponds when the LO has a fixed frequency selected by the user, and no swipe over a range of frequency is done. Here, the central frequency of the zerospan mode is done either at 10 MHz to measure the signal or at 5 MHz (light blue rectangle in the inset) to measure the relative noise power when the squeezer is on and off, characterising the noise reduction from the amplitude squeezed state [14]. The characterisation of the noise reduction of the squeezed state is done at the frequency bandwidth of 5 MHz because the noise clearance is sufficient for the amplitude squeezed state used in this chapter, and the frequency bandwidth is far away from the signal (at 10 MHz) to be certain that only the noise floor is monitored at this specific bandwidth. Furthermore, Kerr-squeezing is power-dependent, therefore the noise floor needs to be compared for a similar output optical power when the squeezer is on and off, this corresponds to the calibration of the experiment and is discussed in section 4.3.1.

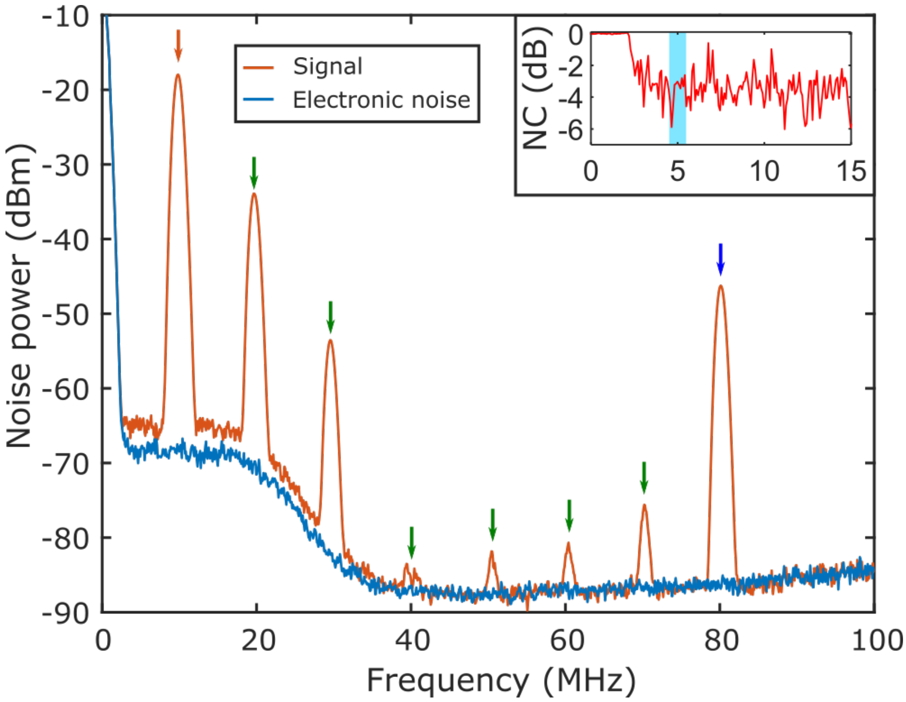

FIGURE 4.2. **100 MHz span from output signal.** The orange trace is the output signal modulated in time at 10 MHz over a 100 MHz span, where the blue trace corresponds to the electric noise from the detector. The noise clearance (NC) is shown on the top right inset from 0 to 15 MHz, where ~ 3 dB of noise clearance is observed. The light blue rectangle corresponds to the frequency bandwidth of 5 MHz where the noise measurements are made to characterise the noise reduction from the squeezed state. The orange arrow corresponds to the signal at 10 MHz, whilst the green arrows correspond to the higher harmonics. Finally, the blue arrow corresponds to the repetition rate of the laser at 80 MHz.

Because the signal is logarithmically amplified by the SA, the noise power of the optical signal when the squeezer was on and off was corrected by adding 2.27 dB to the output signal. First there is an under response of 2.51 dB due to the noise which follows a Rayleigh distribution and the SA calculates the output signal from the square of the average voltage, previously amplified logarithmically. Because the log of the average is not equal to the average of the log, a correction of 2.51 dB must be added to the output signal [7, 14]. Because the voltage of the signal is typically Gaussian distributed, this correction factors only applies on the measurement of the noise power. Secondly, the actual filter in a SA is not a perfect rectangle and there is an error in the measurements when it is used for noise measurement. The equivalent noise bandwidth (ENB) corresponds to the bandwidth of a brickwall filter which output the same integrated noise power as the actual RBW filter. By calculating the ratio between the ENB and the RBW, this error can be correct and gives a correction factor of $-0.24\ dB$ (given by the supplier). This means that 0.24 dB needs to be subtracted from the output signals [7, 14]. Therefore, the relative noise power is corrected by adding a correction factor of $2.27\ dB = 2.51\ dB - 0.24\ dB$.

4.3 Parameter estimation

The modulation δ_{SNR} infers the loss from the sample in a shot-noise limited bandwidth. From the electronic output of the detector, a maximum likelihood estimator is derived saturating the Cramér-Rao bound which makes it an optimal estimator for such a strategy of measurements.

4.3.1 Maximum-likelihood estimation and parameter calibration

The maximum likelihood estimator relies on the measurement at the zerospan mode. The spectral analyser mixes the electric current from the fast output photodiodes to a local oscillator with a fixed frequency centred at the frequency of the optical sideband. The resolution bandwidth (RBW) determines the frequency resolution of the measurements. The higher the RBW is and the faster the measurements are, therefore the less classical noise will be present within the measurements.

As discussed in section 4.2, the loss within the sample induces imbalance in the amplitude between the horizontal and vertical polarisation modes before the recombination at the second polarising beamsplitter, thus inducing photons at the sideband Ω with a modulation depth proportional to the loss from the sample. Therefore, we define δ_{SNR} the signal-to-noise ratio (SNR) at the frequency of modulation. Hence, the SNR can be calculated following:

$$\delta_{SNR} = \frac{\langle p_\Omega \rangle - \langle p_N \rangle}{\langle p_N \rangle - \langle p_E \rangle}, \tag{4.1}$$

where $\langle p_\Omega \rangle$ corresponds to the average power of the sideband at the frequency Ω in the $\pm B/2$ frequency interval, $\langle p_N \rangle$ is the average power of optical noise floor and $\langle p_E \rangle$ is the average power of the electronic noise floor. In an approximation considering low loss, that classical noise from the laser within this bandwidth is negligible and for low absorption from the sample, we have:

$$\langle p_\Omega \rangle = R\left(\frac{1}{8} i_0^2 \delta_m^2 (1-\eta)^2 + 2 q i_o \Phi B + 2q^2 \left\langle \left| \int^\Omega n_e(\nu) d\nu \right|^2 \right\rangle \right), \tag{4.2}$$

$$\langle p_N \rangle = R\left(2 q i_0 \Phi B + 2q^2 \left\langle \left| \int^\Omega n_e(\nu) d\nu \right|^2 \right\rangle \right), \tag{4.3}$$

$$\langle p_E \rangle = R 2 q^2 \left\langle \left| \int^\Omega n_e(\nu) d\nu \right|^2 \right\rangle, \tag{4.4}$$

where $\int^\Omega = \int_{\Omega-B/2}^{\Omega+B/2}$, R is the input resistance, q the electric charge of the electron, $i_0 = NqB$ is the electric photocurrent after measuring N photons within the resolution bandwidth B, δ_m is the modulation depth of the beam after passing through the electro-optic modulator (EOM), $1-\eta$ is the loss from the sample, Φ is the squeezing value, and $n_e(\nu)$ the dark noise, corresponding to the electrons generated independently of the optical field[1] [14]. From Eq. (4.1) and using Eqs. (4.2), (4.3) and (4.4), we have:

$$\delta_{SNR} = \frac{i_0 \delta_m^2 (1-\eta)^2}{16 q \Phi B}, \tag{4.5}$$

Hence, the transmission of the sample η can be written to:

$$\eta = 1 - \sqrt{\frac{16 \Phi \delta_{SNR}}{N \delta_m^2}}. \tag{4.6}$$

Because the SA does not measure the number of photons N, the output power after the whole experimental setup is calibrated to a powermeter (PW) placed before the generation of the state (see Fig. 4.3). The 'Experiment' refers to the strategy of measurement described in the previous section. To calibrate PW, a second powermeter (PW2) is temporally added to measure the output signal. Then, the motorised half-waveplate (mHWP) rotates to increase the input power into the experimental setup and the power is measured from both powermeters. The power calibration between $PW2$ and PW is shown in Fig. 4.3(b) and used to estimate N. Afterwards, the number of photons can be estimated from:

$$N = \frac{\eta_q \gamma \lambda}{hcB}. \tag{4.7}$$

λ is the wavelength of the probe beam and is equal to 740 nm, h is the Planck constant, c the speed of the light in the vacuum, η_q the efficiency of the detectors measured to be 0.85 and γ the power calibration inferred from Fig. 4.3(b).

Fig. 4.4(a) shows how the modulation depth from the electro-optic modulator (EOM) is measured. After the generation of the squeezed state, $PBS1$ splits the probe beam into two polarisation modes (discussed in the previous section). One of the polarisation mode is blocked with a beam dump to avoid the recombination. Then the modulation of the other mode is measured

---

[1] The calculations of $\langle p_N \rangle$ and $\langle p_E \rangle$ are detailed in [14], appendix **A.1**, while the calculation of $\langle p_\Omega \rangle$ can be found in the appendix **B.1**.

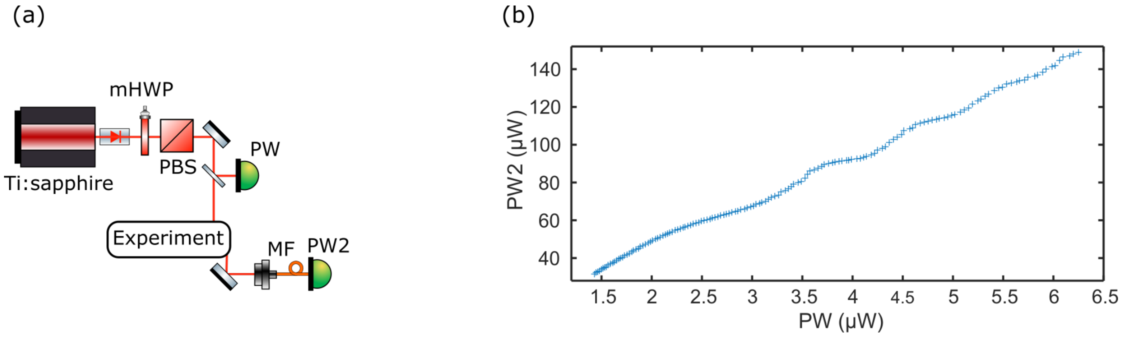

FIGURE 4.3. **Output power calibration.** (a) Input of the laser toward the experiment is controlled with a motorised half-waveplate (mHWP) and a polarising beamsplitter (PBS). Before the light is sent to the experimental setup, a waveplate reflects up to 4% of the light measured with a powermeter (PW) whilst the experiment is running. A second powermeter (PW2) is temporally added at the output of the interference to calibrate the output signal with respect to the output of the first one, PW. (b) Output power calibration with the powermeter PW.

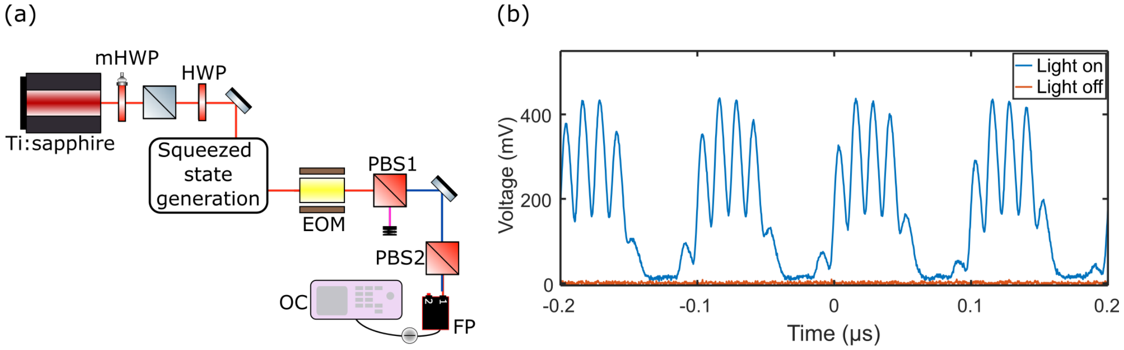

FIGURE 4.4. **Calibration of the depth modulation.** (a) After generation of the squeezed state, an electro-optic modulator (EOM) modulates the optical beam between two polarisation modes in time at a frequency $f = 10\ MHz$. One of the polarisation mode is blocked with a beam dump to measure the modulation depth induced by the EOM with photodiode with fast output (FP, *PDB450A*, *Thorlabs*) and an oscilloscope (OC). (b) Modulated signal measured when the laser is on (blue) and when the laser is off (orange). The modulation depth can be calculated from the visibility of the signal.

with DC photodiode with fast output (FP, *PDB450A*, *Thorlabs*) and the results are shown by the blue trace in Fig. 4.4(b). By calculating the visibility of the output signal and correcting the absolute 0 of the measurements when there is no light (orange trace), the modulation depth δ_m can be calculated. The maximum depth modulation achieved by the EOM is $\delta_m = 0.98 \pm 0.04$.

The calibration of these parameters is subject to the noise within the devices used to measure them. From Eq. (4.6), we can observe that if these parameters fluctuate during the experiment, the variance of η will be affected and no enhancement can be done. However, the power stabilisation of the laser used in this chapter has been measured at the QNL [14] and the EOM used to modulate the light has been designed for this experiment by *QUBIG*. Finally, to decrease the effect of the classical noise within the experiment on the variance of the estimate η, the measurements of δ_{SNR} are taken with a $RBW = 1\ MHz$ corresponding to a data acquisition of $t = 1\ \mu s$. We will see in section 4.5.3 that if we consider a longer time scale, the precision of the microscope is degraded by classical noise. Finally, in section 4.6 experimental protocols are proposed to correct the effect of classical noise on the performance of the microscope.

4.3.2 Fisher information

The Fisher information $\mathscr{F}(\eta)$ can be computed using [91]:

$$\mathscr{F}(\eta) = \left(\frac{\partial \delta_{SNR}}{\partial \eta}\right)^2 \mathscr{F}(\delta_{SNR}), \tag{4.8}$$

here $\mathscr{F}(\delta_{SNR})$ is determined by the expression:

$$\mathscr{F}(\delta_{SNR}) = \left(\frac{\partial p_\Omega}{\partial \delta_{SNR}}\right)^2 \mathscr{F}(p_\Omega). \tag{4.9}$$

Since p_Ω serves as an unbiased estimator, $\mathscr{F}(p_\Omega)$ is given by $[Var(p_\Omega]^{-1}$. The variance of the power at the sideband $Var(p_\Omega)$ for M spectral average is expressed as follow [14][2]:

$$Var(p_\Omega) = \frac{R^2}{M}\left(\frac{1}{2} q\delta_m^2(1-\eta)^2 i_0^3 \Phi B + \frac{1}{4}\delta_m^4(1-\eta)^4 i_0^4 Var(\Re[\mathscr{H}]) + q^2\delta_m^2(1-\eta)^2 i_0^2 Var(\Re[\mathscr{N}])\right),$$

where $\mathscr{H}$ and $\mathscr{N}$ represent the stochastic noise of the laser at low frequency and the electronic noise integrated over the sideband Ω within the RBW $\pm B$. Due to the noise clearance of $3\ dB$ mentioned in the section 4.2, terms in conjunction with $Var(\Re[\mathscr{N}])$ are neglected.

Therefore, the Fisher information $\mathscr{F}(\eta)$ from the estimator in Eq. (4.6) is given by [14]:

$$\mathscr{F}(\eta) = M\left(\frac{8\Phi}{N\delta_m^2} + 4(1-\eta)^2 Var(\Re[\mathscr{H}])\right)^{-1}, \tag{4.10}$$

where $Var(\Re[\mathscr{H}])$ corresponds to the noise of the DC component of the classical relative amplitude noise from the laser and modulator, and M is the number of spectral average. Because only the amplitude at the sideband of the frequency $f = 10\ MHz$ is monitored, for this strategy of measurements we have $M = 1$. Furthermore, Eq. (4.10) assumes $(1-\eta) << 1$ where loss is negligible and the noise reduction from the squeezed state is not affected by it. Since the measurements are carried out at the frequency of the sideband, $\mathscr{F}(\eta)$ increases with the modulation depth δ_m. Indeed, the number of probe photons at the sideband increases with δ_m because only the light oscillating at this frequency is monitored.

---

[2] The calculation are given in details at the appendix **B.2** from [14].

Finally, if the classical noise $Var(\Re[\mathscr{H}])$ from Eq. (4.10) is negligible, we can define the Cramér-Rao bound (CRB) as:

$$CRB = \left(\frac{N\delta_m^2}{8\Phi}\right). \tag{4.11}$$

Because the estimator from Eq. (4.10) saturates the CRB [14], Eq. (4.11) corresponds to the bound for which the smallest variance $Var(\eta)$ can be experimentally achieved with $Var(\eta) = 1/CRB$ (see section 2.3.2).

4.4 Bright amplitude-squeezed source

Fig. 4.5(a) shows the experimental setup to generate Kerr squeezing. It consists of propagating two coherent beams into a non-linear medium in an interferometer. The brighter beam (or strong beam) triggers the non-linear effect to induce self-phase modulation. Because the power of the weak beam is not strong enough, it transmits through the non-linear medium without triggering the Kerr-effect. Afterwards, both beams interfere and the weak beam displaces the strong beam in the quadrature space resulting in an amplitude-squeezed state at the output of the interferometer (see section 2.5.1). Here, the pulse laser (*Ti:sapphire*, *Mai Tai*) generates 100 fs pulses with a repetition rate of 80 MHz at a central wavelength $\lambda = 740$ nm. The source comprises a Sagnac interferometer with a $90:10$ beamsplitter and a 14 m long photonic crystal fibre (PCF) as a non-linear medium in the centre of the interferometer. The wavelength of the laser has been chosen to decrease the effect of dispersion within the fibre by compensating it through the effect of non-linearity, ideally generating an optical soliton [28, 122]. The small core of the PCF (2.09 μm) provides a tight mode confinement within the fibre to enhance the non-linearity. Because Kerr squeezing is power dependent, a motorised half-waveplate (mHWP) and a polarising beamsplitter (PBS) control the power of the light propagating toward the PCF, where the unused beam (the reflected beam from the PBS) is blocked with a beam dump (BD). The PCF is a birefringent medium, therefore HWP_1 rotates the anti-clockwise input polarisation to be matched with the polarisation axis of the fibre. Then, HWP_2 corrects the undesirable polarisation rotation induced by the PCF after the light is transmitted through it. It ensures the clockwise and anti-clockwise propagation beam after transmission through the medium to interfere at the BS, generating an amplitude-squeezed state. Therefore, to generate a coherent state with the experimental setup, HWP_2 is rotated to have both directions of propagation with polarisation orthogonal to each other, cancelling the interference and the generation of the amplitude squeezed-state. Finally, after passing through the Sagnac interferometer, the light is coupled to a multimode fibre (MF) with $\sim 92\%$ coupling efficiency and is detected with balanced amplified photodiode detectors with fast output (FP) (PDB440A-AC, Thorlabs), reporting an efficiency of $\eta_{eff} = 0.85$. The powermeter PW corresponds to the power calibration discussed in the section 4.3.1 and is calibrated before each measurement.

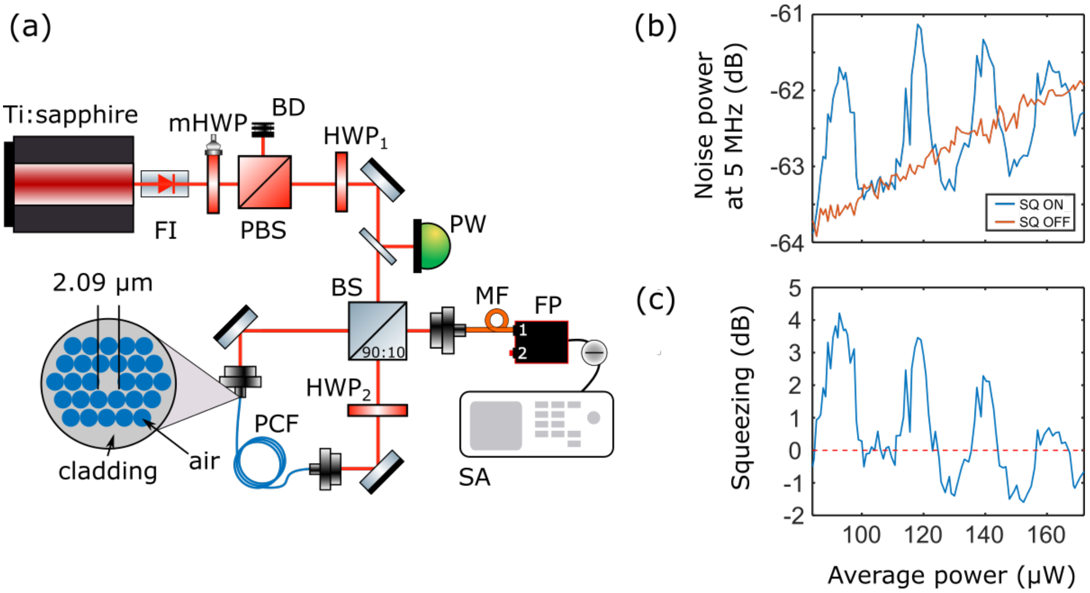

FIGURE 4.5. **Bright amplitude squeezed source.** (a) Ti:sapphire Mai Tai pulse laser (100 fs pulse, 80 MHz repetition rate at $\lambda = 740\ nm$) propagates toward a Sagnac interferometer with a 90 : 10 beamsplitter (BS) and a 14 m long photonic crystal fibre (PCF). HWP$_1$ matches the input polarisation with the main polarisation axis of the fibre, whilst HWP$_2$ corrects the polarisation rotation of the beam after propagating through the PCF. The output light is coupled to a multimode fibre (MF) and measured with AC fast output photodiode detector (*PDB440A-AC*, Thorlabs), whilst the photocurrent is sent to an electronic spectral analyser (*FPC1000*, Rohde & Schwarz). A Faraday optical isolator (FI) avoid any back-propagation within the laser. The input power is controlled with a motorised HWP (mHWP) and a polarising beamsplitter (PBS), whilst the unused reflected light is blocked by a beam dump (BD). (b) Noise power at the 5 MHz bandwidth when the squeezer is on (blue) and off (orange) for different value of the pump power. (c) Calculated squeezing from (b) using Eq. (4.13).

Fig. 4.5(b) shows the relative noise (in dB) measured by a spectral analyser (SA, *FPC1000*, *Rohde & Schwarz*) while the input power is slowly increased by using mHWP. The non-linear phase-shift Φ_{NL} from Eq. (2.51) discussed in section 2.5.1 varies with the input power $\langle P \rangle$, periodically switching the source from an amplitude squeezed (dip) output to anti-squeezed output (peak) configuration as shown in Fig. 4.5(b). The x axis corresponds to the power inferred from the calibration of PW. As discussed in section 4.2, the noise is measured at the central frequency of 5 MHz in the zerospan mode and with a resolution bandwidth (RBW) of 1 MHz. The blue trace (SQ ON) corresponds to an angle of HWP$_2$ when the clockwise and anti-clockwise propagation beams within the Sagnac interfere to generate the amplitude squeezed state, whilst the orange trace (SQ OFF) is a measurement of the shot-noise level from the coherent state where HWP$_2$ is mis-matching the polarisation of the two propagation modes, cancelling the generation of the squeezed-state.

The noise reduction from the squeezed state can be calculated using:

$$\Phi = \frac{10^{SQ/10} - 10^{DK/10}}{10^{SN/10} - 10^{DK/10}}. \tag{4.12}$$

SQ and SN are respectively the measured noise when the squeezer is on (SQ) and off (SN), whilst DK corresponds to the dark current, as known as the electronic noise of the detectors. We define Φ_{log}, the noise reduction in a logarithmic scale to be:

$$\Phi_{log} = 10 \times log_{10}\Phi. \tag{4.13}$$

Fig. 4.5(c) shows the noise reduction Φ_{log} calculated from Fig. 4.5(b) with Eq. (4.13). As expected from Kerr squeezing, changing the input power within the non-linear medium varies the phase Φ_{NL}. The best amplitude squeezed light generated by the source is reported to be $\Phi_{log} = -1.60\ dB$ for an average power of 152.4 μW. By taking in account the loss in the experiment (measured to be ∼ 12 %) and the efficiency of the detector, the source could theoretically generate up to $\sim -2.4\ dB$ of amplitude squeezed light.

4.5 The amplitude-squeezed microscope

Fig. 4.6 shows the amplitude-squeezed microscope, where the probe beam is generated with the source through Kerr-squeezing presented in the magenta square and has been described in the previous section. After the Sagnac interferometer, the beam experiences in the blue square a phase-modulation at 10 MHz with an electro-optic modulator (EOM, *AM7-NIR*, *QUBIG*) between the vertical and horizontal polarisation modes. To maximise the efficiency of the EOM, the polarisation is initially cleaned with quarter, half-waveplates (QWP, HWP) and Glan-Taylor polariser (GT). Then, a second QWP after the GT rotates the polarisation of the state from linear to circular. An arbitrary waveform generator sends a sine wave to the EOM with a frequency of 9.87 MHz and an amplitude of 10.0 V. These values were chosen to optimise the modulation depth of the signal. To encode static loss in a higher frequency bandwidth, a polarising beamsplitter (PBS) transmits the horizontal and reflects the vertical polarisation modes, inducing a π-shit between the two modes. The signal is now path-modulated in time. As discussed in the section 4.2, without the presence of a sample, after recombination of the two polarisation modes with a second PBS the output signal exhibits no modulation. However, with the presence of a sample inducing loss on the horizontal polarisation mode, the output signal is modulated in time with a modulation depth δ_{SNR} proportional to the loss induced by the sample. Afterwards, the sample is raster-scanned on a 2D plane orthogonal to the direction of the probe beam's propagation. Confocal microscopy is performed with two confocal lenses (CL) with focal length of $f = 9.66\ mm$. The focal length were choosen according to GaussianBeam (see appendix A.4). The lateral resolution of the microscope is estimated with a resolution target technique described

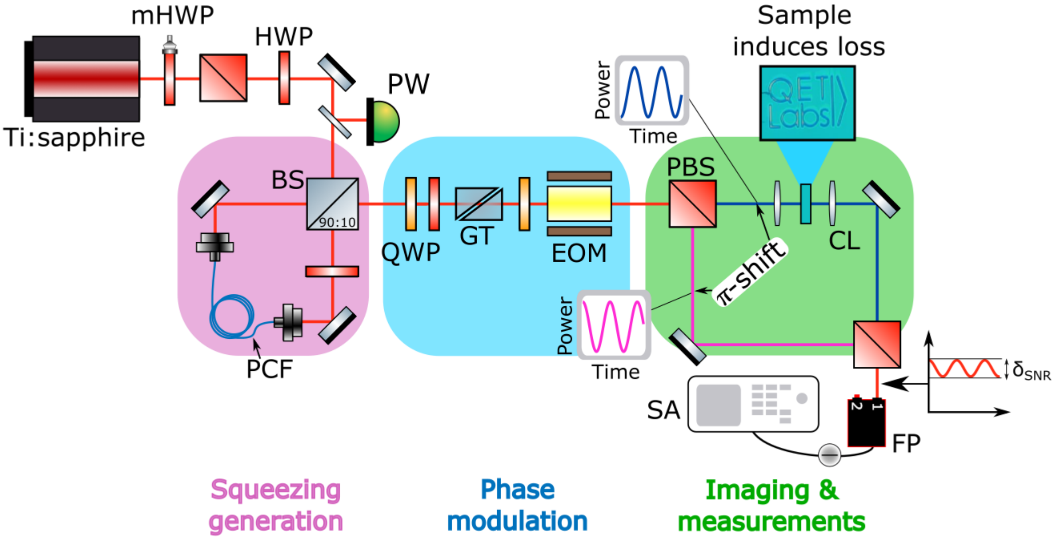

FIGURE 4.6. **Bright-squeezed light microscope.** An amplitude squeezed beam of light is generated from the Sagnac source shown from Fig. 4.7(a). At the output of the Sagnac interferometer, the polarisation is cleaned with quarter, half-waveplates (QWP, HWP) and a Glan-Taylor (GT) to be phase-modulated between vertical (V, magenta) and horizontal (H, blue) polarisation modes at 10 MHz via an electro-optic modulator (EOM, *AM7-NIR*, *QUBIG*). The EOM is controlled by an arbitrary waveform generator sending a sine wave at a frequency of 9.87 MHz and an amplitude pic to pic of 10.0 V. (c) The polarising beamsplitter (PBS) transmits H and reflects V polarisation modes. A π-shift occurs between the two polarisation modes after the first PBS (shown on the plot). The sample (AR coated glass with features made with an ion beam) is between two lenses (CL, focal length f = 9.66 mm) in a confocal configuration. Two piezo translation stages moves the sample on a 2D plane. The loss induces by the sample on the H mode infers a modulation depth δ_m after recombination of the two beams at the second PBS. The output is detected by fast output photodiodes detectors (FP) whereas the resulting electric signal is sent to a spectral analyser (SA). BD = beam dump. Note that the two different colours of the beam between the two PBS are just here to distinguish the horizontal to the vertical polarisation modes.

in section 3.6.1, where a lateral resolution of ~ 10×10 μm^2 was measured. Finally, the output signal is coupled to a multimode fibre (MF) achieving a coupling efficiency of ~ 92 % for both polarisation modes. Fast output photodiode detector (FP) and an electronic spectral analyser (SA) measures the signal in the zerospan mode with a resolution bandwidth (RBW) of 1 MHz centred at the frequency of the sideband. The transmission $\hat{\eta}$ is estimated with Eq. (4.6).

4.5.1 Low static loss estimation

The advantage of this microscope relies on the noise reduction given by the amplitude squeezed light generated by the source described above to enhance the precision of the estimates. However, it is well known that loss on a squeezed state is mathematically equivalent to interfering the state with a vacuum state (which is a coherent state) and therefore decreasing the noise reduction.

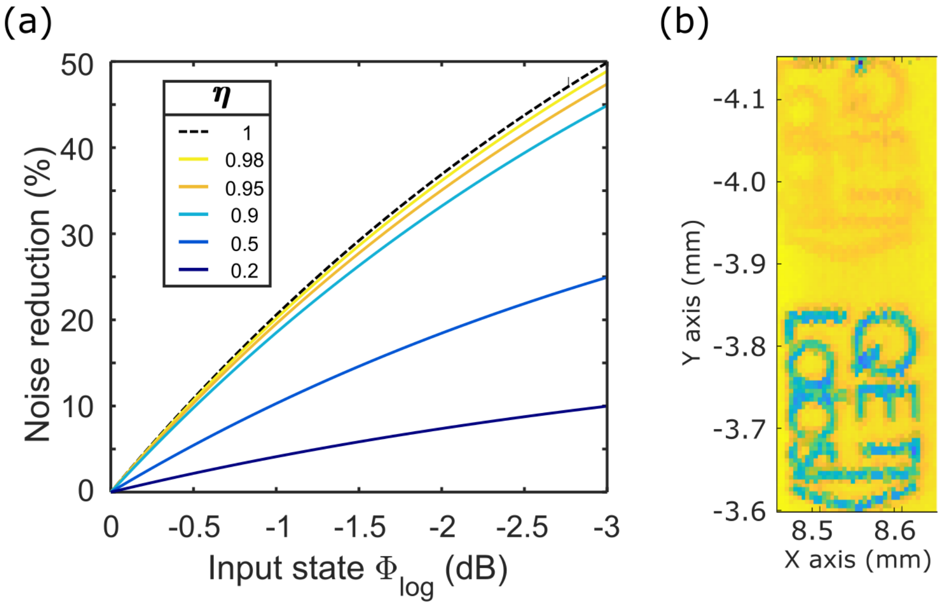

FIGURE 4.7. **Affect on the noise reduction from a squeezed state for different sample transmission.** (a) Theoretical plot of the noise reduction (y axis in %) granted by a squeezed state Φ_{log} in dB (x axis) for different transmission η. The dashed black line represent the noise reduction for different value of squeezing with no sample (no loss). (b) Raster-scanning imaging of the sample by measuring the transmitted light with a powermeter whilst the sample is moved on a 2D-plane between two lenses in a confocal configuration. The top image exhibits a contrast imaging of ~ 2% and the bottom image ~ 10%. The code colour from (a) matches the code colour from (b).

For a given Φ, the new squeezing value Φ_η after loss $(1-\eta)$ is given by [15]:

$$\Phi_\eta = \eta(\Phi - 1) + 1. \tag{4.14}$$

Because the sample is imaged by measuring η for each pixel, the loss induced by the sample can affect the squeezing value of the input state, hence losing the advantage of the scheme. Fig. 4.7(a) shows the theoretical noise reduction granted for different squeezing value Φ_{log}. The black dashed trace is the noise reduction in the measurement outcomes by varying the squeezing value of the input state when there is no loss ($\eta = 1$). When the loss increases (η decreases), the noise reduction for a given squeezing value is affected. It is evident that for a transmission sample of

$\eta = 0.2$ (dark blue trace), the noise reduction from the squeezed state are drastically affected. For instance, with $\Phi_{log} = -3\ dB$, and $\eta = 0.2$, the noise reduction are equivalent to a squeezing value $\Phi_{log} = -0.44\ dB$ with no loss. However, in this chapter, the sample (Fig. 4.7(b)) has been chosen due to its high transmission characteristic ($\Delta\eta \sim 2\ \%$ of contrast with a maximum transmission of $\eta \sim 98\ \%$ for the top image), hence the noise reduction are not highly degraded (light yellow for $\eta = 0.98$ and dark yellow trace for $\eta = 0.95$) and the advantage of the scheme can be maintained.

4.5.2 Single pixel absorption

Using Eq. 4.6, the transmission η of a single pixel from the sample (AR coated NKB-7) is estimated through the measurements of δ_{SNR} for different values of Φ. The quantum advantage (QA) is defined to be the ratio of the experimentally measured variance of the estimator for an unsqueezed state ($\Phi = 1$) and a squeezed state ($\Phi \neq 1$) with the same output power. Then, the QA is given by:

$$QA = \frac{Var\left(\eta(\Phi = 1)\right)}{Var\left(\eta(\Phi)\right)} = \frac{1}{\Phi}. \tag{4.15}$$

As discussed in the section 4.2, the zerospan mode centred at 5 MHz measures the relative noise power when the squeezer is on and off with the same detected power to estimate Φ. Then, the zerospan mode centred at the frequency of the sideband (10 MHz) is measured by the SA on a single sweep of 2 ms with a RBW of 1 MHz. The single sweep outputs 1183 independent measurements and each of them are taken with an acquisition time $t = 1\ \mu s$ (RBW^{-1}). A single-pixel measurement corresponds to 20 sweeps. For each single sweep, every 50 measurements, the variance is calculated. A single sweep corresponds to 1183 measurements, therefore 23 variances are calculated for each sweep. Subsequently, the variance of the i^{th} sweep σ_i^2 is calculated from the mean of these 23 variances. By applying this procedure to the 20 sweeps, a new data set of 20 variances $\{\sigma_1^2, \sigma_2^2, ..., \sigma_{20}^2\}$ is generated. In the new data set, every variance represents the average variance of a single sweep for a measurement with an acquisition time $t = 1\ \mu s$. Finally, $Var(\eta)$ is calculated from the mean of the new data set whilst the error bar is calculated from the standard deviation of the new data set. This process is repeated for different values of Φ and the results are shown in Fig. 4.8(a). The experimental data (blue dots) follows the predicted behaviour of the QA toward Φ (orange line) given by Eq. (4.15). The best QA of 1.2 ± 0.2 is achieved for a noise reduction $\Phi = 0.82$. This result demonstrates an improvement in the variance of the measurements achieved by the noise reduction granted by the squeezed state when comparing to an unsqueezed state with a similar output power.

Afterwards, a second analysis compares the variances $Var(\eta(\Phi))$ calculated previously for each value of Φ to the Cramér-Rao bound (CRB), and the results are shown in Fig. 4.8(b). We can observe that the experimental data points (blue dots) are in agreement with the theory (orange line) corresponding to a fit of the Fisher information $\mathscr{F}(\eta)$ from Eq. (4.10) with a R-squared of 99.2%. The fit gives a value of $Var(\Re[\mathscr{H}]) = (6.8 \pm 0.9) \times 10^{-7}$, preventing the measurements to saturate the CRB. Encoding static loss to higher frequency bandwidth by modulating the light in time allows to take measurement in a shot-noise limited bandwidth. However, the laser is not shot-noise limited at low frequency. Due to the high modulation depth δ_m which has been increased to improve $\mathscr{F}(\eta)$, the noise at the carrier frequency is transferred to the sideband. This extra classical noise degrades the performance of the microscope by increasing the uncertainty on the measurements, resulting to a higher calculated variance for the unsqueezed state than an expected variance from a coherent state saturating the CRB. This excess noise causes a deviation of the measurement from the CRB whilst the squeezing increases.

Furthermore, we observe that for $\Phi_{log} = -0.88\ dB$, the variance of the measurements is similar to a coherent state saturating the CRB (indicated by the horizontal dashed line QNL). This result demonstrates that the noise reduction from the squeezed state decreases the uncertainty within the measurements. For the unsqueezed state which does not saturate the CRB, manipulating the state to generate an amplitude squeezed-state allows measurements with a performance similar to a coherent state saturating the CRB. Following the trend of the experimental fitting, we can expect sub-shot noise measurements for the same experimental setup presented here and with a noise reduction $\Phi_{log} < -1.2\ dB$. Therefore, repeating the experiment with the noise reduction $\Phi_{log} = -1.6\ dB$ achieved in the section 4.4 could achieve sub-shot noise measurements,

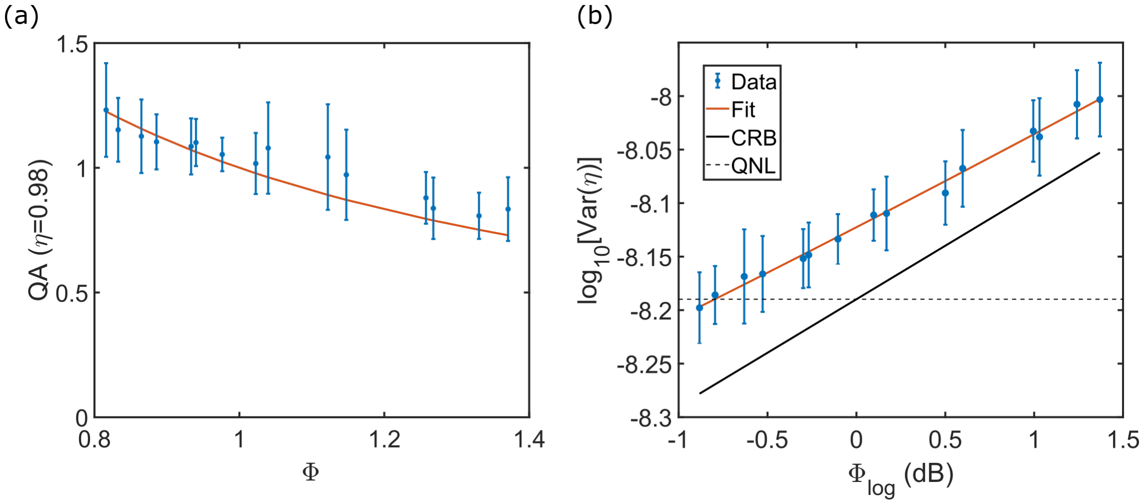

FIGURE 4.8. **Quantum advantage for single pixel estimation.** (a) Quantum advantage for different value of Φ. The orange line is the theory from Eq. (4.15). (b) Calculated variance of the estimates η for different value of Φ in a logarithmic scale. The blue data points and the error bars are experimentally calculated (the data points use the same measurement than (a)), the orange line is a theoretical fit from Eq. (4.10) with a R-squared of 99.2 %, the black line is the Cramér-Rao bound defined in Eq. (4.11) and the dashed black line corresponds to the quantum-noise limit defining the smallest variance achievable for a shot-noise limited classical state with a similar output power.

resulting to the performance that a coherent state saturating the CRB cannot achieve for a similar output power.

4.5.3 2D raster-scanning imaging

After performing single-pixel estimation and experimentally demonstrating improvement in the variance of measurements for an amplitude squeezed state, raster-scan imaging is performed on the sample. The sample consists of an AR coated NKB-7, where the shape of a 'KET' was etched by partially removing the coating with an ion beam. It results into a sample with a transmission from 95 % to 98 %. The relative noise power characterising Φ and the amplitude of the signal at the sideband frequency δ_{SNR} were measured as described in section 4.5.2 but for a single sweep only. Then, after measuring the relative noise power and δ_{SNR}, two translation stages ($PDX1/M$, $ORIC$) moved the sample in a 2D plane orthogonal to the direction of propagation of the probe beam. Because the SA and the translations stages were not synchronised, a pause of 0.2 s between the measurements of each pixel avoided positioning errors. The raster-scan imaging over a surface area of 1.7×10^{-2} mm^2 was performed in a total acquisition time of ~ 8 min corresponding to ~ 3 s per pixel. The total acquisition time per pixel is twice as fast as the motorised translation stages from the HOM microscope in section 3.6, however the gap between the total acquisition time and the data acquisition time is bigger for the piezo translation stages. The translation stages were fast (up to 2 mm/s) and the limiting factor was the positioning error. A synchronisation between a single sweep of the SA and the position of the translation stage could enhance the speed of the imaging.

Fig. 4.9(a) shows the raster-scan imaging for $\Phi = 0.87$, whilst Fig. 4.9(b) demonstrates the QA defined by Eq. (4.15) by comparing the measurements of the amplitude squeezed state with the measurements of an unsqueezed state. The QA is measured to be 1.14 ± 0.1, demonstrating precision enhancement for absorption imaging with an amplitude squeezed state compared to an unsqueezed state. We can observe that the measured QA is in agreement with the theory defined by $QA = 1/\Phi$. The measured noise reduction Φ is monitored for each pixel of the sample and reported on Fig. 4.9(c). For the whole image, we measure $\Phi = 0.87 \pm 0.04$ ((-0.62 ± 0.2) dB). Within the error of the measurements, the noise reduction granted by the squeezed state is not significantly degraded due to the high transmission of the sample as discussed in section 4.5.1. The noise reduction Φ achieved during the imaging does not correspond to the best squeezing value achieved by the source (measured to be -1.6 dB in section 4.4 and -0.88 dB in section 4.5.2). This low noise reduction achieved in this section might be due to dust on the photonic crystal fibre. The most likely reason behind the difference in the measurements of the noise reduction between the single pixel and imaging measurements is dust accumulation at the edge of the photonic crystal fibre. In fact the two measurements were taken a few days apart and for this reason the fibre needed to be cleaved again.

Fig. 4.9(d) compares the calculated variance $Var(\eta)$ of each pixel of the imaging for the

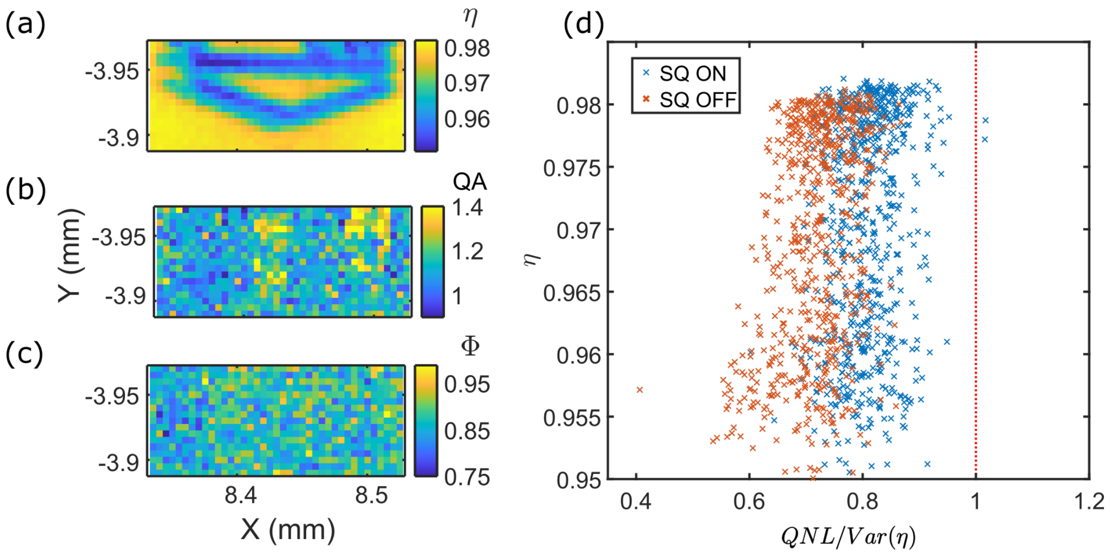

FIGURE 4.9. **Low-static loss microscopy with bright amplitude squeezed probe beam.** (a) Raster-scanning imaging by monitoring δ_m for each pixel of the sample. The transmission is estimated using Eq. (4.6). (b) Quantum advantage by comparing the variance for each pixel from (a) to another image with the same brightness and $\Phi = 1$. (c) Measured Φ for each pixel by measuring the noise at 5 MHz and using Eq. (4.12). Measured values of Φ follow a normal distribution, with $\Phi = 0.87 \pm 0.04$. (d) Normalised variance of each pixel, function of the measured transmission η to the QNL (quantum-noise limit) for two images, either whilst the squeezer was on (blue) or off (red, coherent state). The QNL is given by the CRB for $\Phi = 1$. The red dashed line corresponds to the QNL and measurements above it are sub-QNL.

squeezed state $\Phi = 0.87$ (blue crosses) and the unsqueezed state $\Phi = 1$ (orange crosses) to the CRB defined by Eq (4.11). We observe that for the range of transmission from $\eta = 0.95$ to $\eta = 0.985$, on average the data points for the squeezed state are closer to the QNL than for the unsqueezed state. The noise reduction from the squeezed state improves the performance of the microscope for the range of transmission from $\eta = 0.95$ to $\eta = 0.985$. The results on a single pixel shown in Fig. 4.8(b) are similar to the one reported here for the imaging measurements. Higher squeezing can achieve better performance, and we can expect from the single pixel measurements that with $\Phi_{log} < -1.2\ dB$ sub-QNL measurement for absorption microscope with Kerr-squeezing could be achieved.

The previous analyses were characterising $Var(\eta)$ for an acquisition time $t = 1\ \mu s$ by calculating it from 50 measurements. This analyses result to characterise the variance of the measurements for a time scale of 50 μs. Fig. 4.10 shows the same measurements from Fig 4.9(d) but by evaluating the variance over a different time scale τ. For instance, for $\tau = 100\ \mu s$ the variance is calculated for 100 independent measurements, where each of them have an acquisition time of 1 μs. From this analysis, we observe that when τ increases, the variances of the estimate for a transmission $\eta < 97.5$ % are degraded. We observe that this degradation occurs for both of the unsqueezed and squeezed state and we can believe that the cause is the excess classical noise within the experiment. The classical noise within the measurement seems to be not stationary and for a higher time scale the classical noise dominates the quantum noise, degrading the variance of the estimates. For single pixel measurement, this is not a problem and it can be solved by taking fast measurement, as it has been done previously. For raster-scan imaging this drift within the measurements occurring for a time scale $\tau > 100\ \mu s$ are degrading the performance of the microscope. Due to the fact that the classical noise is not stationary, the second one of a pair of independent measurements with a RBW of 1 MHz will be biased if a longer time than $t > 100\ \mu s$ passed between the two measurements. Hence, with no correction, assuming that the two pixels have the exact same transmission, the measurements will show two pixels with different values and non-overlapping error bars. Referring to the definition of accuracy and precision from the section 2.3, we have a microscope which can provide an image with a high precision if the measurements are taken with an acquisition time $t = 1\ \mu s$ (given by the RBW), but for each pixel measured over a time scale $\tau > 100\ \mu s$ a bias is added, resulting in low accuracy. A synchronisation between the SA and the translation stages could enhance the total acquisition time of the raster-scan imaging, and in section 4.6, solutions are discussed to solve this problem of accuracy for absorption microscopy using this strategy of measurement.

4.6 Future work

We have demonstrated a precision enhancement for a squeezed state compared to an unsqueezed state. We observed that for a time scale $\tau = 100\ \mu s$, the variance of the measurements are not degraded due to classical noise occurring for a higher time scale for pixels with a transmission lower than 98 %. In this section is discussed future improvements on the microscope to ensure measurements with a high precision and accuracy between each pixel.

Fig. 4.11 shows two proposals to realise confocal microscopy by correcting the bias reported from section 4.5.3. We know that classical noise causes a drift within the measurements and affects the accuracy of the microscope occurs for $\tau > 100\ \mu s$. Therefore, the first proposal consists of measuring a vertical sweep over several pixels with the same transmission of $\eta \leq 0.98$. These pixels are measured with values of t and τ for which the variance of the estimates is not degraded and are inferred from the analyses of the section 4.5.2 and 4.5.3. Then, horizontal sweeps within $\tau < 100\ \mu s$ can map the sample for absorption imaging. The reference sweep is used to correct the bias between each horizontal sweeps. The correction can be done by comparing the common pixel between the reference sweep and the horizontal sweep (red pixel). The difference between these two values corresponds to the bias added by the classical noise. Then, knowing the bias, every pixel of the horizontal sweep can be corrected. Because all sweeps are taken within a time $\tau < 100\ \mu s$, corresponding to a time where the variance is not degraded, this strategy of

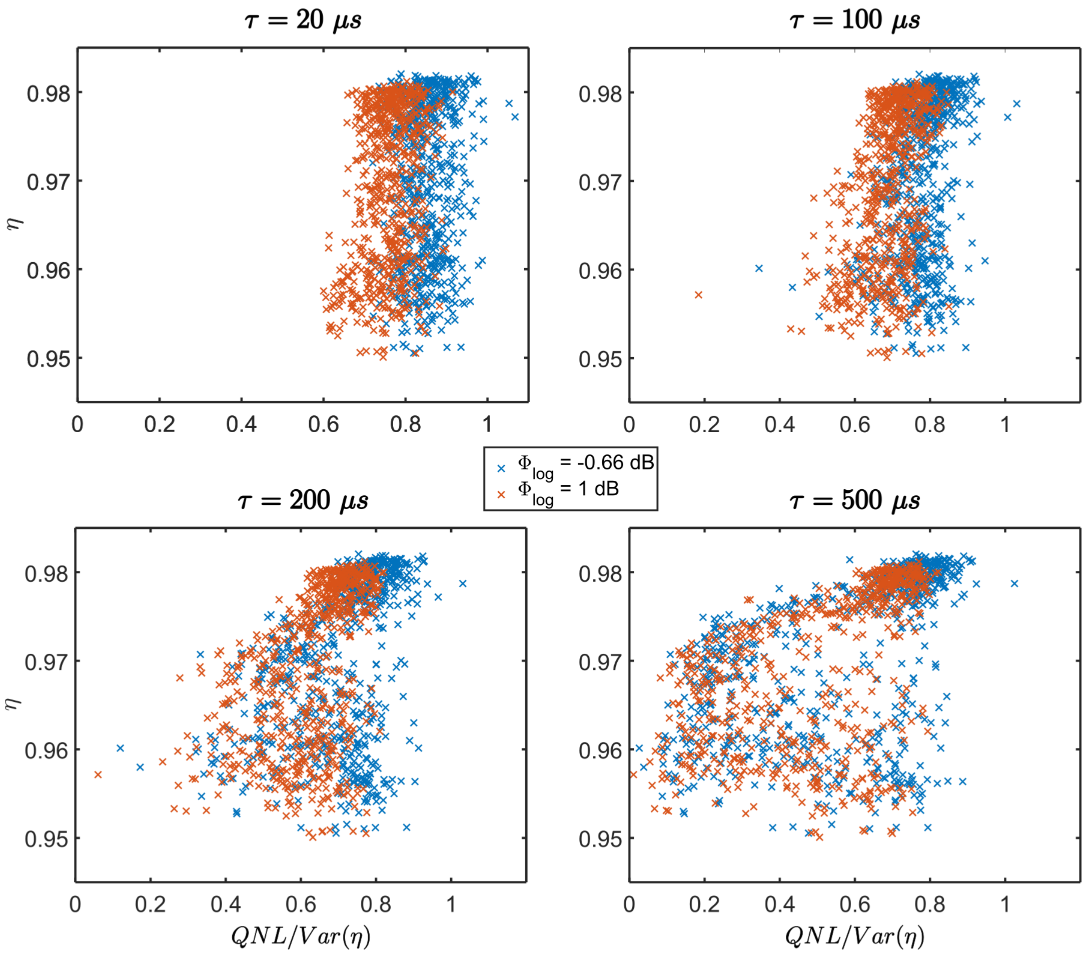

FIGURE 4.10. **Variances of the imaging for different time scale.** Same analysis from Fig. 4.9(d) but for different time scale. 20 μs top left, 100 μs top right, 200 μs bottom left and 500 μs bottom right. The blue and orange crosses correspond respectively for measurement with an amplitude squeezed state $\Phi = -0.66\ dB$ and for measurement with an unsqueezed state $\Phi = 1$.

measurement could provide a correction of the bias added to the measurements. The difficulty of such a strategy of measurement is to synchronise the SA with the translation stages. The speed of the translation stage is not a problem, because the reference sweep can be taken within $\tau = 0.1\ ms$ and does not need to be the full length of the sample. Therefore up to 100 pixels can be measured within this time and be used as a reference. This technique would provide a microscope with high precision and accuracy for contrast imaging. However even if every pixel is measured with high precision and accuracy, the bias is still present and the absolute value of the transmission coefficient for every pixel will be biased toward the reference sweep. This bias can be averaged and measured over several imaging measurement using different reference sweep.

The second proposal consists of monitoring the classical noise from the electro-optic modulator (EOM) to subtract it to the measurements. The experimental setup consists of a laser where the

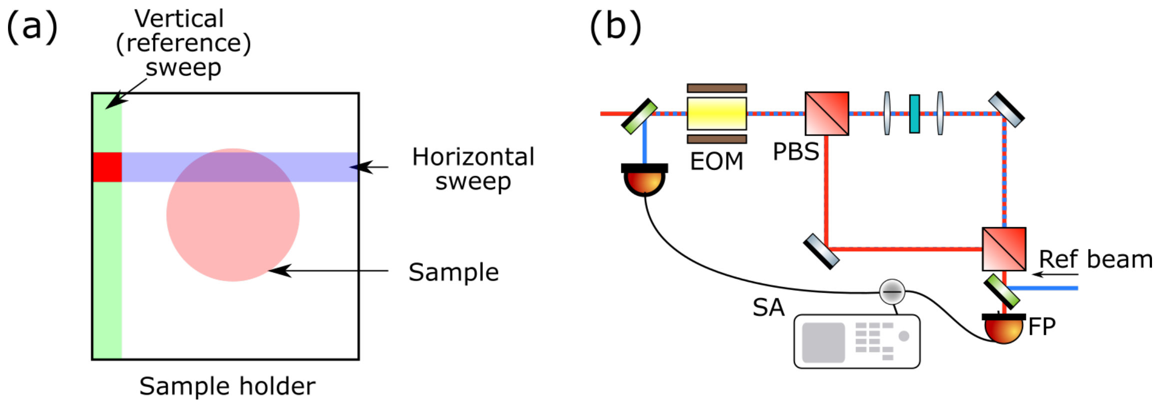

FIGURE 4.11. **Proposal for raster-scanning imaging.** (a) Fast-raster scanning imaging using a reference sampling. Each horizontal sweep mapping the sample shares one or more pixels with the reference sweep to correct the bias occurring between each horizontal sweep mapping the sample. (b) Noise from the EOM is probed simultaneously with the measurements and then is subtracted to the measurements.

probe beam is manipulated from the EOM. The classical noise can either come from external source and require stabilisation or from the devices manipulating the probe beam: here the laser (for the generation) and the EOM for the manipulation. Whereas quantum noise can not be copied, classical noise can. A reference laser is back propagating within the EOM as shown in Fig. 4.11(b). To avoid losses on the probe beam and decreasing the squeezing value, the reference beam needs to be at a different wavelength. Therefore, the reference beam can be extracted with a dichroic mirror, without causing massive losses to the squeezed state. This strategy assumes that excess noise is from the devices within the experiment. Both of these strategies could work together and could provide an accurate and precise microscope for contrast imaging.

A third solution would be to work with multi-mode probe beam. Multi-mode imaging with photon counting have demonstrated sub-shot noise measurements [126]. This strategy of measurement would be very expensive as it would require photodiodes for each pixel of the image. However, the electric signal could be monitored and then analysed post-imaging. This would solve the problem by monitoring each pixel within the desired RBW in a single shot. However, the photodiodes would need to have the same efficiency and same gain, to avoid any problem in the estimation of the transmission η.

Finally, the estimates of N and δ_m discussed in section 4.3 are subject to noise. Power fluctuations from the laser are monitored with a calibrated photodiode at the input of the experiment. The reported precision from the manufacturer (Thorlabs) is $\pm 3\%$. Furthermore, the modulation depth δ_m is measured once before the measurements on the sample and assumes to be constant. If these two values fluctuates over a time scale $\tau >> 1\ \mu s$, then with a RBW of

1 MHz these fluctuations are neglected. However for raster-scan imaging occurring for longer period of time, the instabilities of δ_m and the number of photon N can degrade the performance of the microscope. Monitoring these parameter during the raster-scan imaging with a higher precision could improve the accuracy of the microscope.

4.7 Conclusion

In this chapter, absorption microscopy has been demonstrated with a single-mode Kerr-squeezed state and shows an enhancement in the precision of the estimates compares to an unsqueezed state. The advantage is achieved by encoding a static loss measurement to a higher frequency bandwidth by modulating the phase of the probe beam in time between two orthogonal polarisation modes. This allows to work in a shot-noise limited bandwidth of the detectors and the laser and see an advantage of the noise reduction granted by a squeezed state within the measurements.

The experimental results shown in Fig. 4.8(b) demonstrate that an amplitude squeezed light enhances the precision of the estimates. For the unsqueezed state ($\Phi = 1$), we observe that due to the excess noise of the apparatus the measurements do not saturate the CRB. However, with the same apparatus, for a squeezing value of $\Phi_{log} = -0.88\ dB$ the measurement saturates the CRB of a coherent state. It means that the noise reduction from the squeezed state balances out the inherent noise of the apparatus. Following the trend of the theoretical fitting with a R-square of 99.2 %, sub-shot noise measurement on a single pixel with the same experimental protocol can be achieved with $\Phi_{log} < -1.2\ dB$. Further improvements in the alignment, and reducing the noise within the experiment of $\sim 10\%$ will help to achieve such a performance (note that $\Phi_{log} = -1.6\ dB$ has been achieved in a previous measurement). By using a bulk fast output detector, the signal would not need to be coupled to a multimode fibre and this would prevent 8 % of loss due to the coupling efficiency within the fibre.

After single-pixel estimation, a quantum advantage of 1.14 ± 0.1 has been experimentally demonstrated for absorption imaging for pixel with a transmission from 95 % to 98 %. However, when the time scale τ of the analysis increases (*i.e.* the variance over a longer period of time is calculated), the precision of the measurements is degraded for pixel with a transmission $\eta < 98\ \%$. Classical noise on the experimental setup occurs for a larger time scale and adds extra noise to the measurement for which the noise reduction from the squeezed state was not sufficient to balance it out. For raster-scan imaging when two pixels are measured with a RBW of 1 MHz and a time $\tau > 100\ \mu s$ passed between these two measurements, the excess noise can be seen as a bias added between the two measurements. The origin of the noise has not been investigated and is uncertain, however classical noise might be the cause. To correct the bias caused by this excess noise, three proposals have been suggested. One can monitor the classical noise with a sample beam back propagating within the EOM and subtract it to the signal beam with balanced photodiodes. This corresponds to homodyne detection where the classical noise is simultaneously monitored with the measurements and have already demonstrated improvement in the noise reduction [69]. The second proposal suggests to work with a reference sweep measuring pixels of a known transmission coefficient (such as the sample holder). Then, by processing the raster-scan on horizontal sweep, the sample is squared and the pixels in common between the reference sweep and the horizontal sweeps can be use to correct the bias and normalise the measurements. Both of these strategies could work together and could improve the performances of the microscope. The last proposal suggests multi-mode imaging, which has been demonstrated in a photon counting experiment [126]. The advantage of such a measurement is to monitor each pixel of the sample simultaneously, therefore the accumulated noise between each pixel can be reduced and sub-shot-noise performance can be demonstrated with a quantum probe. The problem is that such a measurement technique is limited by the devices acquiring the data, demanding high number of photodiodes (one for each pixel) working with the same efficiency and gain.

For the microscope discussed in this chapter, an analysis of $\mathscr{F}$ has highlighted the presence of noise from the DC components of the laser and the electro-optic modulator in section 4.3. By increasing the noise reduction with the amplitude squeezed light, the noise within the measurements decreased inducing an improvement in the variance of the estimates. The noise is inherent to the laser. However, demonstrations with homodyne detection have shown in the past that the noise within the signal can be subtracted and reach quantum-noise limited (QNL) measurements [69]. Using homodyne detection to suppress classical noise could be applied to improve the measurements in chapter 4. The inherent noise within the apparatus might be the cause of drifts within the measurements. For raster-scan imaging from section 4.5.3, each pixel of the sample is measured in a short period of time with a resolution bandwidth of 1 MHz, corresponding to an acquisition time of 1 μs. The variance of the estimated transmission η is calculated for a block of 50 measurements, corresponding to a period of time of 50 μs. It has been experimentally demonstrated that when the variance is calculated for measurements occurring for a period of time $\tau < 100$ μs, the amplitude squeezed state shows precision enhancement compared to an unsqueezed state (section 4.5.2 and 4.5.3). However, it has been experimentally demonstrated in section 4.5.3 that for a longer period $\tau > 100$ μs, the calculated variance of the estimates decreased both for the amplitude squeezed and unsqueezed state. The deterioration of the calculated variance for longer period of time corresponds to a a drift for raster-scan imaging. The inherent classical noise within the apparatus is not stationary and might be the cause of the drift. This drift causes a problem for raster-scan imaging, because even if each pixel are measured with a RBW of 1 MHz, if two pixels with the same transmission are measured over a period of time $\tau > 100$ μs, the measured value will be different, with error bars included. From these observations we conclude that quantum imaging schemes benefit from classical techniques to remove the excess classical noise within the apparatus, whilst the probe state of light is being enhanced with a quantum effect to improve the performance of measurements beyond the QNL.

Finally, comparing to photon-counting experiments, the brightness of the probe beam toward the sample from this microscope has been monitored to be 150 μW, whereas photon-counting experiments have been demonstrated in the fW regime [124]. The bright Kerr-squeezing microscope can provide absorption microscopy at a higher regime, where sub-shot noise performance could be achieved for a noise reduction $\Phi < -1.2\ dB$ with the same apparatus described in this chapter. Moreover, squeezed states of light could be use for gas sensing, where a similar protocol with squeezed state and frequency modulation have shown improvement in the signal-to-noise ratio for gas sensing [18]. This results in increasing the brightness of the probe, approaching the illumination of classical imaging technique with quantum enhancement [114, 128], and where the precision of the measurements from photon counting experiments is improved by increasing the brightness of the probe beam for a level of illumination where photo-damage and photo-toxicity can be avoided [58].

CHAPTER 5

CONCLUSION

We have seen two different quantum probe states of light for quantum microscopy. In chapter 3, two-photon interference known as the Hong-Ou-Mandel effect is used to measure a time delay between two photons, from the same photon pair. By transmitting one photon through a semi-transparent sample, the variation in thickness is measured and combined with a two-dimensional raster-scanning technique. The sensitivity of the microscope can be tuned by the use of a wavelength-entangled photon pair source and sub-fs precision (equivalent to sub-μm) is reported with ~ 10^4 photon pairs detected and 12.3 nm of wavelength separation between the signal and the idler. This provides quantum microscopy on the order of fW level, corresponding to 10^{-8} $W.cm^{-2}$ of sample illumination. The sample illumination from the HOM microscope is 8 to 12 order of magnitude below actual microscopes using classical light microscopy [114, 128]. Further improvements to the source could allow for simultaneous generation of HOM interferences exhibiting different frequency of the beat note. As discussed in the section 3.7, with a photon pair source generating broader downconverted photons, HOM interference exhibiting different frequencies of the beat note could be monitored. A wavelength-division multiplexer at the output of the HOM interferometer can help to measure HOM interferences simultaneously with different frequencies of the beat note, dependant on the frequency separation of the selected frequency channels [138]. This strategy of measurements would provide depth imaging with HOM interferences without fringe ambiguity whilst the Fisher information could be maximised in a single shot measurement. It has been discussed that further improvements could be made to the photon pair source to generate wavelength-entangled states with higher detuning. Whilst Lyons et al. achieved nanometre scale for a total acquisition time from 1.4 to 15.6 hours (Fig. 4 of [99]), increasing the Fisher information with higher detuning and a brighter photon pair source could lead similar resolution with a shorter acquisition time. With such a photon pair source, raster-scan depth imaging as presented in the section 3.6 could achieved nm axial precision. Nanometre scale for depth imaging in the order of picowatt intensity in the probe source could benefit microscopy applied to photo sensitive biological samples.

In chapter 4, we have seen precision enhancement with Kerr squeezing for absorption microscopy. The classical noise (such as electronic noise) occurring at low-frequency bandwidth is mitigated by conducting static-loss measurements within a shot-noise limited bandwidth at a higher frequency range. To implement such measurements, the probe beam undergoes path modulation through the use of an electro-optic modulator (EOM) and a polarising beamsplitter (PBS). Subsequently, the PBS split the horizontal and vertical polarisation modes with a pi-shit, these two polarisation modes are recombined with a second PBS. Since the sample interacts with only one of the modes, the loss induced by the sample results in an output beam with a modulation depth proportional to the loss. To achieve static-loss absorption with this experimental setup, it is simply necessary to measure the modulation depth or the signal-to-noise ratio using a spectral analyser at the sideband frequency. Finally, the quantum advantage of this microscope stems from the noise reduction provided by the squeezed state. To generate the squeezed state, a coherent state is launched in an unbalanced Sagnac non-linear interferometer to generate amplitude-squeezed state from Kerr-effect [129]. It has been demonstrated a noise reduction of the amplitude Kerr-squeezed state after transmitting through it a sample exhibiting a transmission $\eta \geq 94\%$. This enhances the precision where shot-noise measurements have been reported for single pixel sensing with a level of squeezing $\Phi_{log} = -0.88\ dB$. Furthermore, precision enhancement of 1.14 ± 0.1 between an unsqueezed state and a squeezed state with $\Phi_{log} = -0.66\ dB$ has been reported for absorption microscopy. With a Fisher information analysis, it has been demonstrated that sub-shot noise measurements can be possible for $\Phi_{log} < -1.2\ dB$, where values of $\Phi_{log} = -1.6\ dB$ has been initially reported for the source used in the chapter 4. Finally, due to the high precision of the microscope, bias in the measurements becomes more evident for absorption imaging. To correct the bias, three solutions are proposed. The first idea is to monitor the classical noise from a reference beam back-propagating within the electro-optic modulator and subtract the measured photocurrent to the sample beam [69]. The second idea proposes to correct the bias with a reference sweep. The horizontal sweep (or reference sweep) is taken in a period of time for which no drift has been experimentally reported. This sweep measures the transmission for several pixel aligned on a column. The transmission of these pixels need to be the same and can be use as a reference sweep. Afterwards, consecutive vertical sweeps with the same acquisition time than the reference sweep can be done to reconstruct an image of the sample. Each of the vertical sweeps share their first measured pixel with at least one pixel of the horizontal sweep. Therefore, the bias occurring between each vertical sweep can be corrected from the reference sweep, where no bias occurred during the measurements of the reference sweep. The last proposal is to work with a spatial multi-mode probe beam, which has demonstrated sub-shot noise imaging in a photon counting experiment [26, 126]. The spatial multi-mode probe beam could allow measurements of the whole sample in a short period of time where no drift within the measurements occur. Each pixel of the sample would be monitored by an individual photodiode, and then the measured photocurrent could be analysed after the data acquisition. This would require photodiodes with the same efficiency and the same response toward the probe beam. These proposals could remove the excess noise in the apparatus causing a degradation of the precision for a longer time scale and provide sub-shot noise measurements for absorption microscopy for bright amplitude squeezed probes. This could provide quantum enhanced precision for absorption microscopy, where the brightness of the probe light ($\sim 200\ \mu W$) achieves an illumination sample of 200 $W.cm^{-2}$ for confocal microscopy. However, due to the fast acquisition time of 1 MHz, photo-bleaching and photo-damage within the sample could be avoided due to the short time the sample is exposed to the probe light.

The estimators in chapter 3 and chapter 4 used to infer either the thickness or the transmission of the sample were shown to be optimal by saturating the Cramér-Rao bound (CRB). A Fisher information ($\mathscr{F}$) analysis has been used for both chapters 3 & 4. $\mathscr{F}$ only considers a given strategy of measurements without considering external noise. At times, implementing all the external noise within the theoretical framework can be challenging. For example, we observed that as the oven temperature approached a high level (approximately 120°C), the standard deviation in measurement precision increased. This phenomenon could be attributed to instabilities in the phase-locking mechanism caused by fluctuations in the refractive index and, consequently, the optical length of the interferometer. These fluctuations introduce errors in the phase-locking of the photon pair source, affecting the overall phase stability of the HOM interference. However, both of the Fisher information analyses from chapters 3 & 4 have exhibited a deviation of the measured precision from the CRB whilst the theoretical $\mathscr{F}$ was increasing. The most likely cause is excess noise within the apparatus. For the HOM microscope, the photon pair source was actively phase-locked. $\mathscr{F}$ was increased by controlling the temperature of the non-linear crystal causing a change in the refractive index. The phase-matching condition was changed from a modification of the refractive index, and the wavelength separation between the downconverted photons could be controlled. When the wavelength separation was increasing, the HOM interference was exhibiting a higher frequency of a beat note. It has been shown theoretically in section 3.3.3 and experimentally in section 3.6.6 that the measured $\mathscr{F}$ (*i.e* the precision of the measurements) was increasing whilst the frequency of the beat note was increasing too. However, the relative error on the measured precision reported in section 3.6.6 was increasing for higher value of the theoretical $\mathscr{F}$. The most likely cause was excess noise from the phase-locking. Indeed, when the refractive index of the crystal was changing due to the variation of the temperature, a path-deviation might have resulted on the laser back propagating within the source to phase-lock it. Hence, the visibility of the interference from the back propagating laser might have been degraded, inducing unstable phase-locking. Furthermore, it has been shown that toward the end of the experiment, the laser used to phase-lock the source became unstable causing mode hopping and abrupt jumps of the phase. The quality of the measurements were degraded as a result of this mode hopping. One proposed solution to this problem was to work with a photon pair source that does not need phase-locking, such as a cross-crystal configuration from [35] or an on-chip photon pair source [138]. These could provide higher stability in the generation of the state, and a possibility to increase the precision for higher theoretical value of $\mathscr{F}(t)$.

High precision for photo-sensitive samples such as molecules where photo-bleaching decreases the performance of imaging [45, 47] or photo-toxicity which damages the sample irreversibly [150] could be possible with a new generation of quantum microscope. The quantum advantage of the first microscope that we report in chapter 3 would be to take advantage of a quantum interference to reach higher Fisher information in estimating a sample's refractive index profile as a function of x-y position, per photon, where the illumination of the sample is ~ 8 order of magnitude below classical microscopes with super resolution [114, 128]. The second microscope, reported in chapter 4, exhibited a quantum probe brighter than a quantum microscope with photon counting experiments [26, 124, 126], however fast measurement decreases the sample illumination and could avoid photo-damage within the sample whilst a noise reduction from the amplitude squeezed state improves the precision of the measurements compared to an ideal classical state. This opens new capabilities of imaging, for refractive index imaging and absorption imaging, where quantum imaging can provide higher quality of information that classical imaging cannot reach. Either from quantum effects occurring at the single-photon level or from noise reduction from a quantum effect for a brighter probe beam.

APPENDIX A

APPENDIX

A.1 How to align a photon pair source.

For the two-photon pair sources presented in this thesis, the pump laser was coupled to a spatial single-mode fibre, as illustrated in Fig. A.1. This configuration offers two key advantages:

1. **Cleaning the spatial mode of the laser:** This makes it easier to achieve a high heralding efficiency when working with single spatial mode.

2. **Facilitating laser activation and deactivation:** When the laser is turned on and off, misalignment of the beam may occur. Additionally, bulk optics, such as mirrors, may experience slight movement due to mechanical relaxation. Therefore, it is more convenient to couple the light back into the single-mode fibre using two mirrors (one for translating the beam and one for tilting the angle of the beam) rather than realigning the entire photon pair source. This advantage holds true whether the laser needs to be shared with a colleague or if a laser replacement is necessary.

For a photon pair source using a non-linear crystal, knowing the crystal's characteristics is important. Here it generates collinear 808 nm downconverted photons with a pump wavelength centred at 404 nm and a crystal temperature of 32 $^{\circ}C$. In both photon pair sources presented in this thesis, *FiberPort collimators* from *Thorlabs* are employed as couplers. These collimators offer a great stability, great alignment into fibres but can be expensive and hard to handle for beginners. Screws at the back can tilt and change the focus spot of the beam, while the horizontal and vertical X-Y adjustments can be done with two screws on the horizontal and vertical edges of the coupler. Moreover, they are compatible with the translation mount *ST1XY-D/M* from *Thorlabs*, providing an additional degree of freedom for translating the beam on the X-Y plane.

The X-Y screws on the collimators can be utilised to tilt the beam while the screws at the back can be exclusively used to set the focus of the beam.

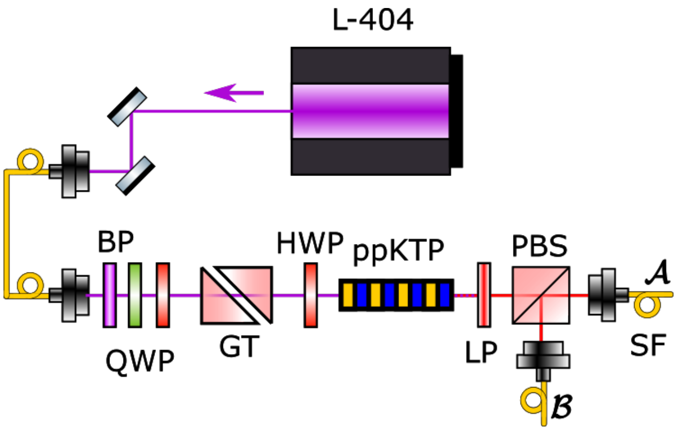

FIGURE A.1. **Alignment of a photon pair source.** The pump laser is coupled to a single spatial single-mode fibre to clean the spatial mode of the pump laser. Afterwards, the pump laser is transmitted toward the non-linear crystal in a similar way to Fig. 3.9

The alignment of the photon pair source is

The alignment of the photon pair source from chapter 3 is done following these steps:

1. Use two mirrors to guide the laser beam toward a fibre coupler, directly connected to a single-mode fibre. Connect the other end of the fibre to an alignment laser, and overlap the two laser beams at the fibre coupler's position and at the laser aperture. Achieve this alignment by walking off the beam, as demonstrated in Thorlabs' video available on YouTube: youtube: watch?v=qzxILY6nOmA. If the overlap of the two beams is sufficiently precise, this ensures effective laser coupling into the single-mode fibre. Finally, remove the alignment laser and use a powermeter. Increase the coupling efficiency by walking off the beam. For that, miss-align the laser with one mirror in one direction, and realign with the second mirror. Repeat this until the average power measured by the power meter does not increase anymore.
2. After that the laser is coupled Add a coupler to input the light into the photon pair source, and align it following a straight line.
3. Add the output $\mathscr{A}$ and $\mathscr{B}$, where the lenses, and the distances between the couplers and the crystal are calculated with GaussianBeam.
4. Overlap the beams from $\mathscr{A}$ and $\mathscr{B}$ to the input pump by walking-off the beam.
5. Add the ppKTP crystal, and align it by overlapping the input beam with the reflection on the edge of the crystal. The beam needs to be transmitted through the centre of the crystal.

6. Repeat step 4 if needed.
7. Connect $\mathscr{A}$ and $\mathscr{B}$ to single photon detectors, and do not forget to add longpass filters before the PBS to remove the excess pump.
8. Walk-off one of the downconverted couplers to increase the heralding efficiency.
9. On the other coupler, the translation mount can be use to increase the heralding efficiency without walking-off the beam.
10. Repeat the two previous steps to increase the heralding efficiency until the desirable brightness and heralding efficiency.

If the crystal is not collinear, it is important to know the angle of the downconverted photons and to use the screw holes of the optic table to place the couplers at the right angle toward the crystal.

A.2 Double Sagnac alignment

The two-colour entangled photon pair source in chapter 3 constitutes of a double Sagnac arrangement. A Sagnac arrangement (also called Sagnac interferometer, or Sagnac ring) is an experimental setup where the input beam is split into two different paths (here with a polarising beamsplitter PBS), and reflected back with mirrors for recombination on the original optical component splitting the light (as shown in Fig. A.2(a)). It is widely used nowadays for bulk alignment as the two directions of propagation of the light (clockwise and anti-clockwise) share commons mirrors. Therefore the environmental fluctuations on these mirrors will affect simultaneously the two directions of propagation, partially cancelling these perturbations and making the interferometer more robust to background noise.

Before aligning the source or any experiment, it is crucial to place all the optical components on the optical table without tightening them initially to ensure there is enough space for everything. A small Sagnac interferometer, while more robust, can be challenging to align. Therefore, it is recommended not to make it too large. For example, in the downconverted Sagnac (red in Fig. A.2(b)), the distance from M3 to M4 was approximately 15 cm to allow sufficient space for the 3 cm long crystal and the oven mounted on an alignment stage (*9081-M, MKS-Newport*).

To align the Sagnac interferometer shown on Fig. A.2(a), the following protocol is used:

1. The pump laser ($L-404$) is initially coupled to a single-mode fibre (see appendix A.1). Then, the lens at the tip of the fibre and the distance between the input pump and the crystal have been chosen with the help of GaussianBeam to ensure that the waist of the pump laser is located at the centre of the crystal (see appendix A.4). Two apertures (one close and one far away of the input beam) following the screw holes of the optical table in the diagonal direction have been used to align the anti-clockwise (AC) pump beam.

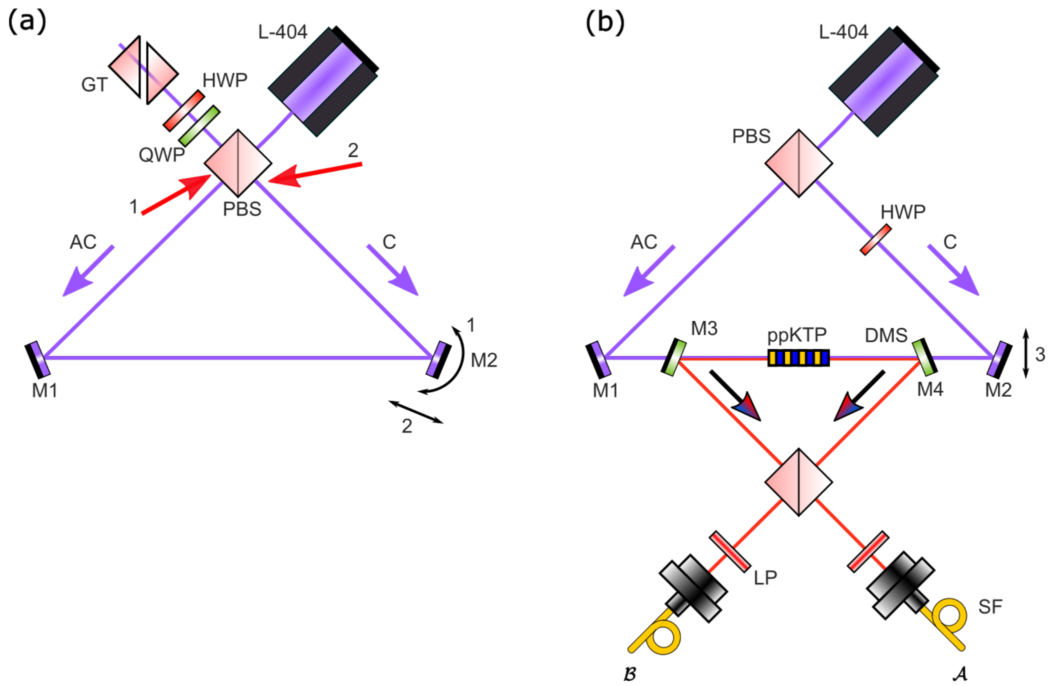

FIGURE A.2. **Sagnac interferometer and the two-colour entangled photon pairs source.** (a) Standard Sagnac interferometer where the input light is split into two directions by a polarising beamsplitter (PBS). The clockwise and anti-clockwise directions are reflected by mirrors (M) toward the PBS. (b) Two-colour entangled photon pair source constituted of two similar structures shown in (a).

2. The mirror (M1) is positioned and aligned to reflect the AC beam horizontally. Two apertures are employed to aid in the alignment process, aligning along the horizontal direction following the screw holes of the optic table.

3. The final mirror in the Sagnac interferometer, denoted as M2, is strategically positioned at the intersection point of the clockwise (C) and anti-clockwise (AC) directions of pumping. On Fig. A.2, the mirror's tilt, represented by a circular arrow labelled as 1, is adjusted to overlap the C and AC beams precisely at the location indicated by the red arrow 1. Simultaneously, the positioning of M2 along the direction of the black double arrow 2 is selected to align the two beams accurately at the designated red arrow 2. These two steps are iteratively carried out until the AC and C beams consistently coincide at the specified red arrows 1 and 2.

4. As depicted in Fig. A.2, a quarter-waveplate (QWP), half-waveplate (HWP) and a Glan-Taylor (GT) are added at the output of the interferometer. The visibility of the interference is assessed by measuring the maximum P_{max} and minimum P_{min} light intensities using a power meter after systematically rotating the waveplates. The visibility (V) is then

computed using the formula:

$$V = \frac{P_{max} - P_{min}}{P_{max} + P_{min}}. \tag{A.1}$$

To optimise visibility and reduce P_{min}, adjustments are made using the screws on mirrors M1 and M2, tilting them horizontally and vertically while ensuring the maintenance of the overlap at the two specified red arrows. The screws on both mirrors are rotated simultaneously but in opposite directions. Typically, following these three steps facilitates achieving a visibility of $V \geq 90$ %. To further enhance the system, tilting the mirrors to induce a walk-off on the beam is performed until a visibility of 98 % is attained. If the walk-off of the mirror proves insufficient, it often indicates a mispositioning of M2 along the black arrow 2. In such cases, adjustments are made to reposition M2 either closer or further away from the polarising beam splitter (PBS).

To align the photon pair source in Fig. A.2(b), the blue Sagnac is initially aligned using the steps outlined above. However, for aligning the photon pair source, I recommend mounting mirror M2 on a translation stage, moving it in the direction indicated by the black double arrow 3. Subsequently, the alignment of the photon pair source is carried out by following these steps:

1. Using a 808 nm alignment laser coupler on $\mathscr{A}$, the alignment of the red Sagnac is conducted following the previously described steps. The distance $M1 - M3$ needs to be equals to the distance $M2 - M4$.

2. After achieving a visibility ≥ 98.5% with the laser from $\mathscr{A}$, coupler $\mathscr{B}$ is introduced and overlapped with the beam from $\mathscr{A}$.

3. The ppKTP crystal is introduced and aligned such that the back-reflection on the crystal overlaps with the input light on both edges. It should be noted that the crystal may reflect the pump beam toward the bottom after it passes through it. To address this, longpass filters must be added before $\mathscr{A}$ and $\mathscr{B}$ to eliminate the excess pump.

4. Utilising the alignment screws on the couplers $\mathscr{A}$ and $\mathscr{B}$, photons pairs from the AC pumping are collected. The alignment is done by improving the Klyshko coefficient of each output.

5. Subsequently, adjustment of the position of $M2$ may be necessary using translation stage 3 and the alignment screws on the mirror mount. It is essential to note that while the blue Sagnac does not require perfect alignment for the source, excessive misalignment can pose challenges for the phase-locking of the source. Additionally, ensure the inclusion of the half-waveplate (HWP) on the C path to satisfy the phase-matching conditions.

6. Finally, the last two steps are repeated to improve the coupling efficiency from the both directions of pumping, with a Klyshko coefficient ∼ 20% in both directions of pumping.

A.3 SPDCalc: a rapid design tool for spontaneous parametric downconversion sources

SPDCalc.org is an online tool used in chapter 3 to calculate the efficiency and brightness of the source function of the pump and collection waists of the downconverted photons. For the photon pairs source in chapter 3, the length of the crystal is 3 cm, working at 32 $°C$ with a pump laser at 404 nm and a linewidth of 5 MHz. The wavelength of the downconverted photons is set to 808 nm. Fig. A.3 shows the calculated coincidence rates (a) and the single heralding efficiency (b) for different values of the pump waist and signal/idler (S/I) collection waists. The smaller the pump waist will be and the higher the coincidence rates is. It is because the local density of energy will be higher for a tight focus of the pump, increasing the probability to generate a photon pairs through the spontaneous parametric down conversion effect. The single heralding efficiency increases with the waists. The light beam will diverge less and due to the limited numerical aperture of the lenses, more light can be coupled into the fibre. However, having a bigger waist means decreasing the local density of energy for a same laser power. Subsequently, the probability to generate photon pairs via the SPDC process will decrease with a bigger waist. In chapter 3, the aim is to have a bright source since the rate of the photon pair source can influence the speed of imaging. If the rate of collected photon pairs is not sufficient, it may necessitate a long acquisition time. Consequently, I opted for a smaller waist to increase the brightness of the source, specifically the coincidence rates. However, having a small waist makes alignment more challenging and can result in reduced visibility, as discussed in section 3.4.2. Ultimately, the experimental achievement of the pump and collection waists of the signal and the idler involved determining the appropriate distance between the couplers and the crystal, as well as selecting the right lenses. All these parameters were calculated using GaussianBeam, as discussed in the appendix A.4.

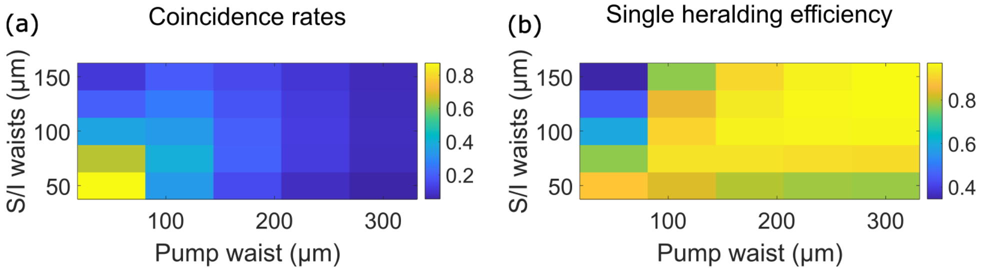

FIGURE A.3. **Coincidence rates and heralding efficiency calculated from SPDCalc.** (a) Fibre-coupled coincidence rates for different values of the pump waist and signal/idler (S/I) waists. (b) Single counts heralding efficiency for different values of the pump waist and signal/idler (S/I) waists. These are calculated from SPDCalc.

A.4 GaussianBeam

GaussianBeam is freely available software accessible on sourceforge.net. This tool is designed to calculate the propagation of a beam with a Gaussian profile, such as a laser beam. Additionally, it offers the capability to incorporate optical components, including lenses and other surfaces, which can modify the propagation of light.

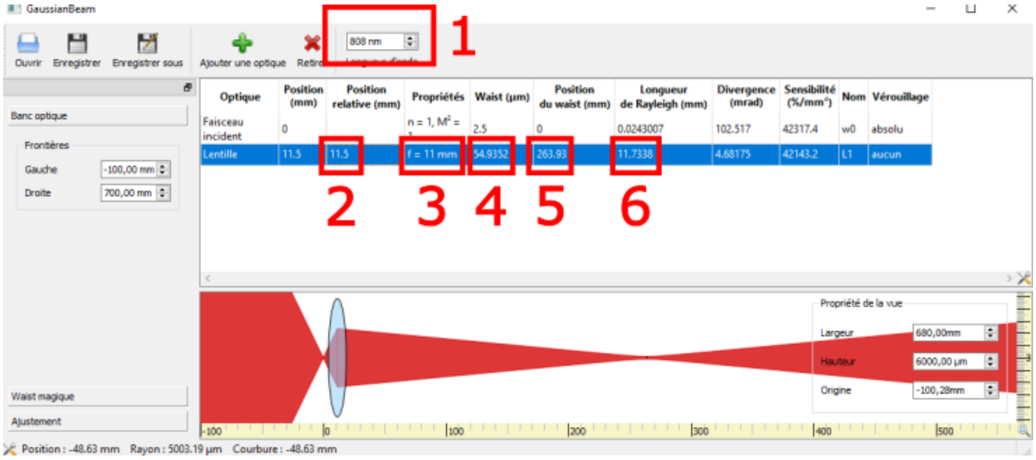

808 nm

Optique	Position (mm)	Position relative (mm)	Propriétés	Waist (µm)	Position du waist (mm)	Longueur de Rayleigh (mm)	Divergence (mrad)	Sensibilité (%/mm²)	Nom	Vérouillage
Faisceau incident	0		n = 1, M² =	2.5	0	0.0243007	102.517	42317.4	w0	absolu
Lentille	11.5	11.5	f = 11 mm	54.9352	263.93	11.7338	4.68175	42143.2	L1	aucun

Gauche -100,00 mm
Droite 700,00 mm

Largeur 680,00mm
Hauteur 6000,00 µm
Origine -100,28mm

Position : -48.63 mm Rayon : 5003.19 µm Courbure : -48.63 mm

FIGURE A.4. **Interface of the software GaussianBeam.** 1) Indicate the wavelength of the light, 2) relative position between the component (*e.g.* lens) and the incident beam, 3) focal length of the lens (or curvature for mirrors), 4) waist of the beam in μm (smallest radius), 5) position of the waist in mm to the origin and 6) Rayleigh length in mm.

Figure A.4 displays the interface of the GaussianBeam software. The red rectangles indicate various parameters, with some utilised by the software for calculations and others serving as essential guidance for selecting the appropriate lens in our experiment. Firstly, it's essential to specify the wavelength of the light (1) since dispersion is dependent on λ. In this example, we are considering the choice of lenses for downconverted photons in chapter 3, and thus set $\lambda = 808\ nm$. The fibres used to couple the light are from *Thorlabs*, with a mode field diameter of $5.0 \pm 0.5 \mu m$ at $850 nm$ (as indicated on the supplier's website). Consequently, the waist of the incident beam is set at $2.5 \mu m$, corresponding to the beam radius. Subsequently, the user specifies the focal length of the lens (3), taking note that some lenses are wavelength-dependent, for example, non-achromatic lenses. The position of the lens (2) is then chosen by the user. Finally, for different positions of the lens, parameters such as the waist (4), its position (5), and its Rayleigh range (6) are noted.

The Rayleigh range corresponds to the distance over which the waist is considered to be consistent. The smaller the Rayleigh range, the more challenging the alignment becomes. It is crucial to carefully consider the position of the lens, ensuring it is experimentally achievable with the selected coupler. Additionally, the distance must be chosen to provide ample space for all necessary optics within the experiment, situated between the downconverted couplers and the crystal. In this example, only the polarising beamsplitter and the longpass filter are included. However, the distance cannot be excessively long, as it would demand more space on the optic table. In the confocal microscope from chapter 3 and chapter 4, the distance between the lens and the focal point is significant and must be long enough to accommodate the sample adequately.

This tool provides a reliable approximation of the achievable waist with your current optics. That's why it has been employed in this thesis to assist in the selection of lenses.

A.5 How to find a Hong-Ou-Mandel interference?

The Hong-Ou-Mandel effect is identified by a reduction in coincident counts, known as anti-bunching, when the two photons of are indistinguishable. For degenerate HOM interference, it is recommended to operate with a single spatial mode, even though it is possible to conduct HOM interference with a spatial multi-mode source [106].

Fig. A.5 depicts a photography of the HOM interferometer utilised in chapter 3 excluding the confocal microscope and the 1 × 4 fused fibre couplers. The alignment of the HOM interferometer proceeds at it follows:

1. Before proceeding with any adjustments, arrange all optics on the table without tightening them to ensure sufficient space. Verify that the distance, denoted as $\mathscr{D}$, to the beamsplitter (BS) is equal to $\mathscr{C}$ - BS within the translation stage range.

2. Mount the translation stage dt with the coupler $\mathscr{C}$, and use a target or a beam profiler to confirm that the position of the beam remains stable during the translation of the stage.

3. Integrate the output coupler 2 into the setup and couple the light from $\mathscr{C}$ by adjusting the position of coupler 2 without making any other changes. To achieve this, the output couplers consist of two translation stages, enabling the translation of the beam within the horizontal or vertical direction. Additionally, an XY translation mount ($ST1XY-D$) facilitates tilting the beam by translating the lens adjacent to the output fibre.

4. Introduce the BS into the arrangement and confirm that the BS is positioned for optimal reflection efficiency. This may involve adjusting the angle between the BS and the incident beam from $\mathscr{C}$, typically aiming for an angle around $85-90°$.

5. Couple the light from $\mathscr{C}$ into 1, by only touching the coupler 1.

6. Incorporate the coupler $\mathscr{D}$ and couple the light into a single-mode fibre from the output coupler 1 by adjusting the position of coupler $\mathscr{D}$. Given that 1 and 2 are initially coupled to the same input coupler $\mathscr{C}$, coupling $\mathscr{D}$ to 1 should be sufficient and ensure good coupling efficiency from $\mathscr{D}$ to the output coupler 2. It's important to note that for HOM imaging,

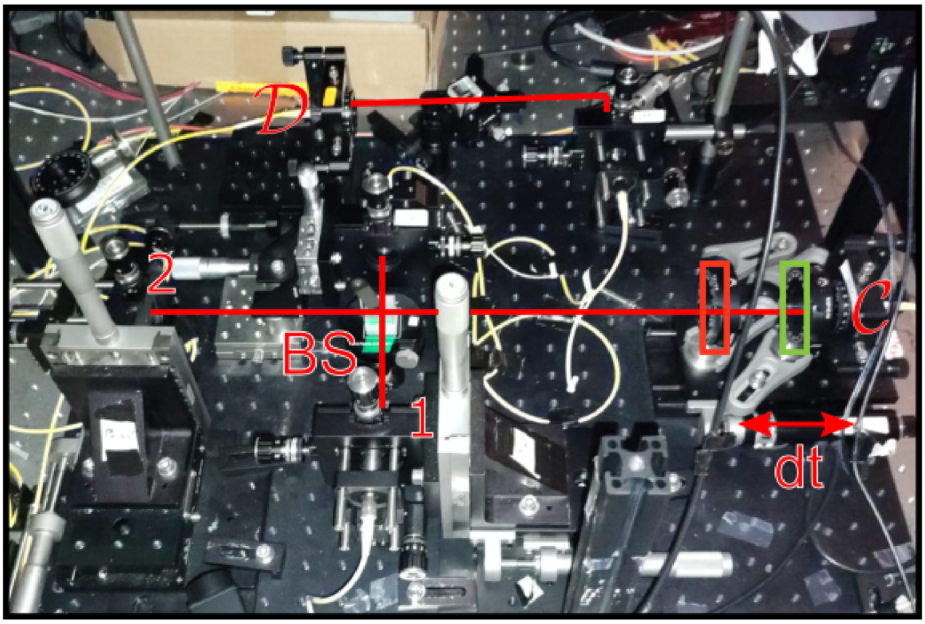

FIGURE A.5. **Hong-Ou-Mandel interferometer: alignment.** HOM interferometer from chapter 3 without the confocal microscope and the sample. BS: beamsplitter, $\mathscr{C}$ and $\mathscr{D}$ are the inputs of the photon pair source and dt corresponds to the translation stage. The red and green rectangles correspond respectively to half-waveplate and quarter-waveplate. 1 and 2 correspond to the two outputs of the interferometer.

the spatial mode should be filtered before the interference occurs (refer to Section 3.6.2). However, for casual HOM interferometry, this step is not necessary and can be omitted.

7. Add half and quarter waveplates in one of the input arm. It is recommended to add them on both inputs, as the polarisation matching of both input will be easier. Note: adding waveplates after finding the position of the HOM dip will shift it due to the thickness and the refractive index of the waveplates!

8. Connect the input fibres to the photon pair source, and repeat the previous alignment steps in order to increase the heralding efficiency and the number of detected photons.

9. Secure the input optical fibres on the optical table from $\mathscr{C}$ and $\mathscr{D}$ using tape. To ensure that the polarisation of each photon matches before interfering at the BS, add a polarising beamsplitter (PBS) before one of the output (*e.g.* 2). Rotates the HWP and QWP to decrease the number of detected single counts from $\mathscr{C}$ and then from $\mathscr{D}$. If you do not have waveplates in one of the arm, you can try to gently bend the fibre and then tape it to decrease the number of single counts. The polarisation matching can be improved later on. Remove the PBS initially positioned before one of the output.

10. Make sure that the downconverted photons are degenerate (*e.g.* with a spectrometer *Andor*), and check that both outputs 1 and 2 receive single photons from both inputs $\mathscr{C}$ and $\mathscr{D}$ by either blocking the input $\mathscr{C}$ or $\mathscr{D}$.

11. Monitor the number of coincidences while the stage translate toward the BS. You should find a dip. Position the translation stage at the dip and check that the number of anti-bunching coincidence counts vary by changing the polarisation of one input. If a dip is not found, make sure again that the two inputs before the BS have the same optical length within the translation of the stage in $\mathscr{C}$.

12. Increase the visibility of the interference after positioning the translation stage at the dip. Make sure to have degenerate photons, same spatial mode photons, and same polarisation.

If the HOM interference is still not found, make sure that the two inputs paths have the same length within the translation of the stage, and that each output receive single photons from both inputs.

A.6 Design of the fabricated sample

The design was made on Inkscape and converted to a GDS file to be visualised with Klayout. The masks were produced by *Compugraphics*, each measuring $0.8 \times 0.8\ cm^2$. The total active area is $7.3 \times 7.3\ cm^2$, corresponding to 36 masks to use for etching. It's important to note that each mask can be used only once for the etching process of the sample.

The design consists of three masks initially created for three different layers. Subsequently, only one mask was utilised, as depicted in Fig. A.6. The features at the top were too small to be manufactured, hence only the larger features at the bottom were employed for chapter 3. The four "L" shapes at the corners aided in aligning the masks on the glass sample, where the designed pattern was etched. The red rectangle corresponds to the "KET" imaged in chapter 3.

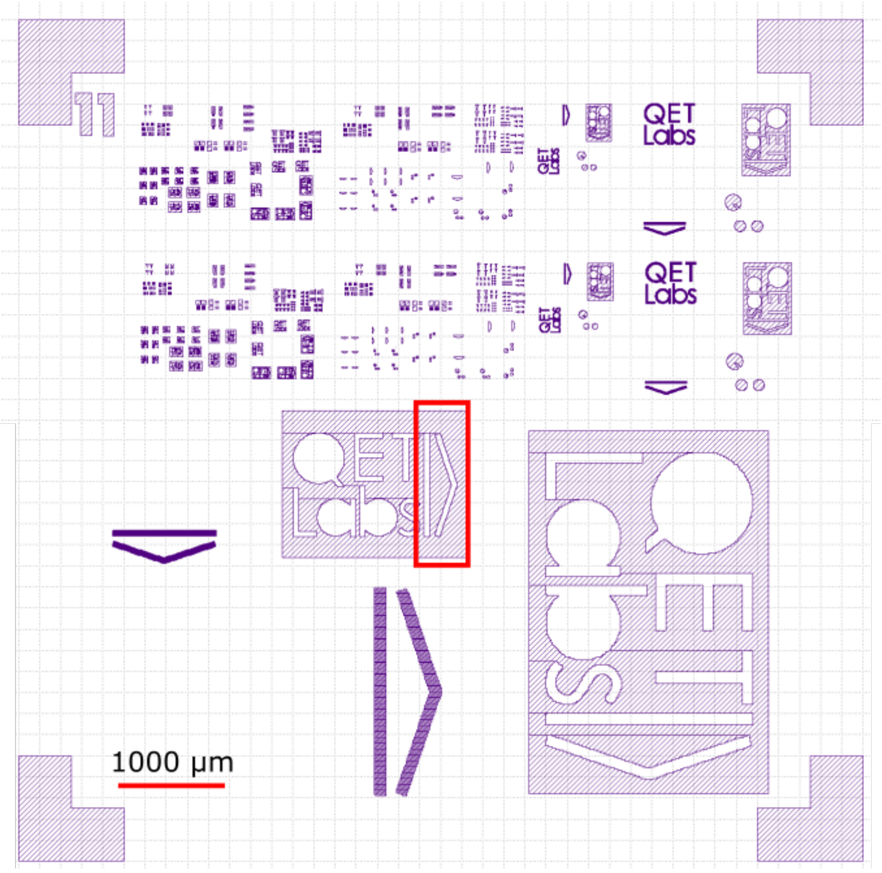

FIGURE A.6. **Design of the fabricated sample**. Screen shot of the mask, designed by myself on GDS for the fabricated sample. The red rectangle correspond to the "KET" imaged in chapter 3.

BIBLIOGRAPHY

[1] *Phase matching for nonlinear optical processes, https://www.fiberoptics4sale.com/*. https://shorturl.at/hivzD. Accessed: 2022-05-10.

[2] J. AASI AND ET AL., *Enhanced sensitivity of the LIGO gravitational wave detector by using squeezed states of light*, Nature Photonics, 7 (2013), pp. 613–619.

[3] G. ABBAS, V. CHAN, AND T. YEE, *A dual-detector optical heterodyne receiver for local oscillator noise suppression*, Journal of Lightwave Technology, 3 (1985), pp. 1110–1122.

[4] D. ACHILLES, C. SILBERHORN, C. SLIWA, K. BANASZEK, I. A. WALMSLEY, M. J. FITCH, B. C. JACOBS, T. B. PITTMAN, AND J. D. FRANSON, *Photon-number-resolving detection using time-multiplexing*, Journal of Modern Optics, 51 (2004), pp. 1499–1515.

[5] I. AFEK, O. AMBAR, AND Y. SILBERBERG, *High-NOON states by mixing quantum and classical light*, Science, 328 (2010), pp. 879–881.

[6] I. N. AGAFONOV, M. V. CHEKHOVA, AND G. LEUCHS, *Two-color bright squeezed vacuum*, Phys. Rev. A, 82 (2010), p. 011801.

[7] AGILENT TECHNOLOGIES, *Spectrum and signal analyzer: Measurements and noise*, Application Note, (2012), pp. 8–9.

[8] G. P. AGRAWAL, *Nonlinear fiber optics*, in Nonlinear Science at the Dawn of the 21st Century, Springer Berlin Heidelberg, 2000, pp. 195–211.

[9] U. L. ANDERSEN, T. GEHRING, C. MARQUARDT, AND G. LEUCHS, *30 years of squeezed light generation*, Physica Scripta, 91 (2016), p. 053001.

[10] U. L. ANDERSEN, J. S. NEERGAARD-NIELSEN, P. VAN LOOCK, AND A. FURUSAWA, *Hybrid discrete- and continuous-variable quantum information*, Nature Physics, 11 (2015), pp. 713–719.

[11] E. ARABUL, S. PAESANI, S. TANCOCK, J. RARITY, AND N. DAHNOUN, *A precise high count-rate FPGA based multi-channel coincidence counting system for quantum photonics applications*, IEEE Photonics Journal, 12 (2020), pp. 1–14.

[12] M. ATATÜRE, A. V. SERGIENKO, B. M. JOST, B. E. A. SALEH, AND M. C. TEICH, *Partial distinguishability in femtosecond optical spontaneous parametric down-conversion*, Phys. Rev. Lett., 83 (1999), pp. 1323–1326.

[13] G. ATKINSON, E. ALLEN, G. FERRANTI, A. MCMILLAN, AND J. MATTHEWS, *Quantum enhanced precision estimation of transmission with bright squeezed light*, Phys. Rev. Appl., 16 (2021), p. 044031.

[14] G. S. ATKINSON, *Quantum Metrology with Bright Squeezed Light*, PhD thesis, University of Bristol, 2021.

[15] H.-A. BACHOR AND T. C. RALPH, eds., *A Guide to Experiments in Quantum Optics*, Wiley, 2004.

[16] S. BARZ, I. KASSAL, M. RINGBAUER, Y. O. LIPP, B. DAKIĆ, A. ASPURU-GUZIK, AND P. WALTHER, *A two-qubit photonic quantum processor and its application to solving systems of linear equations*, Scientific Reports, 4 (2014).

[17] J. V. BECK AND K. J. ARNOLD, *Parameter estimation in engineering and science*, Wiley, 1977.

[18] A. BELSLEY, *Quantum-enhanced absorption spectroscopy with bright squeezed frequency combs*, Phys. Rev. Lett., 130 (2023), p. 133602.

[19] S. BOIXO, S. T. FLAMMIA, C. M. CAVES, AND J. GEREMIA, *Generalized limits for single-parameter quantum estimation*, Phys. Rev. Lett., 98 (2007), p. 090401.

[20] W. R. BOSENBERG AND C. L. TANG, *Type II phase matching in a β-barium borate optical parametric oscillator*, Applied Physics Letters, 56 (1990), pp. 1819–1821.

[21] R. W. BOYD, *Nonlinear Optics*, Academic Press, San Diego, CA, 3 ed., Mar. 2008.

[22] H. E. BRANDT, *Positive operator valued measure in quantum information processing*, American Journal of Physics, 67 (1999), pp. 434–439.

[23] S. L. BRAUNSTEIN AND C. M. CAVES, *Statistical distance and the geometry of quantum states*, Phys. Rev. Lett., 72 (1994), pp. 3439–3443.

[24] S. L. BRAUNSTEIN, C. M. CAVES, AND G. MILBURN, *Generalized uncertainty relations: Theory, examples, and lorentz invariance*, Annals of Physics, 247 (1996), pp. 135–173.

[25] S. L. BRAUNSTEIN AND P. VAN LOOCK, *Quantum information with continuous variables*, Rev. Mod. Phys., 77 (2005), pp. 513–577.

[26] G. BRIDA, M. GENOVESE, AND I. R. BERCHERA, *Experimental realization of sub-shot-noise quantum imaging*, Nature Photonics, 4 (2010), pp. 227–230.

[27] L. L. CAM, *The central limit theorem around 1935*, Statistical Science, 1 (1986).

[28] S. J. CARTER, P. D. DRUMMOND, M. D. REID, AND R. M. SHELBY, *Squeezing of quantum solitons*, Phys. Rev. Lett., 58 (1987), pp. 1841–1844.

[29] C. A. CASACIO, L. S. MADSEN, A. TERRASSON, M. WALEED, K. BARNSCHEIDT, B. HAGE, M. A. TAYLOR, AND W. P. BOWEN, *Quantum-enhanced nonlinear microscopy*, Nature, 594 (2021), pp. 201–206.

[30] G. CASELLA AND R. L. BERGER, *Statistical Inference*, Thomson Press, Nov. 2006.

[31] C. M. CAVES, *Quantum-mechanical noise in an interferometer*, Phys. Rev. D, 23 (1981), pp. 1693–1708.

[32] J. C. CHAPMAN, J. M. LUKENS, B. QI, R. C. POOSER, AND N. A. PETERS, *Bayesian homodyne and heterodyne tomography*, Optics Express, 30 (2022), p. 15184.

[33] H. CHEN, S. MA, X. WU, W. YANG, AND T. ZHAO, *Diagnose human colonic tissues by terahertz near-field imaging*, J. Biomed. Opt., 20 (2015), p. 036017.

[34] W. CHEN, J. COUSIN, E. POULLET, J. BURIE, D. BOUCHER, X. GAO, M. W. SIGRIST, AND F. K. TITTEL, *Continuous-wave mid-infrared laser sources based on difference frequency generation*, Comptes Rendus Physique, 8 (2007), pp. 1129–1150.

[35] Y. CHEN, M. FINK, F. STEINLECHNER, J. P. TORRES, AND R. URSIN, *Hong-Ou-Mandel interferometry on a biphoton beat note*, Npj Quantum Inf., 5 (2019).

[36] Y. CHEN, Q. SHEN, S. LUO, L. ZHANG, Z. CHEN, AND L. CHEN, *Entanglement-assisted absorption spectroscopy by Hong-Ou-Mandel interference*, Phys. Rev. Appl., 17 (2022), p. 014010.

[37] L. CHENG, W. BOSENBERG, AND C. TANG, *Growth and characterization of low temperature phase barium metaborate crystals*, Journal of Crystal Growth, 89 (1988), pp. 553–559.

[38] C. W. CHOW, C. H. YEH, Y. F. LIU, AND P. Y. HUANG, *Mitigation of optical background noise in light-emitting diode (led) optical wireless communication systems*, IEEE Photonics Journal, 5 (2013), pp. 7900307–7900307.

[39] M. CHRISTANDL AND R. RENNER, *Reliable quantum state tomography*, Phys. Rev. Lett., 109 (2012), p. 120403.

[40] C. COUTEAU, *Spontaneous parametric down-conversion*, Contemporary Physics, 59 (2018), pp. 291–304.

[41] C. Couteau, S. Barz, T. Durt, T. Gerrits, J. Huwer, R. Prevedel, J. Rarity, A. Shields, and G. Weihs, *Applications of single photons in quantum metrology, biology and the foundations of quantum physics*, Nature Reviews Physics, 5 (2023), pp. 354–363.

[42] H. Cramér, *Mathematical Methods of Statistics (PMS-9)*, Princeton University Press, 1999.

[43] D. M. Dagenais and F. Bucholtz, *Measurement and origin of magnetostrictive noise limitation in magnetic fiber-optic sensors*, Optics Letters, 19 (1994), p. 1699.

[44] C. Degen, F. Reinhard, and P. Cappellaro, *Quantum sensing*, Reviews of Modern Physics, 89 (2017).

[45] A. P. Demchenko, *Photobleaching of organic fluorophores: quantitative characterization, mechanisms, protection*, Methods and Applications in Fluorescence, 8 (2020), p. 022001.

[46] R. Demkowicz-Dobrzanski, U. Dorner, B. J. Smith, J. S. Lundeen, W. Wasilewski, K. Banaszek, and I. A. Walmsley, *Quantum phase estimation with lossy interferometers*, Phys. Rev. A, 80 (2009), p. 013825.

[47] D. Djukic and J. M. van Ruitenbeek, *Shot noise measurements on a single molecule*, Nano Letters, 6 (2006), pp. 789–793.

[48] V. G. Dmitriev, G. G. Gurzadyan, and D. N. Nikogosyan, *Handbook of Nonlinear Optical Crystals*, Springer Berlin Heidelberg, 1997.

[49] U. Dorner, R. Demkowicz-Dobrzanski, B. J. Smith, J. S. Lundeen, W. Wasilewski, K. Banaszek, and I. A. Walmsley, *Optimal quantum phase estimation*, Phys. Rev. Lett., 102 (2009), p. 040403.

[50] T. Eberle, S. Steinlechner, J. Bauchrowitz, V. Händchen, H. Vahlbruch, M. Mehmet, H. Müller-Ebhardt, and R. Schnabel, *Quantum enhancement of the zero-area sagnac interferometer topology for gravitational wave detection*, Phys. Rev. Lett., 104 (2010), p. 251102.

[51] M. D. Eisaman, J. Fan, A. Migdall, and S. V. Polyakov, *Invited review article: Single-photon sources and detectors*, Review of Scientific Instruments, 82 (2011), p. 071101.

[52] P. Eraerds, M. Legré, A. Rochas, H. Zbinden, and N. Gisin, *SiPM for fast photon-counting and multiphoton detection*, Optics Express, 15 (2007), p. 14539.

[53] B. M. Escher, R. L. de Matos Filho, and L. Davidovich, *General framework for estimating the ultimate precision limit in noisy quantum-enhanced metrology*, Nature Physics, 7 (2011), pp. 406–411.

[54] M. Evans, S. Ballmer, M. Fejer, P. Fritschel, G. Harry, and G. Ogin, *Thermo-optic noise in coated mirrors for high-precision optical measurements*, Phys. Rev. D, 78 (2008), p. 102003.

[55] A. Fedrizzi, T. Herbst, A. Poppe, T. Jennewein, and A. Zeilinger, *A wavelength-tunable fiber-coupled source of narrowband entangled photons*, Optics Express, 15 (2007), p. 15377.

[56] M. Fiorentino, S. M. Spillane, R. G. Beausoleil, T. D. Roberts, P. Battle, and M. W. Munro, *Spontaneous parametric down-conversion in periodically poled KTP waveguides and bulk crystals*, Optics Express, 15 (2007), p. 7479.

[57] R. A. Fisher, *A mathematical examination of the methods of determining the accuracy of observation by the mean error, and by the mean square error*, Monthly Notices of the Royal Astronomical Society, 80 (1920), pp. 758–770.

[58] R. Galli, O. Uckermann, E. F. Andresen, K. D. Geiger, E. Koch, G. Schackert, G. Steiner, and M. Kirsch, *Intrinsic indicator of photodamage during label-free multiphoton microscopy of cells and tissues*, PLoS ONE, 9 (2014), p. e110295.

[59] A. Galvanauskas, D. Harter, M. A. Arbore, M. H. Chou, and M. M. Fejer, *Chirped-pulse-amplification circuits for fiber amplifiers, based on chirped-period quasi-phase-matching gratings*, Opt. Lett., 23 (1998), pp. 1695–1697.

[60] Y. Gao, P. M. Anisimov, C. F. Wildfeuer, J. Luine, H. Lee, and J. P. Dowling, *Super-resolution at the shot-noise limit with coherent states and photon-number-resolving detectors*, Journal of the Optical Society of America B, 27 (2010), p. A170.

[61] N. R. Gemmell, J. Flórez, E. Pearce, O. Czerwinski, C. C. Phillips, R. F. Oulton, and A. S. Clark, *Loss-compensated and enhanced midinfrared interaction-free sensing with undetected photons*, Phys. Rev. Appl., 19 (2023), p. 054019.

[62] G. M. Gibson, S. D. Johnson, and M. J. Padgett, *Single-pixel imaging 12 years on: a review*, Optics Express, 28 (2020), p. 28190.

[63] V. Giovannetti, S. Lloyd, and L. Maccone, *Advances in quantum metrology*, Nature Photonics, 5 (2011), pp. 222–229.

[64] N. Gisin and R. Thew, *Quantum communication*, Nature Photonics, 1 (2007), pp. 165–171.

[65] G. N. Gol'tsman, O. Okunev, G. Chulkova, A. Lipatov, A. Semenov, K. Smirnov, B. Voronov, A. Dzardanov, C. Williams, and R. Sobolewski, *Picosecond superconducting single-photon optical detector*, Applied Physics Letters, 79 (2001), pp. 705–707.

[66] W. P. GRICE AND I. A. WALMSLEY, *Spectral information and distinguishability in type-II down-conversion with a broadband pump*, Phys. Rev. A, 56 (1997), pp. 1627–1634.

[67] N. HARNCHAIWAT, F. ZHU, N. WESTERBERG, E. GAUGER, AND J. LEACH, *Tracking the polarisation state of light via Hong-Ou-Mandel interferometry*, Opt. Express, 28 (2020), pp. 2210–2220.

[68] H. A. HAUS, *Electromagnetic Noise and Quantum Optical Measurements*, Springer Berlin Heidelberg, 2000.

[69] P. C. D. HOBBS, *REACHING THE SHOT NOISE LIMIT FOR $10*, Optics and Photonics News, 2 (1991), p. 17.

[70] H. F. HOFMANN AND S. TAKEUCHI, *Quantum phase gate for photonic qubits using only beam splitters and post selection*, Phys. Rev. A., 66 (2001), p. 024308.

[71] C. K. HONG AND L. MANDEL, *Theory of parametric frequency down conversion of light*, Phys. Rev. A, 31 (1985), pp. 2409–2418.

[72] C. K. HONG, Z. Y. OU, AND L. MANDEL, *Measurement of subpicosecond time intervals between two photons by interference*, Phys. Rev. Lett., 59 (1987), pp. 2044–2046.

[73] Y. HOSEONG, K. JANGSUN, AND A. YEONG HWAN, *High-speed THz time-of-flight imaging with reflective optics*, Sensors, 23 (2023).

[74] D. S. HUM AND M. M. FEJER, *Quasi-phasematching*, Comptes Rendus Physique, 8 (2007), pp. 180–198.

[75] S. D. HUVER, C. F. WILDFEUER, AND J. P. DOWLING, *Entangled fock states for robust quantum optical metrology, imaging, and sensing*, Phys. Rev. A, 78 (2008), p. 063828.

[76] T. S. ISKHAKOV, A. M. PÉREZ, K. Y. SPASIBKO, M. V. CHEKHOVA, AND G. LEUCHS, *Superbunched bright squeezed vacuum state*, Optics Letters, 37 (2012), p. 1919.

[77] Y. ISRAEL, S. ROSEN, AND Y. SILBERBERG, *Supersensitive polarization microscopy using noon states of light*, Phys. Rev. Lett., 112 (2014), p. 103604.

[78] M. A. JOHNSON AND M. H. MORADI, eds., *PID Control*, Springer-Verlag, 2005.

[79] S. JOHNSON, A. MCMILLAN, C. TORRE, S. FRICK, J. RARITY, AND M. PADGETT, *Single-pixel imaging with heralded single photons*, Optics Continuum, 1 (2022), p. 826.

[80] F. KAISER, P. VERGYRIS, D. AKTAS, C. BABIN, L. LABONTÉ, AND S. TANZILLI, *Quantum enhancement of accuracy and precision in optical interferometry*, Light: Science & Applications, 7 (2017), pp. 17163–17163.

[81] A. A. KALACHEV, D. A. KALASHNIKOV, A. A. KALINKIN, T. G. MITROFANOVA, A. V. SHKALIKOV, AND V. V. SAMARTSEV, *Biphoton spectroscopy of YAG:Er*$^{3+}$ *crystal*, Laser Physics Letters, 4 (2007), pp. 722–725.

[82] B. E. KARDYNAŁ, Z. L. YUAN, AND A. J. SHIELDS, *An avalanche-photodiode-based photon-number-resolving detector*, Nature Photonics, 2 (2008), pp. 425–428.

[83] S. M. KAY, *Fundamentals of statistical processing, volume I*, Prentice Hall, Philadelphia, PA, Mar. 1993.

[84] O. KHARRAZ AND D. FORSYTH, *Performance comparisons between PIN and APD photodetectors for use in optical communication systems*, Optik, 124 (2013), pp. 1493–1498.

[85] T. KIM, M. FIORENTINO, AND F. N. C. WONG, *Phase-stable source of polarization-entangled photons using a polarization sagnac interferometer*, Phys. Rev. A, 73 (2006), p. 012316.

[86] M. KITAGAWA AND Y. YAMAMOTO, *Number-phase minimum-uncertainty state with reduced number uncertainty in a Kerr nonlinear interferometer*, Phys. Rev. A, 34 (1986), pp. 3974–3988.

[87] D. N. KLYSHKO, *Use of two-photon light for absolute calibration of photoelectric detectors*, Sov. J. Quantum Electron., 10 (1980), pp. 1112–1117.

[88] X. KUANG, X. SUI, Y. LIU, Q. CHEN, AND G. GU, *Single infrared image optical noise removal using a deep convolutional neural network*, IEEE Photonics Journal, 10 (2018), pp. 1–15.

[89] P. KWEE, C. BOGAN, K. DANZMANN, M. FREDE, H. KIM, P. KING, J. PÖLD, O. PUNCKEN, R. L. SAVAGE, F. SEIFERT, P. WESSELS, L. WINKELMANN, AND B. WILLKE, *Stabilized high-power laser system for the gravitational wave detector advanced LIGO*, Optics Express, 20 (2012), p. 10617.

[90] P. KWEE, B. WILLKE, AND K. DANZMANN, *Shot-noise-limited laser power stabilization with a high-power photodiode array*, Optics Letters, 34 (2009), p. 2912.

[91] E. LEHMANN AND G. CASELLA, *Theory of Point Estimation*, Springer-Verlag, 1998.

[92] M. S. LEIFER AND R. W. SPEKKENS, *Towards a formulation of quantum theory as a causally neutral theory of bayesian inference*, Phys. Rev. A, 88 (2013), p. 052130.

[93] G. B. LEMOS, V. BORISH, G. D. COLE, S. RAMELOW, R. LAPKIEWICZ, AND A. ZEILINGER, *Quantum imaging with undetected photons*, Nature, 512 (2014), pp. 409–412.

[94] G. B. LEMOS, M. LAHIRI, S. RAMELOW, R. LAPKIEWICZ, AND W. N. PLICK, *Quantum imaging and metrology with undetected photons: tutorial*, J. Opt. Soc. Am. B, 39 (2022), pp. 2200–2228.

[95] R. LOUDON, *The quantum theory of light*, Oxford University Press, London, England, 3 ed., Sept. 2000.

[96] X.-M. LU, S. YU, AND C. H. OH, *Robust quantum metrological schemes based on protection of quantum fisher information*, Nature Communications, 6 (2015).

[97] A. I. LVOVSKY, *Squeezed light*, in Photonics, John Wiley & Sons, Inc., Jan. 2015, pp. 121–163.

[98] A. LY, M. MARSMAN, J. VERHAGEN, R. P. GRASMAN, AND E.-J. WAGENMAKERS, *A tutorial on fisher information*, Journal of Mathematical Psychology, 80 (2017), pp. 40–55.

[99] A. LYONS, G. C. KNEE, E. BOLDUC, T. ROGER, J. LEACH, E. M. GAUGER, AND D. FACCIO, *Attosecond-resolution Hong-Ou-Mandel interferometry*, Sci. Adv., 4 (2018), p. eaap9416.

[100] J. C. F. MATTHEWS, X.-Q. ZHOU, H. CABLE, P. J. SHADBOLT, D. J. SAUNDERS, G. A. DURKIN, G. J. PRYDE, AND J. L. O'BRIEN, *Towards practical quantum metrology with photon counting*, Npj Quantum Inf., 2 (2016).

[101] K. MCKENZIE, N. GROSSE, W. P. BOWEN, S. E. WHITCOMB, M. B. GRAY, D. E. MCCLELLAND, AND P. K. LAM, *Squeezing in the audio gravitational-wave detection band*, Phys. Rev. Lett., 93 (2004), p. 161105.

[102] A. MONRAS AND M. G. A. PARIS, *Optimal quantum estimation of loss in bosonic channels*, Phys. Rev. Lett., 98 (2007), p. 160401.

[103] P.-A. MOREAU, E. TONINELLI, T. GREGORY, AND M. J. PADGETT, *Imaging with quantum states of light*, Nature Reviews Physics, 1 (2019), pp. 367–380.

[104] G. MOUROU, *Extreme light physics and application*.
https://www.nobelprize.org/prizes/physics/2018/mourou/lecture/.

[105] J. D. MUELLER, N. SAMANTARAY, AND J. C. F. MATTHEWS, *A practical model of twin-beam experiments for sub-shot-noise absorption measurements*, Applied Physics Letters, 117 (2020), p. 034001.

[106] B. NDAGANO, H. DEFIENNE, D. BRANFORD, Y. D. SHAH, A. LYONS, N. WESTERBERG, E. N. GAUGER, AND D. FACCIO, *Quantum microscopy based on hong–ou–mandel interference*, Nat. Photon., 16 (2022), pp. 384–389.

[107] J. L. O'Brien, G. J. Pryde, A. G. White, T. C. Ralph, and D. Branning, *Demonstration of an all-optical quantum controlled-NOT gate*, Nature, 426 (2003), pp. 264–267.

[108] T. Ono, R. Okamoto, and S. Takeuchi, *An entanglement-enhanced microscope*, Nat. Commun., 4 (2013), pp. 1–7.

[109] Z. Y. Ou and L. Mandel, *Observation of spatial quantum beating with separated photodetectors*, Phys. Rev. Lett., 61 (1988), pp. 54–57.

[110] Z.-Y. J. Ou, *Multi-Photon Quantum Interference*, Springer New York, NY, 2007.

[111] A. M. Pérez, T. S. Iskhakov, P. Sharapova, S. Lemieux, O. V. Tikhonova, M. V. Chekhova, and G. Leuchs, *Bright squeezed-vacuum source with 1.1 spatial mode*, Optics Letters, 39 (2014), p. 2403.

[112] A. Peruzzo, A. Laing, A. Politi, T. Rudolph, and J. L. O'Brien, *Multimode quantum interference of photons in multiport integrated devices*, Nature Communications, 2 (2011).

[113] S. Pirandola, B. R. Bardhan, T. Gehring, C. Weedbrook, and S. Lloyd, *Advances in photonic quantum sensing*, Nature Photonics, 12 (2018), pp. 724–733.

[114] K. Prakash, B. Diederich, R. Heintzmann, and L. Schermelleh, *Super-resolution microscopy: a brief history and new avenues*, Philosophical Transactions of the Royal Society A: Mathematical, Physical and Engineering Sciences, 380 (2022).

[115] T. C. Ralph, N. K. Langford, T. B. Bell, and A. G. White, *Linear optical controlled-NOT gate in the coincidence basis*, Phys. Rev. A., 65 (2001), p. 062324.

[116] C. R. Rao, *Information and the accuracy attainable in the estimation of statistical parameters*, in Springer Series in Statistics, Springer New York, 1992, pp. 235–247.

[117] J. G. Rarity and P. R. Tapster, *Fourth-order interference in parametric downconversion*, J. Opt. Soc. Am. B, 6 (1989), pp. 1221–1226.

[118] J. G. Rarity and P. R. Tapster, *Two-color photons and nonlocality in fourth-order interference*, Phys. Rev. A, 41 (1990), pp. 5139–5146.

[119] C. Rauscher, *Fundamentals of spectrum analysis*, Rohde & Schwarz, Munich, Germany, 8 ed., Mar. 2007.

[120] M. Reisner, F. Mazeas, R. Dauliat, B. Leconte, D. Aktas, R. Cannon, P. Roy, R. Jamier, G. Sauder, F. Kaiser, S. Tanzilli, and L. Labonté, *Quantum-limited determination of refractive index difference by means of entanglement*, Npj Quantum Inf., 8 (2022).

[121] D. Romik, *Stirling's approximation for $n!$: the ultimate short proof?*, The American Mathematical Monthly, 107 (2000), pp. 556–557.

[122] M. Rosenbluh and R. M. Shelby, *Squeezed optical solitons*, Phys. Rev. Lett., 66 (1991), pp. 153–156.

[123] M. H. Rubin, D. N. Klyshko, Y. H. Shih, and A. V. Sergienko, *Theory of two-photon entanglement in type-II optical parametric down-conversion*, Phys. Rev. A, 50 (1994), pp. 5122–5133.

[124] J. Sabines-Chesterking, A. R. McMillan, P. A. Moreau, S. K. Joshi, S. Knauer, E. Johnston, J. G. Rarity, and J. C. F. Matthews, *Twin-beam sub-shot-noise raster-scanning microscope*, Optics Express, 27 (2019), p. 30810.

[125] J. Sabines-Chesterking, R. Whittaker, S. K. Joshi, P. M. Birchall, P. A. Moreau, A. McMillan, H. V. Cable, J. L. O'Brien, J. G. Rarity, and J. C. F. Matthews, *Sub-shot-noise transmission measurement enabled by active feed-forward of heralded single photons*, Phys. Rev. Appl., 8 (2017), p. 014016.

[126] N. Samantaray, I. Ruo-Berchera, A. Meda, and M. Genovese, *Realization of the first sub-shot-noise wide field microscope*, Light: Science & Applications, 6 (2017), pp. e17005–e17005.

[127] E. A. Santos, T. Pertsch, F. Setzpfandt, and S. Saravi, *Subdiffraction quantum imaging with undetected photons*, Phys. Rev. Lett., 128 (2022), p. 173601.

[128] L. Schermelleh, A. Ferrand, T. Huser, C. Eggeling, M. Sauer, O. Biehlmaier, and G. P. C. Drummen, *Super-resolution microscopy demystified*, Nature Cell Biology, 21 (2019), pp. 72–84.

[129] S. Schmitt, J. Ficker, M. Wolff, F. König, A. Sizmann, and G. Leuchs, *Photon-number squeezed solitons from an asymmetric fiber-optic sagnac interferometer*, Phys. Rev. Lett., 81 (1998), pp. 2446–2449.

[130] K. Schneider, R. Bruckmeier, H. Hansen, S. Schiller, and J. Mlynek, *Bright squeezed-light generation by a continuous-wave semimonolithic parametric amplifier*, Optics Letters, 21 (1996), p. 1396.

[131] B. L. Schumaker, *Noise in homodyne detection*, Optics Letters, 9 (1984), p. 189.

[132] A. D. Semenov, G. N. Gol'tsman, and A. A. Korneev, *Quantum detection by current carrying superconducting film*, Physica C: Superconductivity, 351 (2001), pp. 349–356.

[133] D. Sen, *The uncertainty relations in quantum mechanics*, CURRENT SCIENCE, 107 (2014).

[134] A. V. SERGIENKO, Y. H. SHIH, AND M. H. RUBIN, *Experimental evaluation of a two-photon wave packet in type-II parametric downconversion*, J. Opt. Soc. Am. B, 12 (1995), pp. 859–862.

[135] B.-S. SHI AND A. TOMITA, *Generation of a pulsed polarization entangled photon pair using a sagnac interferometer*, Phys. Rev. A, 69 (2004), p. 013803.

[136] S. SHIN, U. SHARMA, H. TU, W. JUNG, AND S. A. BOPPART, *Characterization and analysis of relative intensity noise in broadband optical sources for optical coherence tomography*, IEEE Photonics Technology Letters, 22 (2010), pp. 1057–1059.

[137] M. SHIRASAKI AND H. A. HAUS, *Squeezing of pulses in a nonlinear interferometer*, Journal of the Optical Society of America B, 7 (1990), p. 30.

[138] J. W. SILVERSTONE ET AL., *On-chip quantum interference between silicon photon-pair sources*, Nat. Photon., 8 (2014).

[139] A. SIZMANN AND G. LEUCHS, in The Optical Kerr Effect and Quantum Optics in Fibers, E. Wolf, ed., vol. 39 of Progress in Optics, Elsevier, 1999, pp. 373–469.

[140] S. SLUSSARENKO, M. M. WESTON, H. M. CHRZANOWSKI, L. K. SHALM, V. B. VERMA, S. W. NAM, AND G. J. PRYDE, *Unconditional violation of the shot-noise limit in photonic quantum metrology*, Nature Photonics, 11 (2017), pp. 700–703.

[141] H. STARK, ed., *Applications of optical Fourier transforms*, Academic Press, San Diego, CA, June 1982.

[142] D. STRICKLAND, *Generating high-intensity ultrashort optical pulses*. https://www.nobelprize.org/prizes/physics/2018/strickland/lecture/.

[143] T. SUGIYAMA, P. S. TURNER, AND M. MURAO, *Precision-guaranteed quantum tomography*, Phys. Rev. Lett., 111 (2013), p. 160406.

[144] S. TANZILLI, H. D. RIEDMATTEN, W. TITTEL, H. ZBINDEN, P. BALDI, M. D. MICHELI, D. OSTROWSKY, AND N. GISIN, *Highly efficient photon-pair source using periodically poled lithium niobate waveguide*, Electronics Letters, 37 (2001), p. 26.

[145] P. R. TAPSTER, S. F. SEWARD, AND J. G. RARITY, *Sub-shot-noise measurement of modulated absorption using parametric down-conversion*, Phys. Rev. A, 44 (1991), pp. 3266–3269.

[146] J. R. TAYLOR, *Introduction to Error Analysis, second edition*, University Science Books, Sausalito, CA, 2 ed., July 1997.

[147] M. A. Taylor, J. Janousek, V. Daria, J. Knittel, B. Hage, H.-A. Bachor, and W. P. Bowen, *Biological measurement beyond the quantum limit*, Nature Photonics, 7 (2013), pp. 229–233.

[148] The LIGO Scientific Collaboration, *A gravitational wave observatory operating beyond the quantum shot-noise limit*, Nature Physics, 7 (2011), pp. 962–965.

[149] J. N. Tinsley, M. I. Molodtsov, R. Prevedel, D. Wartmann, J. Espigulé-Pons, M. Lauwers, and A. Vaziri, *Direct detection of a single photon by humans*, Nature Communications, 7 (2016).

[150] K. L. Tosheva, Y. Yuan, P. M. Pereira, S. Culley, and R. Henriques, *Between life and death: strategies to reduce phototoxicity in super-resolution microscopy*, Journal of Physics D: Applied Physics, 53 (2020), p. 163001.

[151] H. Vahlbruch, M. Mehmet, K. Danzmann, and R. Schnabel, *Detection of 15 db squeezed states of light and their application for the absolute calibration of photoelectric quantum efficiency*, Phys. Rev. Lett., 117 (2016), p. 110801.

[152] H. Vahlbruch, D. Wilken, M. Mehmet, and B. Willke, *Laser power stabilization beyond the shot noise limit using squeezed light*, Phys. Rev. Lett., 121 (2018), p. 173601.

[153] A. Vega, E. A. Santos, J. Fuenzalida, M. Gilaberte Basset, T. Pertsch, M. Gräfe, S. Saravi, and F. Setzpfandt, *Fundamental resolution limit of quantum imaging with undetected photons*, Phys. Rev. Res., 4 (2022), p. 033252.

[154] L. E. Vicent, A. B. U'Ren, R. Rangarajan, C. I. Osorio, J. P. Torres, L. Zhang, and I. A. Walmsley, *Design of bright, fiber-coupled and fully factorable photon pair sources*, New Journal of Physics, 12 (2010), p. 093027.

[155] U. von Toussaint, *Bayesian inference in physics*, Rev. Mod. Phys., 83 (2011), pp. 943–999.

[156] D. O. Wackerly, W. Mendenhall, and R. L. Scheaffer, *Mathematical statistics with applications, international edition*, Brooks/Cole, Florence, KY, 7 ed., Oct. 2007.

[157] S. P. Walborn, A. N. de Oliveira, S. Pádua, and C. H. Monken, *Multimode Hong-Ou-Mandel interference*, Physical Review Letters, 90 (2003).

[158] R. M. Waxler and G. W. Cleek, *The effect of temperature and pressure on the refractive index of some oxide glasses.*, J. Res. Natl. Bur. Stand. A. Phys. Chem., 77A (1973), pp. 755–763.

[159] A. G. White, P. K. Lam, D. E. McClelland, H.-A. Bachor, and W. J. Munro, *Kerr noise reduction and squeezing*, Journal of Optics B: Quantum and Semiclassical Optics, 2 (2000), pp. 553–561.

[160] E. E. WOLLMAN, V. B. VERMA, A. D. BEYER, R. M. BRIGGS, B. KORZH, J. P. ALLMARAS, F. MARSILI, A. E. LITA, R. P. MIRIN, S. W. NAM, AND M. D. SHAW, *UV superconducting nanowire single-photon detectors with high efficiency, low noise, and 4 k operating temperature*, Optics Express, 25 (2017), p. 26792.

[161] R. M. WOODWARD, B. E. COLE, V. P. WALLACE, R. J. PYE, D. D. ARNONE, E. H. LINFIELD, AND M. PEPPER, *Terahertz pulse imaging in reflection geometry of human skin cancer and skin tissue*, Physics in Medicine & Biology, 47 (2002), p. 3853.

[162] L.-A. WU, H. J. KIMBLE, J. L. HALL, AND H. WU, *Generation of squeezed states by parametric down conversion*, Phys. Rev. Lett., 57 (1986), pp. 2520–2523.

[163] M. YAMADA, N. NADA, M. SAITOH, AND K. WATANABE, *First-order quasi-phase matched* $LiNbO_3$ *waveguide periodically poled by applying an external field for efficient blue second-harmonic generation*, Applied Physics Letters, 62 (1993), pp. 435–436.

[164] B. YAN, Z. WANG, A. L. PARKER, Y. KUN LAI, P. J. THOMAS, L. YUE, AND J. N. MONKS, *Superlensing microscope objective lens*, Applied Optics, 56 (2017), p. 3142.

[165] Z. YAN, L.-G. ZHU, K. MENG, W. HUANG, AND Q. SHI, *THz medical imaging: from in vitro to in vivo*, Trends in Biotechnology, 40 (2022), pp. 816–830.

[166] F. ZAKI, Y. WANG, H. SU, X. YUAN, AND X. LIU, *Noise adaptive wavelet thresholding for speckle noise removal in optical coherence tomography*, Biomed. Opt. Express, 8 (2017), pp. 2720–2731.

[167] J. ZHANG AND K. PENG, *Quantum teleportation and dense coding by means of bright amplitude-squeezed light and direct measurement of a bell state*, Phys. Rev. A, 62 (2000), p. 064302.

[168] L.-J. ZHANG AND M. XIAO, *Towards quantum-enhanced precision measurements: Promise and challenges*, Chinese Physics B, 22 (2013), p. 110310.

[169] Y. ZHAO, Y. OKAWACHI, J. K. JANG, X. JI, M. LIPSON, AND A. L. GAETA, *Near-degenerate quadrature-squeezed vacuum generation on a silicon-nitride chip*, Phys. Rev. Lett., 124 (2020), p. 193601.

[170] H.-S. ZHONG ET AL., *Quantum computational advantage using photons*, Science, 370 (2020), pp. 1460–1463.

[171] J. ZHU, L. WANG, J. WU, Y. LIANG, F. XIAO, B. XU, Z. ZHANG, X. FAN, Y. ZHOU, J. XIA, AND Z. WANG, *Achieving 1.2* $fm/hz^{1/2}$ *displacement sensitivity with laser interferometry in two-dimensional nanomechanical resonators: Pathways towards quantum-noise-limited measurement at room temperature*, Chinese Physics Letters, 40 (2023), p. 038102.

[172] A. W. Ziarkash, S. K. Joshi, M. Stipčević, and R. Ursin, *Comparative study of afterpulsing behavior and models in single photon counting avalanche photo diode detectors*, Scientific Reports, 8 (2018).